2017

A FIRST EXPERIMENTAL LIMIT ON THE RELATIVE RATES OF MUON CAPTURE ON DEUTERIUM FROM THE QUARTET AND DOUBLET HYPERFINE SPIN STATES OF THE *μd* ATOM

Ray Kreswell Neely
University of Kentucky, kres.neely@gmail.com
Digital Object Identifier: https://doi.org/10.13023/ETD.2017.045

STUDENT AGREEMENT:

I represent that my thesis or dissertation and abstract are my original work. Proper attribution has been given to all outside sources. I understand that I am solely responsible for obtaining any needed copyright permissions. I have obtained needed written permission statement(s) from the owner(s) of each third-party copyrighted matter to be included in my work, allowing electronic distribution (if such use is not permitted by the fair use doctrine) which will be submitted to UKnowledge as Additional File.

I hereby grant to The University of Kentucky and its agents the irrevocable, non-exclusive, and royalty-free license to archive and make accessible my work in whole or in part in all forms of media, now or hereafter known. I agree that the document mentioned above may be made available immediately for worldwide access unless an embargo applies.

I retain all other ownership rights to the copyright of my work. I also retain the right to use in future works (such as articles or books) all or part of my work. I understand that I am free to register the copyright to my work.

REVIEW, APPROVAL AND ACCEPTANCE

The document mentioned above has been reviewed and accepted by the student's advisor, on behalf of the advisory committee, and by the Director of Graduate Studies (DGS), on behalf of the program; we verify that this is the final, approved version of the student's thesis including all changes required by the advisory committee. The undersigned agree to abide by the statements above.

Ray Kreswell Neely, Student

Dr. Tim Gorringe, Major Professor

Dr. Christopher Crawford, Director of Graduate Studies

A FIRST EXPERIMENTAL LIMIT ON THE RELATIVE RATES OF MUON CAPTURE ON DEUTERIUM FROM THE QUARTET AND DOUBLET HYPERFINE SPIN STATES OF THE μd ATOM

DISSERTATION

A dissertation submitted in partial
fulfillment of the requirements for
the degree of Doctor of Philosophy
in the College of Arts and Sciences
at the University of Kentucky

By
R. Kreswell Neely
Lexington, Kentucky

Director: Dr. Dr. Tim Gorringe, Professor of Physics
Lexington, Kentucky 2017

ABSTRACT OF DISSERTATION

A FIRST EXPERIMENTAL LIMIT ON THE RELATIVE RATES OF MUON CAPTURE ON DEUTERIUM FROM THE QUARTET AND DOUBLET HYPERFINE SPIN STATES OF THE μd ATOM

The MuSun experiment will determine the muon capture rate on deuterium ($\mu^- + d \rightarrow n + n + \nu_\mu$) from the doublet hyperfine spin state, Λ_d, of muonic deuterium to a precision of 1.5%. Muon capture can occur from either the quartet or doublet state of the 1S orbital of the μd atom; however, the V-A nature of the process strongly suppresses the rate of capture from the quartet state, Λ_q. Muons in ultra-pure deuterium gas may also catalyze $d + d \rightarrow {}^3He + n$ fusion through the formation of $d\mu d$ molecules.

Using neutron data from run 6 of the MuSun experiment, a new method is developed for determining the relative capture rates from the two hyperfine spin states, Λ_q/Λ_d. This method takes advantage of several improvements which were new for run 6 including a reduced beam-dependent neutron background, thanks to the move from the $\pi E3$ to the $\pi E1$ beamline at Paul Scherrer Institute, and improved energy resolution of the TPC due to the installation of new cryogenic pre-amplifiers. These improvements also allow for a new determination of the relative rates of molecular $dd\mu$ formation from the quartet and doublet atomic states, λ_q/λ_d, as well as the quartet to doublet hyperfine transition rate, λ_{qd}, which were previously determined by Raha [1] using neutron data from MuSun run 4.

An upper bound is placed on the relative capture rate of $\Lambda_q/\Lambda_d < 0.275(90\%cl.)$. The relative molecular formation rate is found to be $\lambda_q/\lambda_d = 103.2 \pm 1.9(stat.) \pm 2.50(syst.)$, and the hyperfine transition rate is found to be $34.74 \pm 0.21(stat.) \pm 0.044(syst.)$.

KEYWORDS: muon, muon capture, deuterium, hyperfine transition, weak interaction

R. Kreswell Neely

February 27, 2017

A FIRST EXPERIMENTAL LIMIT ON THE RELATIVE RATES OF MUON CAPTURE ON DEUTERIUM FROM THE QUARTET AND DOUBLET HYPERFINE SPIN STATES OF THE μd ATOM

By
R. Kreswell Neely

Director of Dissertation: Dr. Tim Gorringe

Director of Graduate Studies: Dr. Christopher Crawford

Date: February 27, 2017

ACKNOWLEDGMENTS

This dissertation would not have been possible without the support and encouragement of many people. First and foremost, I would like to thank my doctoral advisor, Tim Gorringe, for his boundless patience, encouragement, and assistance. And I would like to extend my thanks to the members of my doctoral committee: Christopher Crawford, Renee Fatemi, and Stephen Yates.

I am very grateful to my friends and colleagues on the MuSun experiment, especially my fellow University of Kentucky graduate student, Nandita Raha, whose doctoral research laid much of the groundwork for my own work, and who was immeasurably helpful in learning my way around the MuSun experiment. I am also grateful to my fellow MuSun graduate students Michael Murray, Xiao Luo, Luis Ibañez, and Rachel Ryan who provided a great deal of additional help and support. And I would like to acknowledge all of the members of the MuSun collaboration: V.A. Andreev, E.J. Barnes, R.M. Carey, V.A. Ganzha, A. Gardestig, W. Gohn, T. Gorringe, F.E. Gray, D.W. Hertzog, M. Hildebrandt, L. Ibañez, P. Kammel, B. Kiburg, S.A. Kizilgul, S. Knaack, P.A. Kravtsov, A.G. Krivshich, K. Kubodera, B. Lauss, M. Levchenko, X. Luo, K.R. Lynch, E.M. Maev, O.E. Maev, F. Mulhauser, M.H. Murray, F. Myhrer, A. Nadtochy, C. Petitjean, G.E. Petrov, J. Phillips, R. Prieels, D. Prindle, N. Raha, R. Ryan, D. Salvat, G.N. Schapkin, N. Schroeder, G.G. Semenchuk, M.A. Soroka, V. Tishchenko, A.A. Vasilyev, A.A. Vorobyov, N. Voropaev, M.E. Vznuzdaev, F. Wauters, and P. Winter.

Lastly, but most importantly, I would like to thank those loved ones who supported and encouraged me throughout my many years of school: my parents Bill and Wanda Neely, my sister Susan Neely-Barnes, and most of all my wife Audrey Bowlds.

Dedicated to my parents Bill and Wanda, and to my wife Audrey.

TABLE OF CONTENTS

LIST OF FIGURES

LIST OF TABLES

Chapter 1 Introduction

The MuSun experiment will measure the capture rate of muons on deuterium from the doublet hyperfine state of the muonic deuterium atom, Λ_d, to a precision of 1.5%. In this dissertation, we present an analysis of neutrons from muon–deuterium interactions based on data collected during MuSun run 6 in 2013. This analysis will provide constraints on several parameters of μ–d interactions. Specifically, it will constrain the relative rates of muon capture on deuterium from the quartet and doublet hyperfine spin states of the μd atom.

1.1 Muon Capture

The muon is the second generation charged lepton. It is an elementary particle with negative charge (positive for antimuons) and spin 1/2 which interacts via the weak, electromagnetic, and gravitational forces but not the strong force. In these ways it is similar to the electron. However, at 105.7 MeV/c^2, the muon is over 200 times more massive than the electron. Muons decay to electrons via the emission of a W^- boson (fig. 1.1)

$$\begin{aligned} \mu^- &\rightarrow e^- + \nu_\mu + \bar{\nu}_e \\ \mu^+ &\rightarrow e^+ + \bar{\nu}_\mu + \nu_e \end{aligned} \tag{1.1}$$

with a lifetime of 2.197 μs [9, 10].

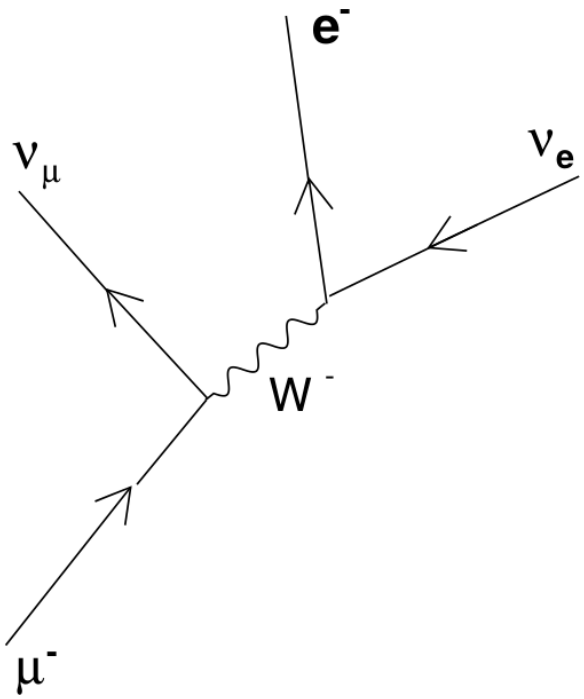

Figure 1.1: Tree level Feynman diagram of the free decay of the muon.

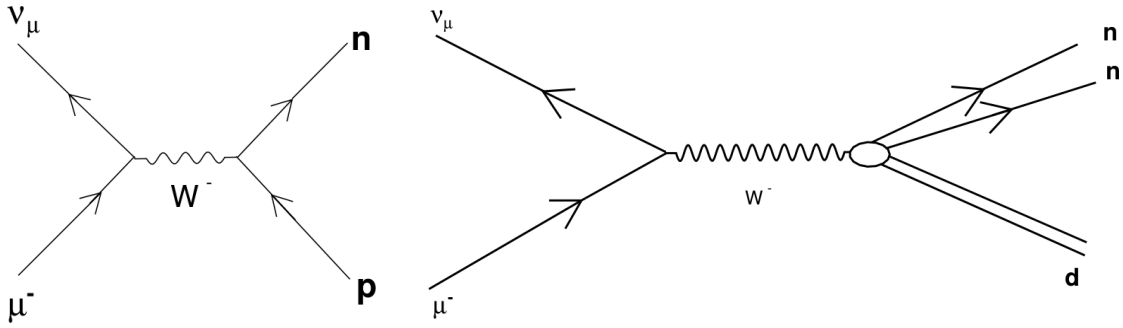

(a) (b)

Figure 1.2: Tree level Feynman diagrams for (a) muon capture on the proton and (b) muon capture on deuterium.

Muons in matter can also undergo capture on atomic nuclei via W-boson exchange. The simplest such process is muon capture on the proton (fig. 1.2a)

$$\mu^- + p \rightarrow n + \nu_\mu \tag{1.2}$$

which was studied by the MuCap experiment [11]. MuSun will measure the rate of muon capture on deuterium. Deuterium is an isotope of hydrogen whose nucleus is composed of one proton and one neutron. As such, muon capture on the deuteron (fig. 1.2b)

$$\mu^- + d \rightarrow n + n + \nu_\mu. \tag{1.3}$$

is the simplest capture process involving multiple nucleons (fig. 1.2b). This process can be calculated to a high degree of precision; however, the capture rate for this process has yet to be measured experimentally to high precision.

Muons in deuterium form muonic deuterium ($\mu^- d$) atoms, with a muon substituted for the electron. Due to the muon's high mass, the orbitals of muonic deuterium are about 200 times smaller radius than the orbitals of ordinary deuterium. As the muon is a spin-1/2 particle, and the deuteron is spin-1, the 1s orbital has both a quartet and doublet hyperfine spin state. These states may be expressed by the equation [12]

$$|s\ m\rangle = \sum_{m_d+m_\mu=m} C^{s_d s_\mu s}_{m_d m_\mu m} |s_d\ m_d\rangle |s_\mu\ m_\mu\rangle \tag{1.4}$$

where s and m are the spin and magnetic quantum numbers associated with the combined state, s_d, s_μ, m_d, and m_μ are the spin and magnetic quantum numbers of the deuteron and muon respectively, and C are the Clebsch-Gordan coefficients. The states with total spin 3/2 (*ie.* the quartet state) are therefore

$$\begin{aligned}
|3/2\ 3/2\rangle &= |1\ 1\rangle |1/2\ 1/2\rangle \\
|3/2\ 1/2\rangle &= \sqrt{\frac{1}{3}} |1\ 1\rangle |1/2\ \text{-}1/2\rangle + \sqrt{\frac{2}{3}} |1\ 0\rangle |1/2\ 1/2\rangle \\
|3/2\ \text{-}1/2\rangle &= \sqrt{\frac{2}{3}} |1\ 0\rangle |1/2\ \text{-}1/2\rangle + \sqrt{\frac{1}{3}} |1\ \text{-}1\rangle |1/2\ 1/2\rangle \\
|3/2\ \text{-}3/2\rangle &= |1\ \text{-}1\rangle |1/2\ \text{-}1/2\rangle ,
\end{aligned} \tag{1.5}$$

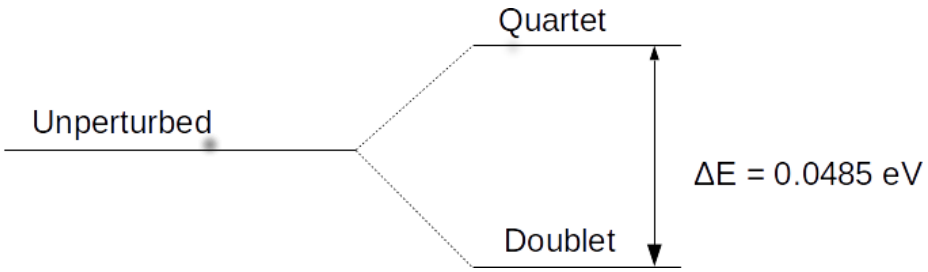

Figure 1.3: Hyperfine splitting of the quartet and doublet spin states of the 1s orbital of the μd atom.

and the states with total spin 1/2 (*ie.* the doublet state) are therefore

$$\begin{aligned} |1/2\ 1/2\rangle &= \sqrt{\frac{2}{3}}\,|1\ 1\rangle\,|1/2\ \text{-}1/2\rangle - \sqrt{\frac{1}{3}}\,|1\ 0\rangle\,|1/2\ 1/2\rangle \\ |1/2\ \text{-}1/2\rangle &= \sqrt{\frac{1}{3}}\,|1\ 0\rangle\,|1/2\ \text{-}1/2\rangle - \sqrt{\frac{2}{3}}\,|1\ \text{-}1\rangle\,|1/2\ 1/2\rangle\,. \end{aligned} \tag{1.6}$$

Spin-spin coupling between the muon and the deuteron results in a breaking of the energy degeneracy of the quartet and doublet states, as depicted in figure 1.3, resulting in an energy difference of $\Delta E = 0.0485$ eV.

Muon capture can occur from either hyperfine state of the μd atom; however, capture from the quartet state, Λ_q, is strongly suppressed [13, 14]. For this reason, MuSun will determine the capture rate from the doublet state, Λ_d. A μd atom may also form a diatomic $dd\mu$ molecule with another deuterium atom from either hyperfine state. These molecules rapidly undergo muon catalyzed fusion resulting in either a helium-3 nucleus plus a neutron, or a tritium nucleus plus a proton

$$\mu^- + d + d = \mu^- + {}^3He + n \tag{1.7a}$$
$$\mu^- + d + d = \mu^- + t + p. \tag{1.7b}$$

The full dynamics of muonic deuterium are discussed in detail in chapter 2.

1.2 Theoretical background

At low energy, quantum chromodynamics (QCD) is non-perturbative. Thus, effective field theories (EFTs) are used to model low energy nuclear interactions. These EFTs have reduced degrees of freedom, as compared to the full QCD treatment, which allows for the recovery of a pertubative approach to calculating many interactions. Two commonly used EFTs are chiral perturbation theory (χPT or χEFT), in which chiral symmetry is a conserved quantity, and pionless effective field theory ($\not\pi$EFT), which approximates meson exchange currents as nucleon-nucleon contact interactions. For calculations of nucleon-nucleon interactions, such as muon capture on deuterium, both χPT and $\not\pi EFT$ require low energy constants (LECs) which must be determined experimentally. The dominant uncertainty in these interactions is in a particular LEC

	Λ_d (s^{-1})	Method	Source	Year
Experiment	409 ± 40	neutron detection	Cargnelli [20]	1989
	470 ± 29	lifetime, liquid d_2	Bardin [21]	1986
Theory	383.8–392.4	χEFT	Adam [22]	2012
	399 ± 3	χEFT	Marcucci [23]	2012
	392.0 ± 2.3	hybrid EFT	Marcucci [24]	2011
	416 ± 6	SNPA and hybrid EFT	Ricci [25]	2010

Table 1.1: Previous measurements and calculations of Λ_d.

which in χPT is denoted $\hat{d}^R$ and in $\not\pi$EFT is denoted $L_{1,A}$ [15, 16, 17]. This constant is currently constrained by tritium beta decay [18]; however, a precise measurement of Λ_d could significantly improve the constraints on this term [16].

The parameters $\hat{d}^R$ and $L_{1,A}$ play a critical role in EFT calculations of other two nucleon interactions besides μd capture. Most notably, they are essential for calculations of the initial step of the p-p cycle

$$p + p \rightarrow d + e^- + \nu_e, \tag{1.8}$$

which is the primary channel for solar fusion (see figure 1.4). The correspondence between this process and μd capture is the motivation behind the name of MuSun. These LECs are also used to calculate neutrino-deuterium reactions, such as the processes observed by the Sudbury Neutrino Observatory (SNO). SNO used a large volume of heavy water to observe two processes,

$$\nu_e + d \rightarrow p + p + e^- \tag{1.9a}$$

$$\nu_x + d \rightarrow p + n + \nu_x. \tag{1.9b}$$

The first of these processes (eq. 1.9a) is a charged-current reaction in which an electron neutrino exchanges a $W^{\pm}$ boson with the deuteron. In the second reaction (eq. 1.9b), a neutrino of any flavor exchanges a Z^0 boson with the deuteron resulting in the fission of the deuterium nucleus. Since reaction 1.9b can occur for any neutrino flavor, but reaction 1.9a requires an electron neutrino, the simultaneous observation of both processes allowed the SNO experiment to confirm neutrino oscillation and resolve the "missing neutrino" problem [19].

1.3 Previous determinations of Λ_d

The μd doublet capture rate, Λ_d has been experimentally measured and theoretically calculated previously. Table 1.1 shows several of these results.

1.3.1 Experimental measurements

The most recent measurement of Λ_d to date was performed by Cargnelli, *et al.* in 1989 [20], using the detection of capture neutrons (neutrons produced by reaction 1.3). They found a value of 409 ± 40 s^{-1} for Λ_d. Bardin, *et al.* also measured the

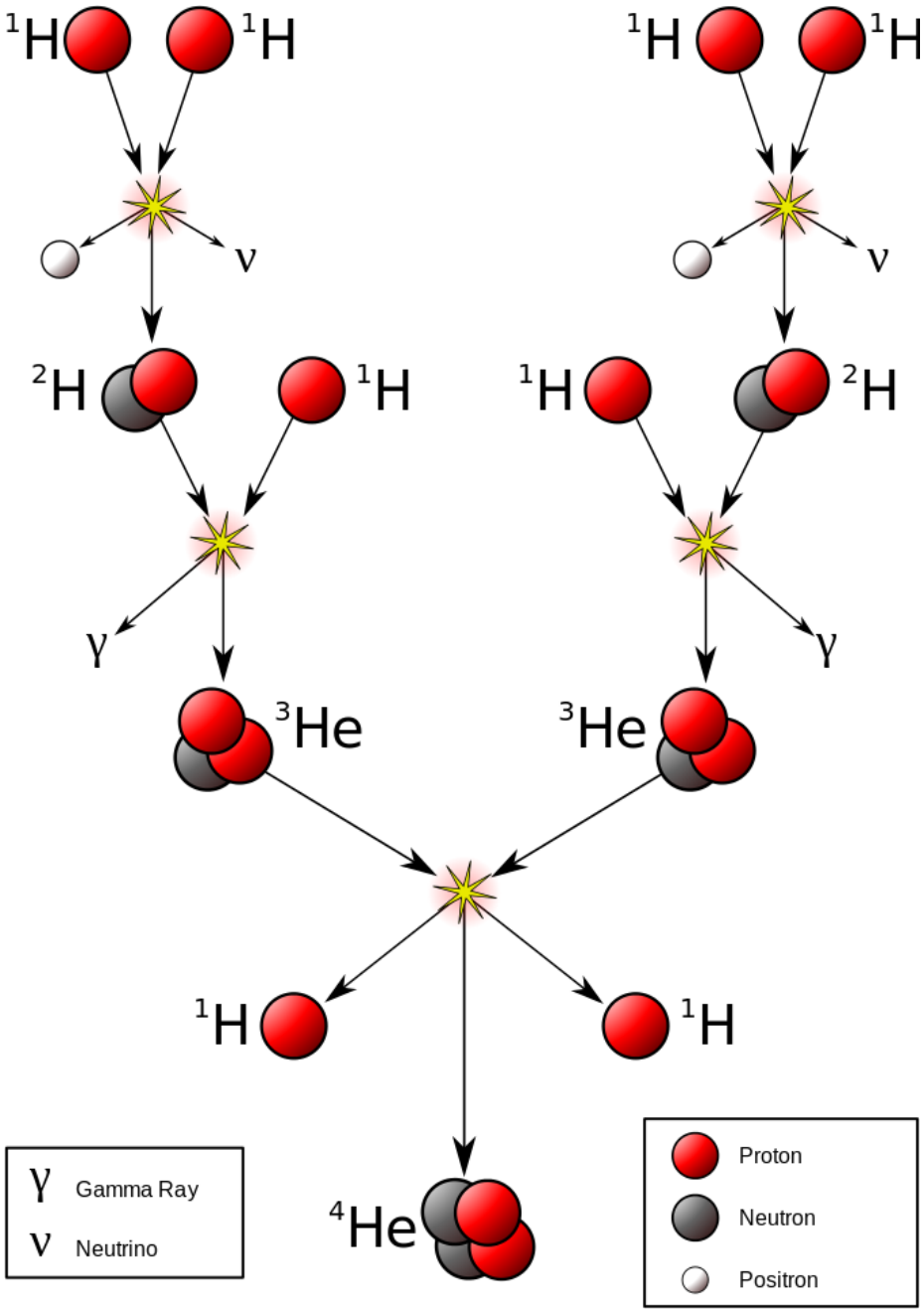

Figure 1.4: The p-p cycle of solar fusion. I) Two protons (^{1}H nuclei) fuse to form a deuteron, emitting a positron and an electron neutrino (charged weak interaction). II) The deuteron fuses with a proton to form a ^{3}He nucleus, emitting a 5.49 MeV gamma ray (strong interaction). III) Two ^{3}He nuclei fuse to form a ^{4}He nucleus emitting two protons (strong interaction). (Image source, Wikimedia Commons [2])

Λ_q (s^{-1})	Λ_d (s^{-1})	Λ_d/Λ_q	Source	Year
11.4	416 ± 6	36.5	Ricci [25]	2010
6.07 ± 0.04	374 ± 18	61.6 ± 3.4	Mintz [28]	1973
12.0	312.7	26.1	Pascual [29]	1972
30	450	15	Cremmer [30]	1967
15	334	22	Wang [31]	1965

Table 1.2: Calculations of Λ_q. There is a wide range in the calculated value of Λ_q and therefore Λ_d/Λ_q as well.

doublet capture rate in 1986 [21]. Their technique, known as the lifetime technique, measured the time of decay electrons relative to the entrance time of a muon into a liquid deuterium target. This is similar to the technique used by MuSun, which will be described in detail in chapter 2. Bardin measured a doublet capture rate of 470 ± 29 s^{-1}. While this measurement is higher precision than the one made by Cargnelli, it is less consistent with modern theory.

Prior to this work, no experimental measurement has been made of either the quartet capture rate, Λ_q, nor the relative rates of capture from the two hyperfine states, Λ_d/Λ_q.

1.3.2 Theoretical calculations

The muon capture rate on deuterium has been calculated several times using a variety of techniques. Calculations were done in the 1990s by Adam [26], Doi [7], and Tatara [27] using the standard nuclear physics approach (SNPA), which treats nuclei as simply a system of interacting nucleons. More recently, Chen [17] performed a calculation using $\not\pi$EFT and Ando [16], Ricci [25] and Marcucci [24] performed calculations using a hybrid of SNPA and χEFT. The most recent calculations were performed by Adam [22] and Marcucci [23] in 2012 using χEFT. As can be seen in table 1.1, these most recent calculations have uncertainties on the order of a few percent or better.

Although Λ_q has not yet been measured experimentally, multiple calculations have been made of its value. Several of these are presented in table 1.2. As can be seen, there is a great deal of variation in the predicted value of Λ_q and thus in Λ_d/Λ_q as well. Doi *et al.* (1991) [3] showed that Λ_d/Λ_q has a strong dependence on the value of the weak pseudoscalar coupling constant, g_p, and on the $\pi N\Delta$ coupling constant, $c_0 m_\pi^3$. Thus, an experimental measurement of Λ_d/Λ_q will help constrain these two parameters. Figure 1.5 shows these relations.

1.4 Overview of MuSun

MuSun will determine Λ_d using the lifetime technique. The technique is to measure the disappearance rate of muons in ultra-pure deuterium gas by observing the timing of outgoing decay electrons relative to the muon entrance into the deuterium target. The primary channel for muon disappearance is beta decay, with a rate of $\lambda_\mu = 455$ ms^{-1}, followed by the doublet capture rate $\Lambda_d \sim 400$ s^{-1}. Thus, the total

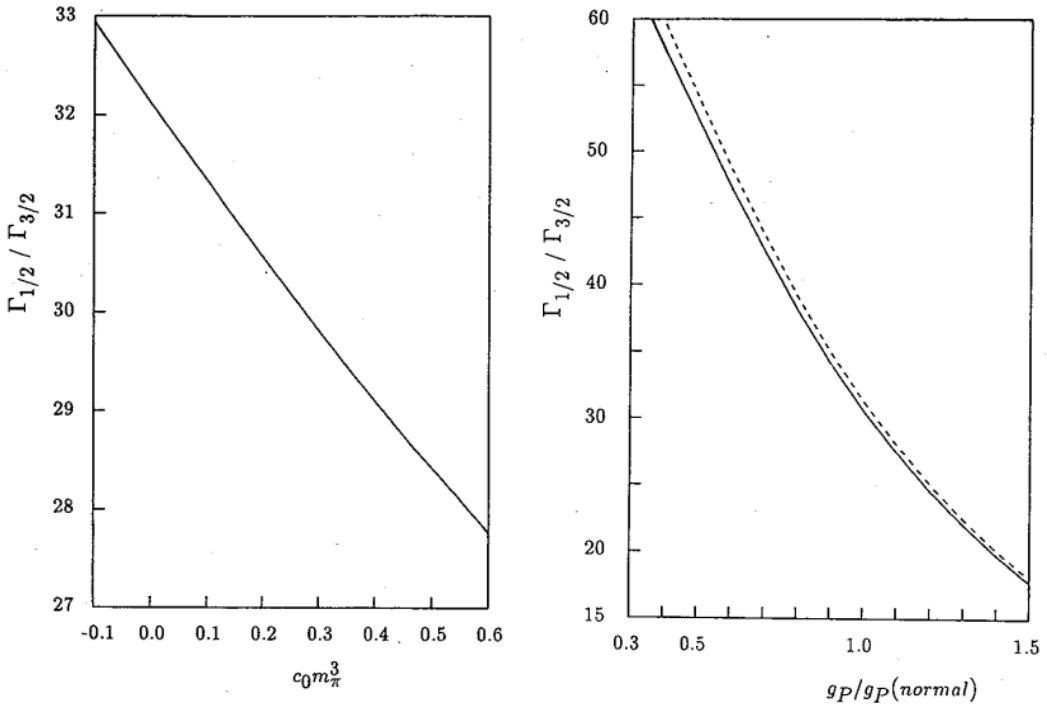

(a) (b)

Figure 1.5: Dependence of Λ_d/Λ_q on (a) the $\pi N\Delta$ coupling constant $c_0 m_\pi^3$ and (b) the value of the weak pseudoscalar coupling g_p (relative to nominal). The solid and dashed lines in figure (b) correspond to $c_0 m_\pi^3$ =0.188 and 0.0969 respectively. These figures are reproduced from Doi *et al.* (1991) [3].

disappearance rate, Λ, is simply

$$\Lambda = \lambda_\mu + \Lambda_d. \tag{1.10}$$

After Λ_d, the next largest contributor to muon disappearance is the quartet capture rate, $\Lambda_q \sim 10$ s^{-1}, which is on the order of the projected uncertainty in the final measurement.

Since Λ_d is on the order of 10^{-3} of λ_μ, and the goal is to determine Λ_d to one part in 10^{-2}, the total disappearance rate must be determined to one part in 10^{-5}. This provides some technical challenges. First, the muon lifetime must be determined to high precision. This was accomplished by the MuLan experiment, a predecessor to MuSun, which found a value of $\tau_{\mu^+} = 2196980.3 \pm 2.2$ ps [10], corresponding to a lifetime of $\lambda_\mu = 455170.22 \pm 0.46$ s^{-1}. By CPT symmetry, it can be assumed that $\tau_{\mu^+} = \tau_{\mu^-}$. Second, the deuterium target must be chemically and isotopically ultrapure. This is accomplished by continuous circulation of the gas through a zeolite filter. Third, the muon entrance must be identified with high efficiency, and lone muon entrances must be ensured to high efficiency. This is accomplished through the combined use of a beam kicker and sophisticated entrance counter. Fourth, it must be assured that the muon stops in the deuterium gas. This is accomplished by the use of a time projection chamber (TPC) in which the deuterium gas is an active target.

MuSun is preceded by the MuCap experiment, which measured the muon capture rate on hydrogen (protium). Their final result of $\Lambda_s = 714.9 \pm 10.5$ s^{-1} for the capture rate from the singlet state of muonic hydrogen was published in 2013 [11]. MuCap also used the lifetime technique for this measurement with a very similar experimental design to the one used for MuSun. Indeed, much of the experimental apparatus for MuSun is carried over from MuCap. This includes the beam kicker, entrance detector, electron detectors, and gas purification system.

The design requirements and the experimental setup for MuSun are discussed in detail over the next two chapters.

1.5 Outline of Analysis Program

The primary result of this dissertation is a first experimental constraint on the ratio of capture rates Λ_q/Λ_d. This ratio is determined by observing the time evolution of neutrons produced both by muon capture and by muon catalyzed fusion. It is therefore critical to positively discriminate neutrons produced by these two different processes. Much of the analysis presented here is focused on developing methods for doing the necessary identification and discrimination of neutrons. This analysis also presents an opportunity to reproduce the results of Raha [1] for the ratio of molecular formation rates λ_q/λ_d and the hyperfine transition rate λ_{qd}.

Chapter 2 Experimental Design

2.1 μd Kinetics

Muons stopped in pure deuterium form μd atoms which quickly settle into the 1S ground state. From here, the μd atom may undergo one of three processes: muon decay (eq. 1.1), μd capture (eq. 1.3), or $dd\mu$ molecule formation which rapidly leads to muon catalyzed fusion. The full kinetics of these three processes are depicted in figure 2.1, and the relevant parameters are listed in table 2.1. The lifetime of positive muons was measured to part-per-million level precision by the MuLan experiment [10]. By the CPT theorem, the μ^- lifetime will be identical. Deuterium capture and muon catalyzed fusion are discussed in detail in this chapter. In practice, muons may stop in atoms of $Z > 1$, either in the form of materials used in the experimental apparatus, or in the form of gas impurities. The capture rate of muons on nuclei is roughly proportional to Z^4 [32], so high-Z capture is a potential source of significant background. The need to minimize muon capture on $Z > 1$ nuclei is one of the key factors behind the experimental design.

2.1.1 Muon capture on deuterium

The muon is a fermion with spin 1/2, while the deuteron, being composed of two nucleons, has spin 1. As such, the 1S orbital of muonic deuterium has both a doublet and a quartet spin state, with a hyperfine splitting energy of $\Delta = 0.0485$ eV [33] (where

Description	Quantity	Value (30K)	Value (300K)
initial quartet fraction	q	2/3	
hyperfine trans. $q \to d$	$\lambda_{qd}\,(\mu s^{-1})$	37.0(4)	35(5)
hyperfine trans. $d \to q$	$\lambda_{dq}\,(\mu s^{-1})$	5.3×10^{-7}	10.7
$dd\mu$ form. rate from q	$\lambda_q\,(\mu s^{-1})$	3.98(5)	~3.75
$dd\mu$ form. rate from d	$\lambda_d\,(\mu s^{-1})$	0.053(3)	2.549(23)
^3He total capture rate	$\Lambda_{He}\,(s^{-1})$	2216(70)	
μd quartet capture rate	$\Lambda_q\,(s^{-1})$	~ 10	
μd doublet capture rate	$\Lambda_d\,(s^{-1})$	~ 400	
eff. fusion fraction	β	0.517(15)	0.590(6)
sticking fraction	$\bar{\omega}$	0.1206(6)	

Table 2.1: The parameters for muons in deuterium relevant to the MuSun experiment. These data are taken from Balin *et al.* (2011) [8]. Values for λ_{dq} are calculated from values for λ_{qd} using equation 2.1. The hyperfine transition rates and $dd\mu$ molecular formation rates (λ_{qd}, λ_{dq}, λ_q, and λ_d) are density dependent. The values given are for liquid deuterium. At experimental conditions, the density is $\phi = 0.05$ relative to liquid D_2. These parameters are therefore scaled by this factor for MuSun conditions. It is useful to define $\omega = \beta\bar{\omega} = 0.0624$.

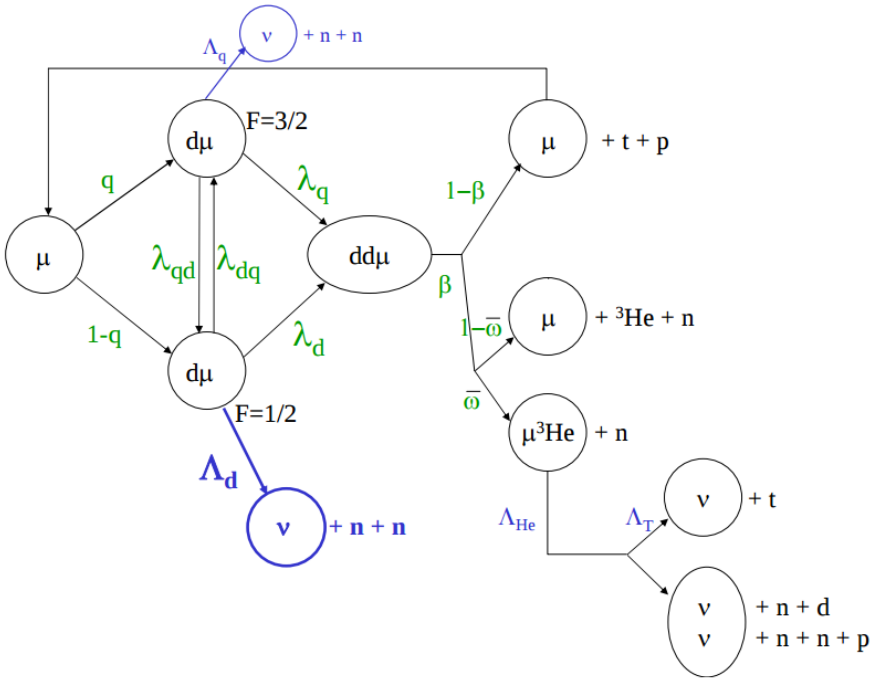

Figure 2.1: Muon kinetics in deuterium. The muon forms a μd atom in a statistical mix of spin states, where $q = 2/3$ is the initial quartet fraction. Transitions may occur between these two spin states via atomic collisions. At experimental conditions λ_{dq} is negligible. From these two spin states, the muon may capture on the deuteron, or a $dd\mu$ molecule may form. These molecules immediately undergo muon catalyzed fusion (μCF) producing either ^3He+n or $t+p$. Since the muon is a spectator particle in μCF, it may either stick to the ^3He (with a probability of 12%) or be recycled to repeat this process. The muon may also decay to an electron at any stage in this process.

the doublet state is the true ground state). Since muon capture is a weak charged current interaction (involving by the exchange of a $W^{\pm}$-boson), the interaction operator has a vector-minus-axial-vector ($V - A$) structure. This operator projects out the quartet component, so muon capture occurs almost exclusively from the doublet state with a predicted rate of $\Lambda_d \sim 400$ s^{-1}. However, muon capture can occur from the quartet state with a much smaller rate, estimated to be $\Lambda_q \sim 10$ s^{-1} (see tables 1.1, 1.2, and references therein). The μd atoms initially form in a statistical mix of these two spin states, 2/3 quartet and 1/3 doublet, but atomic collisions can induce transitions between these two states. If the kinetic energy of thermal collisions is well below the hyperfine splitting energy, $\Delta = 0.0485$ eV, then λ_{dq} depends exponentially on temperature according to the detailed balance relation [8]

$$\lambda_{dq} = 2e^{-\frac{\Delta}{kT}}\lambda_{qd}, \tag{2.1}$$

while λ_{qd} is only weakly dependent on temperature (fig. 2.2). As the goal of MuSun is to determine Λ_d to high precision, it is important to maximize the depopulation of

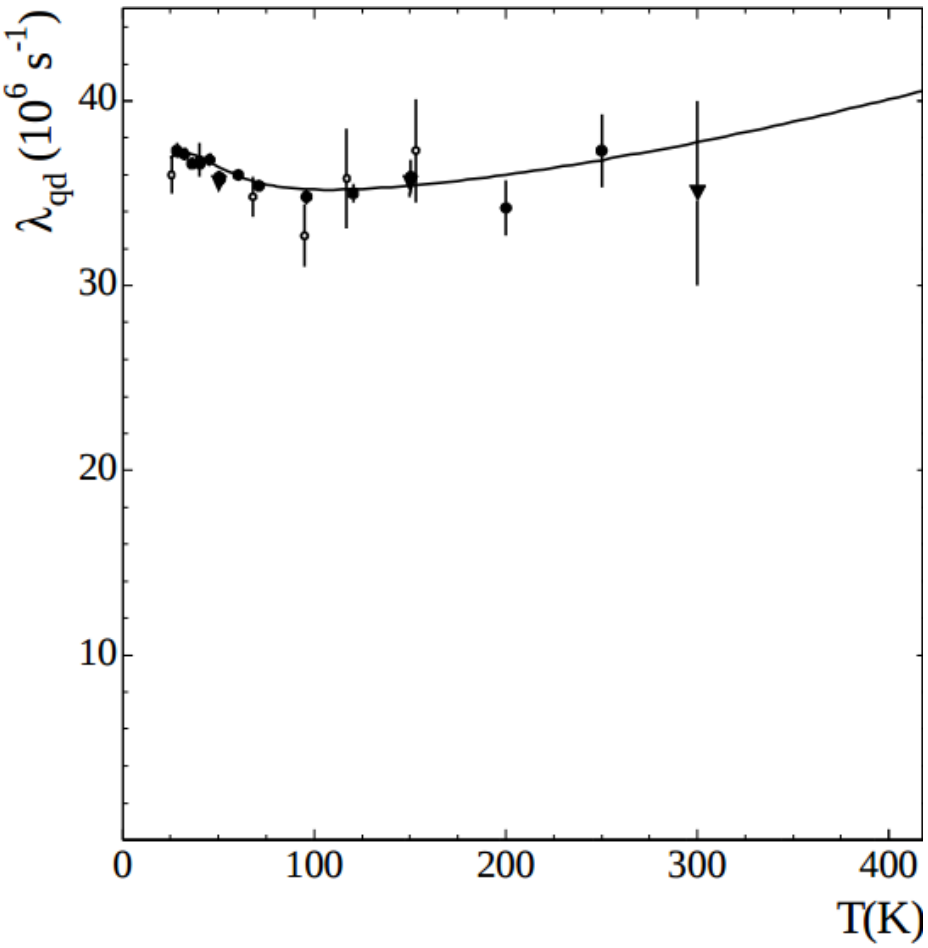

Figure 2.2: Hyperfine transition rate from the quartet to the doublet spin state of the μd atom as a function of temperature. Figure is from reference [4] and data are from references therein.

the quartet state, and, more generally, to ensure that the quartet/doublet fraction is well understood under the experimental conditions. This is another major motivation for the design of the experiment.

2.1.2 Muon catalyzed fusion

A muonic deuterium atom may form a diatomic molecule with an ordinary deuterium atom via collisions with D_2 molecules. Since the muon is about 207 times more massive than the electron, the nuclear separation in such a molecule is about 207 times smaller than in regular diatomic deuterium. This reduces the potential barrier for nuclear fusion enough that muon catalyzed fusion (μCF) occurs essentially immediately. The fusion reaction may result in a helium-3 plus a neutron, or in a triton plus a proton

$$dd\mu \rightarrow {}^3He + n + \mu \tag{2.2a}$$

$$dd\mu \rightarrow t + p + \mu. \tag{2.2b}$$

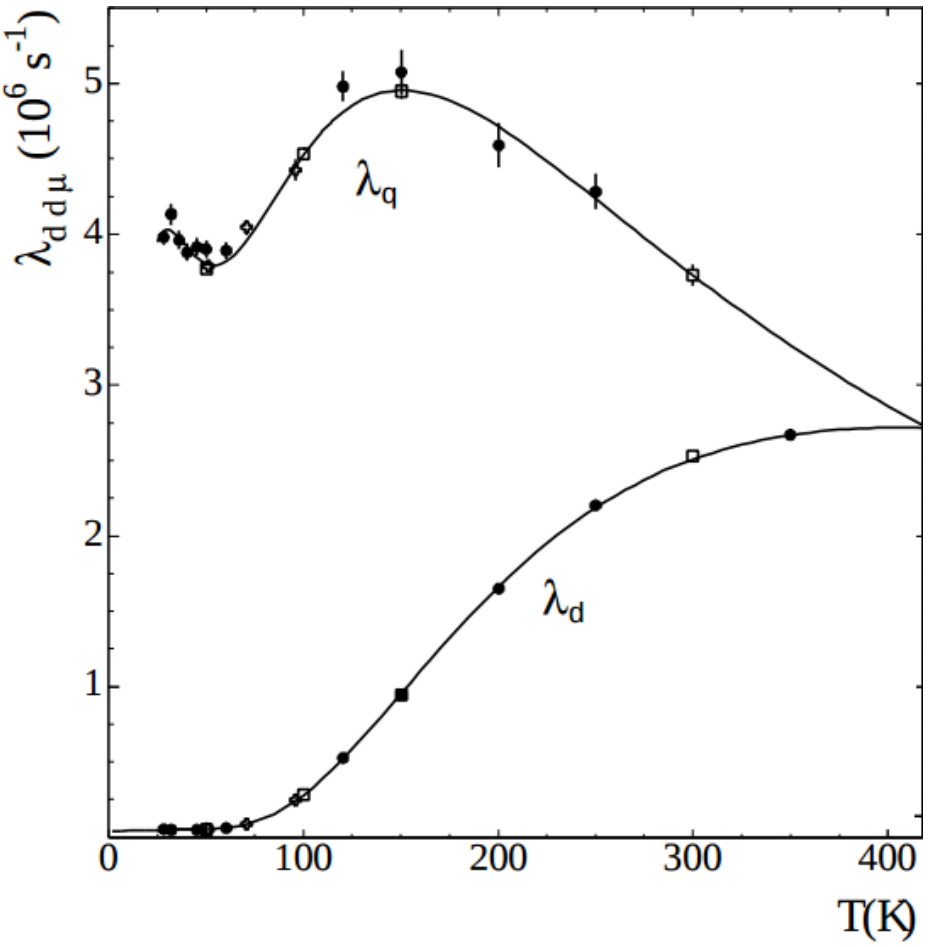

Figure 2.3: The rates of $dd\mu$ molecular formation from the quartet and doublet states of the μd atom as a function of temperature. Figure is from [4] and data are from references therein.

In this process, the muon is a spectator particle. It catalyzes the fusion but does not directly participate. This means that the muon can be recycled into another μd atom. There is also a small probability of the muon "sticking" to one of the fusion products. That is, it becomes bound in an atomic orbital of a ^{3}He, ^{3}H, or ^{1}H nucleus, effectively removing it from participating in any further reactions.

The $dd\mu$ molecular formation rate depends both on temperature and on the spin state of the μd atom. At temperatures above about 400 K, λ_d and λ_q are approximately equal, but λ_d monotonically decreases towards 0 K, while λ_q varies in a more complicated fashion, but is also reduced at low temperatures. These rates are depicted in figure 2.3.

2.2 Target Conditions

MuSun uses a low temperature, high density, gaseous deuterium target, with optimal conditions determined by the kinetics of muonic deuterium. There are several advan-

tages to using a target with these conditions. Chief among them is that it greatly enhances λ_{qd} relative to λ_{dq}, improving the efficiency for determining Λ_d. This effect is further enhanced by the gas being at high density. A low temperature also reduces the $dd\mu$ molecular formation rate by reducing the formation rate from the doublet hyperfine state, thus reducing the background from μCF. Furthermore, the high density increases the stopping fraction of muons in the gas, and a low temperature allows for a high density to be maintained without requiring an exceedingly high pressure.

The time evolution of the populations of the μd quartet, μd doublet and μ^3He states depend on the temperature and density of the deuterium target. The quartet and doublet states are initially populated in a statistical mix, while the helium-3 state is initially unpopulated. After formation, μd atoms may be lost to $dd\mu$ molecular formation, capture, or muon decay. These processes happen for both hyperfine spin states at rates unique to the two states. Transitions between the two states may also occur, resulting in a depopulation of one state and a population of the other. Both states may also be repopulated through muon recycling following a muon catalyzed fusion, again initially forming in a statistical mix. As $dd\mu$ formation very rapidly leads to fusion, we may make the approximation that it occurs instantaneously, so the molecular formation rates from both HF spin states are equal to the effective fusion rates. The μ^3He state is therefore populated by molecular formation, scaled by the effective sticking fraction $\omega = \beta\bar{\omega}$, and is depopulated by helium capture and muon decay. The populations of these three states are therefore described by a system of three coupled, first-order differential equations

$$\begin{aligned}
\frac{dN_d}{dt} &= \left[-\lambda_\mu - \Lambda_d - \phi\lambda_{dq} - \phi\lambda_d\left(1 - \frac{1}{3}(1-\omega)\right)\right] N_d + \left[\phi\lambda_{qd} + \frac{1}{3}\phi\lambda_q(1-\omega)\right] N_q \\
\frac{dN_q}{dt} &= \left[\phi\lambda_{dq} + \frac{2}{3}\phi\lambda_d(1-\omega)\right] N_d + \left[-\lambda_\mu - \Lambda_q - \phi\lambda_{qd} - \phi\lambda_q\left(1 - \frac{2}{3}(1-\omega)\right)\right] N_q \\
\frac{dN_{He}}{dt} &= \left[\phi\lambda_d\omega\right] N_d + \left[\phi\lambda_q\omega\right] N_q + \left[-\lambda_\mu - \Lambda_{He}\right] N_{He}
\end{aligned} \tag{2.3}$$

where λ_μ is the muon decay rate and ϕ is the target density (a dimensionless quantity normalized to liquid density). Since $dd\mu$ formation and HF spin state transitions are both collisional processes, they scale with the target density. The values for these parameters at 300 K and 30 K are listed in table 2.1. The initial conditions are

$$\begin{aligned}
N_q(0) &= 2/3 \\
N_d(0) &= 1/3 \\
N_{He}(0) &= 0.
\end{aligned} \tag{2.4}$$

These equations were solved numerically in reference [4] for a variety of environmental conditions. The solutions for the time evolution of μd states and $\mu^3 He$ are shown in figure 2.4. As can be seen, at T=30 K and ϕ=0.05, the μd quartet hyperfine spin state population rapidly depopulates, and the $\mu^3 He$ population is strongly suppressed. Thus, these conditions were chosen for the deuterium target. During run 6 production data taking, the actual conditions were T=31 K and P=5.1 bar, which corresponds to a density of ϕ=0.065 relative to liquid D_2 [45].

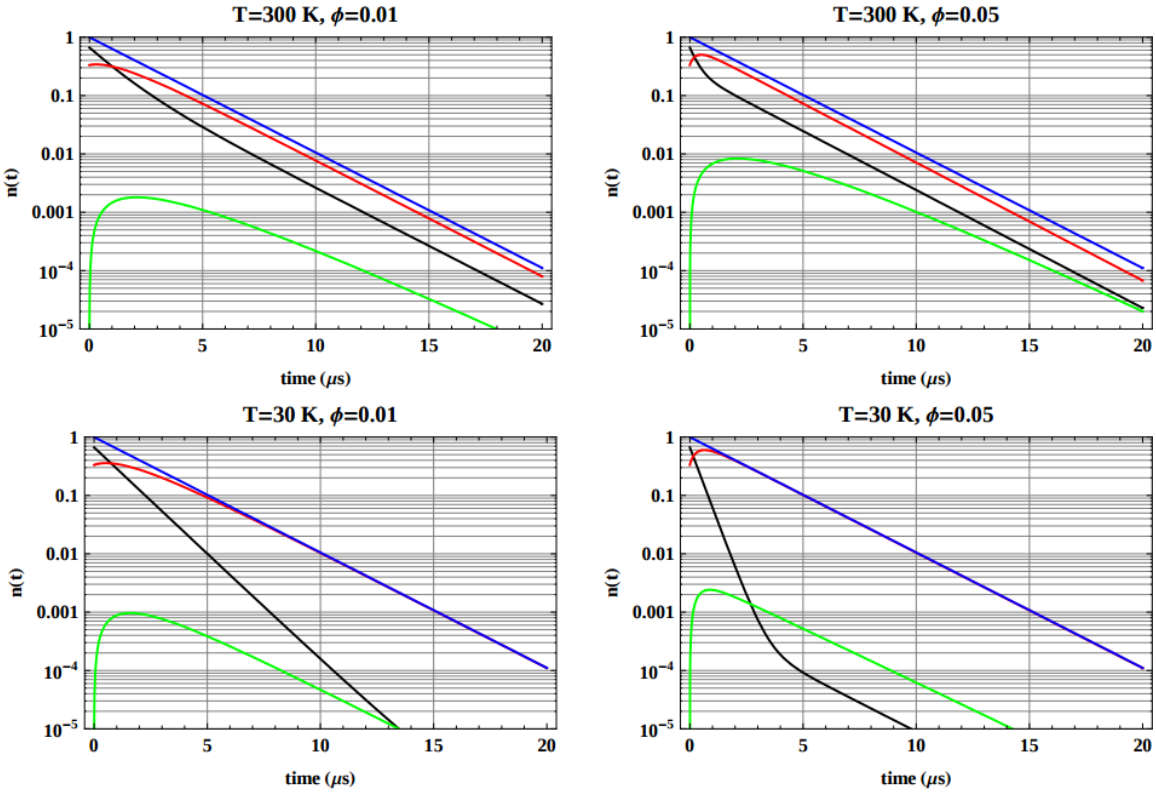

Figure 2.4: Numerical solutions for the populations of doublet μd atoms (red), quartet μd atoms (black), and μHe atoms (green) as a function of time for four different sets of target conditions. The blue curve shows the total μd populations for both hyperfine states (i.e., the sum of the black and red curves). These are solutions to equations 2.3 as determined in reference [4], and the figure is reproduced from that source. The rapid depopulation of the quartet state and the suppression of μCF at T=30 K and ϕ=0.05 (bottom right) are the main motivating factors for choosing these experimental conditions.

2.2.1 Chemical and isotopic purity

In general, the capture rate of negative muons on atomic nuclei increases with Z [34]. Furthermore, muons stopped in deuterium will preferentially transfer to higher Z atoms. For this reason, it is very important to the success of MuSun to minimize the amount of muon capture on high Z nuclei in the experiment. To this extent, three precautions are taken. First, A time projection chamber (TPC) is used to identify muon stops in the deuterium gas. A detailed description of the design and operation of the TPC is given in section 3.3. Second, as much as possible, very high Z materials are used in the construction of the TPC and other components surrounding the gas target. This ensures that muon capture on these materials happens very rapidly and thus has a minimal impact on the determination of Λ_d. Third, the deuterium gas target must be ultra-pure.

The main potential contaminants of the D_2 gas target are atmospheric compounds, N_2, O_2, and H_2O. As 30 K is well below the boiling point of these compounds,

they are largely frozen out of the gas. However, the partial pressure of nitrogen is still high enough to potentially disrupt the measurement of Λ_d. It was determined [35] that for the experimental conditions of 31 K, the concentration of nitrogen is $\sim$20 ppb. The muon capture rate on nitrogen is $6.6(4) \times 10^4$ s^{-1} [34, 14], much faster than the predicted value of Λ_d. Also, muons will preferentially transfer from deuterium to nitrogen nuclei. The transfer rate is very rapid at room temperature, $1.45(2) \times 10^{11}$ s^{-1} [36], but is strongly suppressed at 30 K to an estimated $\sim$320 s^{-1} [35]. For these reasons, nitrogen must be cleaned to the level of a few ppb to achieve the desired 1.5% precision in the measurement of Λ_d. This level of chemical purity is achieved by continuous circulation of the target gas through a synthetic zeolite filter (see section 3.3.6).

The muon capture rate on the proton was recently measured by the MuCap experiment to be 714.9 ± 10.5 s^{-1} [11]. Thus, the deuterium target must be isotopically pure to the ppm level.

2.3 Observable Neutron Rates

The time evolution of the observed neutrons from both capture and fusion can be calculated using equations 2.3. With a few simplifying approximations, these equations may be solved analytically. As Λ_q and Λ_d are each at least two orders of magnitude smaller than the other rates appearing in these equations, we may take their contributions to the muon state populations described by equations 2.3 to be negligible. They will be reintroduced when determining the observable rate of capture neutrons (described below). We also only consider the case for T=30 K, and so can take $\lambda_{dq} \approx 0$.

2.3.1 Neutron Rates Without Muon Recycling

We begin by disregarding the small contribution from muon recycling. in this case, the kinetics from equation 2.3 can be reduced to a system of two equations

$$\frac{d}{dt}\begin{pmatrix} N_d \\ N_q \end{pmatrix} = \begin{pmatrix} -\lambda_1 & \phi\lambda_{qd} \\ 0 & -\lambda_2 \end{pmatrix}\begin{pmatrix} N_d \\ N_q \end{pmatrix} \tag{2.5}$$

where $\lambda_1 = \lambda_\mu + \phi\lambda_d$ and $\lambda_2 = \lambda_\mu + \phi\lambda_{qd} + \phi\lambda_q$. The initial conditions are as before

$$N_d(0) = 1/3\ N_0$$
$$N_q(0) = 2/3\ N_0.$$

Since equation 2.5 is upper triangular, the eigenvalues are simply the diagonal elements, $-\lambda_1$ and $-\lambda_2$, with eigenvectors

$$v_1 = \begin{pmatrix} 1 \\ 0 \end{pmatrix}$$
$$v_2 = \begin{pmatrix} \frac{-\lambda_{qd}}{\lambda_{qd}+\lambda_q-\lambda_d} \\ 1 \end{pmatrix}.$$

For convenience, we will define $X = \frac{\lambda_{qd}}{\lambda_{qd}+\lambda_q-\lambda_d}$.The solutions to equation 2.5 are therefore

$$\begin{aligned} N_d(t) &= N_0 \left[\left(\frac{1}{3} + \frac{2}{3}X \right) e^{-\lambda_1 t} - \frac{2}{3} X e^{-\lambda_2 t} \right] \\ N_q(t) &= \frac{2}{3} N_0 e^{-\lambda_2 t}. \end{aligned} \tag{2.6}$$

2.3.2 Effect of Muon Recycling

To consider the case where the muon recycling contribution is nonzero, we will make the same simplifying assumptions as before. As we are concerned with determining the time distributions of fusion and capture neutrons, and muons which stick to helium are removed from further interactions, the kinetic equation for the helium population may be discarded. The kinetic equations then become

$$\begin{aligned} &\frac{d}{dt} \begin{pmatrix} N_d \\ N_q \end{pmatrix} = \\ &\begin{pmatrix} -\lambda_\mu - \phi\lambda_d \left(1 - \frac{1}{3}(1-\omega)\right) & \phi\lambda_{qd} + \frac{1}{3}\phi\lambda_q(1-\omega) \\ \frac{2}{3}\phi\lambda_d(1-\omega) & -\lambda_\mu - \phi\lambda_{qd} - \phi\lambda_q \left(1 - \frac{2}{3}(1-\omega)\right) \end{pmatrix} \begin{pmatrix} N_d \\ N_q \end{pmatrix} \end{aligned} \tag{2.7}$$

We may make one further simplifying approximation by noting that $\frac{2}{3}\phi\lambda_d(1-\omega)$ is at least two orders of magnitude smaller than the other matrix elements (see table 2.1). Discarding this term makes the matrix in equation 2.7 upper triangular, as in equation 2.5. Therefore, the solution will be identical to equation 2.6, but with

$$\begin{aligned} \lambda_1 &= \lambda_\mu + \phi\lambda_d \left(1 - \frac{1}{3}(1-\omega)\right) \\ \lambda_2 &= \lambda_\mu + \phi\lambda_{qd} + \phi\lambda_q \left(1 - \frac{2}{3}(1-\omega)\right) \end{aligned} \tag{2.8}$$

and

$$X = \frac{\lambda_{qd} + \frac{1}{3}\lambda_q(1-\omega)}{\lambda_{qd} + \lambda_q\left(1 - \frac{2}{3}(1-\omega)\right) - \lambda_d\left(1 - \frac{1}{3}(1-\omega)\right)} \tag{2.9}$$

2.3.3 Observable Rates of Capture and Fusion

The expressions for the observable rates of fusion and capture neutrons are

$$R_f(t) = \lambda_d N_d(t) + \lambda_q N_q(t) \tag{2.10a}$$

$$R_c(t) = \Lambda_d N_d(t) + \Lambda_q N_q(t) \tag{2.10b}$$

These two equations may both be re-expressed as the sum of two exponential functions

$$R_f(t) = N_0 \left[\lambda_d \left(\frac{1}{3} + \frac{2}{3}X \right) e^{-\lambda_1 t} + \frac{2}{3} \left(\lambda_q - \lambda_d X \right) e^{-\lambda_2 t} \right] \tag{2.11a}$$

$$R_c(t) = N_0 \left[\Lambda_d \left(\frac{1}{3} + \frac{2}{3}X \right) e^{-\lambda_1 t} + \frac{2}{3} \left(\Lambda_q - \Lambda_d X \right) e^{-\lambda_2 t} \right] \tag{2.11b}$$

Note that at experimental conditions $\lambda_q > \lambda_d$, so the second term of equation 2.11a is positive, but $\Lambda_q < \Lambda_d$ and X is of order unity, so the second term of equation 2.11b is negative. Also note that both equations depend on the same λ_1 and λ_2, so these two parameters may be determined by fitting one of the time distributions, then plugged into the other time distribution to constrain the free parameters.

Experimentally, fusion neutrons are much more abundant than capture neutrons. This is due to λ_d and λ_q being orders of magnitude larger than Λ_d and Λ_q, and due to the fusion neutrons being mono-energetic with energy well within the sensitive range of the neutron detectors, while the capture neutron spectrum extends outside of the sensitive range of the detectors especially at low energies (due to gamma contamination, see section 5.4).

Chapter 3 Experimental Setup

The MuSun experiment took place at the Paul Scherrer Institute (PSI) in Villigen, Switzerland. The Swiss Muon Source (SμS) at PSI uses the highest intensity continuous proton beam in the world [37] to produce multiple continuous, high intensity muon beams. These beams may be operated in either μ^- or μ^+ mode. Thus, PSI has served as an ideal location for the MuLan, MuCap, and MuSun experiments.

MuSun used the πE3 beamline at PSI for runs 1-4, but was moved to the πE1 beamline in 2012. Run 6 was the first production run of MuSun in its new location, and ran from September to November of 2013. At the time of this writing, MuSun has completed run 7 in 2014 and run 8 in 2015 which completes the MuSun production data taking. A diagram of the πE1 area and a photograph of the MuSun apparatus can be seen in figure 3.1.

MuSun uses a kicked muon beam combined with a high-efficiency, multi-component entrance counter to introduce pile-up-protected muons-on-demand to a cryogenic, ultra-pure deuterium gas target. The deuterium serves as the active target in a time projection chamber (TPC) used to positively identify muon stops in the gas. The TPC is also used to identify muon catalyzed fusion and muon transfer to gas impurities. Electrons from muon decay are identified using a multi-stage electron hodoscope. The muon disappearance rate is defined by the time difference between the incoming muon and the outgoing electron. Neutrons are detected by multiple liquid scintillators. A diagram of the configuration of the entrance detectors, TPC, and electron detectors can be seen in figure 3.2.

3.1 Beamline

The ring cyclotron at PSI produces a continuous 590 MeV proton beam with a current of 2.2 mA. This beam is incident on a graphite production target producing charged and neutral pions which rapidly decay. The primary decay channels are,

$$\begin{aligned} \pi^+ &\rightarrow \mu^+ + \nu_\mu \\ \pi^- &\rightarrow \mu^- + \bar{\nu_\mu} \\ \pi^0 &\rightarrow \gamma + \gamma \end{aligned} \tag{3.1}$$

for charged and neutral pions. Muons and pions are extracted from this point into several beamlines for various experiments. As the beam is initially a mixture of muons and electrons of both charges, μ^- (or μ^+) must be selected for. Momentum and charge selection for the beam are done upstream of the πE1 area with a momentum slit. Electrons are removed from the beam using a crossed E-B-field velocity selector (separator) described below.

The muon beam is tuned to a momentum of 37.4 MeV/c with a $\Delta p/p$ of 1.5% [38]. This momentum is chosen to center the muon stopping distribution within the TPC. Figure 3.3 shows a typical measurement of the muon beam spot in the entrance

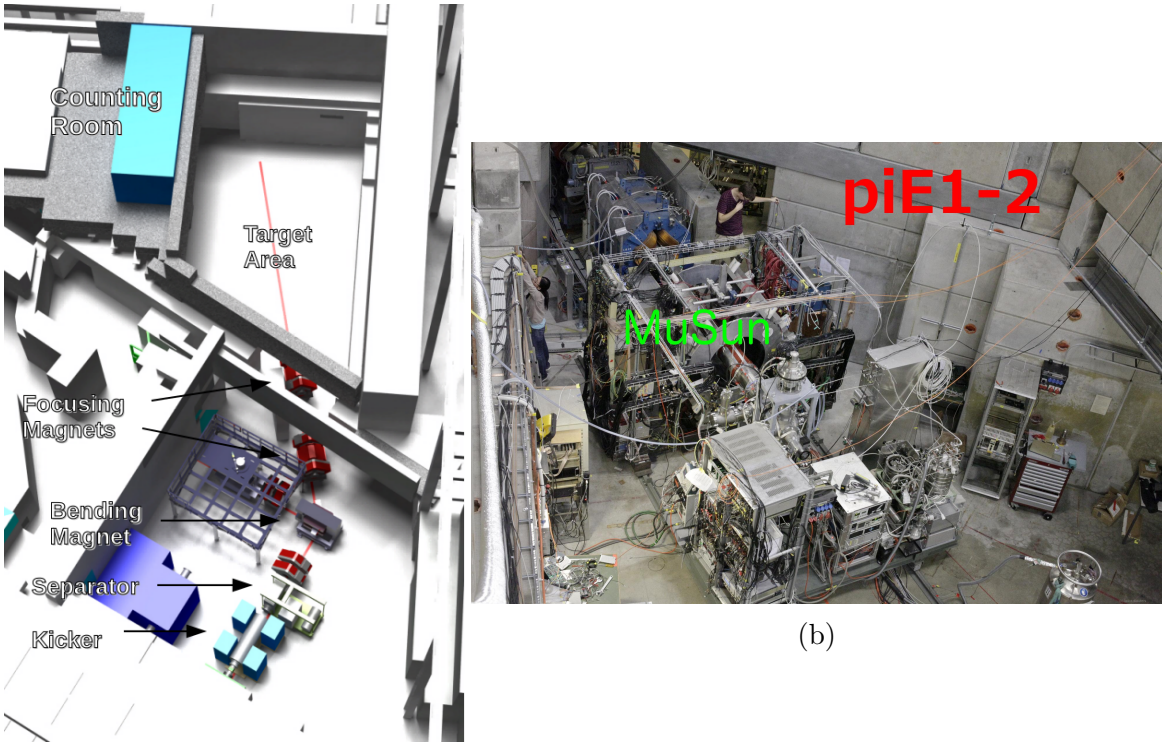

(a) (b)

Figure 3.1: The πE1 area of the PSI experiment hall where MuSun was located for run 5 through run 8. (a) CAD drawing of the area. The beamline, shown in red, enters from the bottom of the picture. The MuSun apparatus is not pictured. (b) Photograph of MuSun. The camera is looking upstream, so the beam enters from the top left of the picture. The detector assembly is the large cylindrical structure near the center-left of the image. The gas purification and cryogenics equipment is in the bottom-center of the image. In this image, the TPC and the attached purification/cryo assembly are partially removed from the detector assembly. (image ref. [5])

detector and muon stopping distribution in the TPC during run 6 production data taking.

3.1.1 Electrostatic Beam Kicker

The incoming muon beam passes through a parallel plate, E-field beam kicker. The function of the kicker is to maximize the rate of pile-up-free muon entrances. Muon pile-up protection is further ensured by a multi-component, high efficiency entrance detector described in section 3.2.

This kicker was initially built at TRIUMF for the MuLan experiment. Each plate is 75 $\times$ 20 cm with operating voltage of $\pm$12.5 kV per plate (for a total voltage difference of 25 kV) and is capable of switching at a frequency of up to 50 kHz with a rise time of 45 ns [39]. The kicker is triggered by a high efficiency scintillating

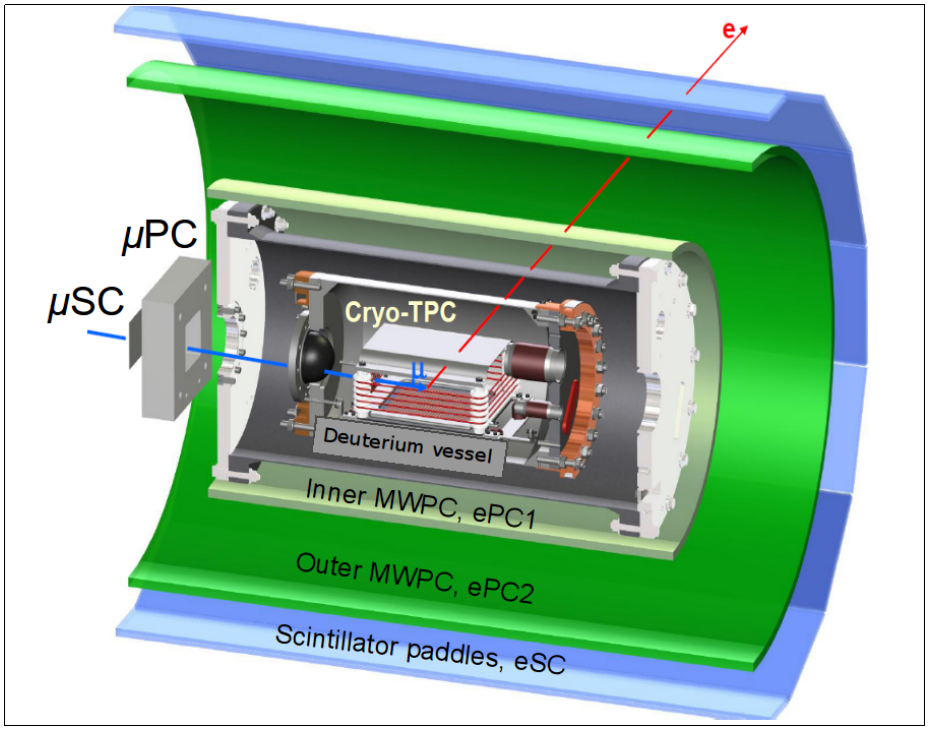

Figure 3.2: CAD drawing showing the configuration of entrance detectors (μSC and μPC), TPC, deuterium vessel, and electron detectors (ePC1, ePC2, and eSC). The neutron counters are not pictured here. The blue and red lines show a typical flight path for an incoming muon and an outgoing electron. (Image ref. [4])

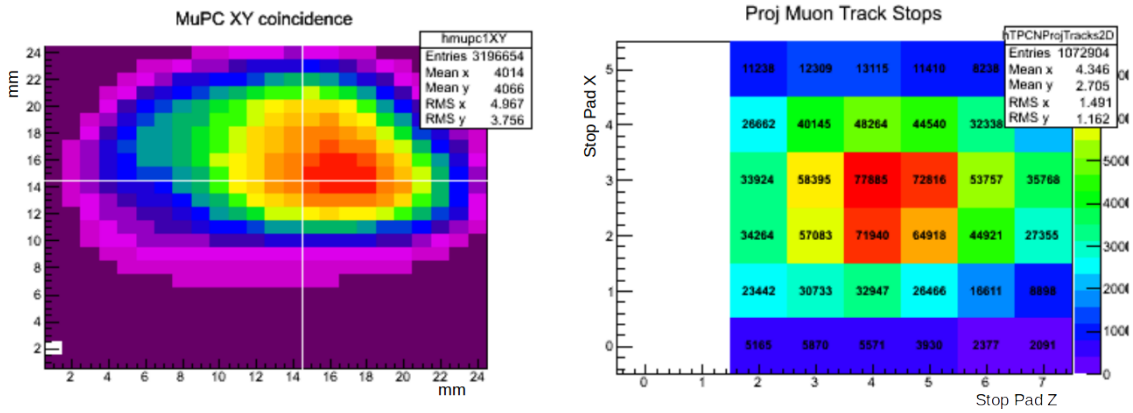

(a) (b)

Figure 3.3: (a) Muon beam spot during early run 6 production. The μPC is slightly off center from the collimator, so the white cross-hair shows the center of the beam spot. The pixel size is 2 mm×2 mm. (b) Position of muon track stops in the TPC during early run 6 production. The beam enters from the left. The TPC anode is divided into 48 pads. Since a muon track is defined by at least three pads, a track stop cannot occur in the first two columns.

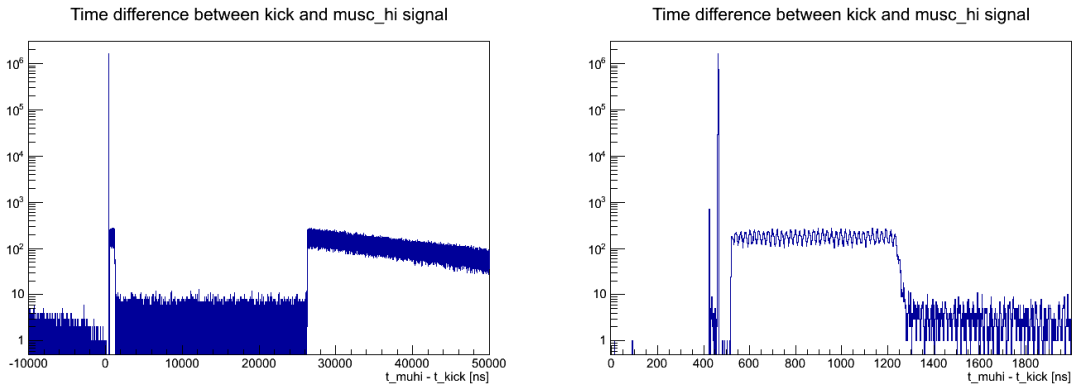

Figure 3.4: Kicker activation time relative to the muon entrance time (in μSC). The 800 ns plateau shortly after t=0 is due to the kicker activation delay. The 25 μs valley is the period during which the kicker is on. The ratio of the level of the plateau to the level of the valley ($\sim$85) is the extinction factor. These two histograms show the same data on different time scales.

plastic muon entrance counter (see section 3.2). Once activated, it kicks the muon beam off axis for 25 μs. Since the μ^- lifetime is 2.2 μs, this ensures a less than 1 in 10^5 probability of muon pile-up due to long-lived muons. There is an 800 ns delay between the muon detection and beam reduction due to signal processing and transmission time and muon time-of-flight. This activation sequence puts an upper limit on the muon entrance rate of about 38 kHz. During run 6, the muon entrance rate was 22-24 kHz.

The figure of merit for the effectiveness of the kicker is the extinction factor, defined as the muon rate while the kicker is off (beam on axis) to the muon rate while the kicker is on (beam off axis). During run 6, an extinction factor of 70-90 was achieved. Tuning the beam properties for a very high extinction factor is not practical, as it would require significantly reducing the muon entrance rate. Since muon pile-up can be eliminated by the entrance counters (see below), a balance is struck between kicker extinction and muon rate to maximize the rate of pile-up free muon entrances. Figure 3.4 shows the muon entrance time relative to the kicker activation time. The kicker extinction, activation time, and activation delay can all be seen in this histogram.

3.1.2 Velocity Separator

As described above, the initial beam produced at the graphite target is a mixture of muons and electrons of both charges. Before entering the πE1 experimental area, the beam passes through three turns which select for charge, one of which includes a momentum slit. Thus, the muon beam is contaminated with a large number of high velocity electrons with equal momentum.

To remove these electrons, a crossed E-B-field velocity selector is placed in the beam line directly downstream of the kicker. This separator is configured to deflect

electrons in the same direction as the kicked beam. This reduces the rate of beam electrons to ∼2 kHz, more than an order of magnitude lower than the muon rate.

After the separator, the muon beam passes through a 38^o turn. This turn was necessary due to the geometry of the πE1 area, and due to the shared use of the πE1 beam with the Dolly experiment. It was discovered during run 6 that the beam-dependent neutron background is significantly reduced in comparison with run 4 (ref. [1]). This background reduction may be due to this post-kicker, post-separator turn in the muon beamline.

3.2 Muon Entrance Detection

Precise muon entrance identification is essential to the MuSun experiment, as the muon entrance defines the start time for the lifetime measurement and also triggers the kicker. A robust pile-up veto is also essential for an accurate lifetime measurement. To this end, muon entrances are identified with a high efficiency, multi-component entrance detector.

3.2.1 Muon Scintillator

Incoming muons pass into air through a 75 μm mylar window at the end of the beam pipe. They then pass through a 250 μm thick plastic scintillator (muSC or μSC) which has timing precision at the nanosecond scale with leading edge discriminators and sub-nanosecond scale when fitting pulse shapes. The efficiency of the muSC is difficult to determine precisely, but during MuCap (which used the same entrance counter) the inefficiency was determined to be on the order of 10^{-4} [6].

The analog signal from the PMT attached to the muSC plastic scintillator is digitized by an 8-bit waveform digitizer (WFD) with a 25 MHz sampling rate. The signal is also digitized by a CAEN V767 time-to-digital converter (TDC). The TDC has two thresholds, one at 310 mV and one at 1090 mV, referred to as muSClo and muSChi respectively, correspond to electron and muon pulses. (Note that a muon pulse will also trigger the muSClo.) Two copies of the muSChi are recorded by the TDC as a cross-check. The muSChi signal defines the muon entrance, sets the start time of the lifetime measurement, and triggers the kicker.

3.2.2 Muon Veto Scintillator and Beam Collimator

Immediately upstream of the muSC is the muSCa, a 2 mm thick plastic scintillator with a 40 mm diameter circular hole. This scintillator is backed by a 1 mm thick lead collimator, also with a 40 mm diameter hole, on the downstream side. The muSCa provides a veto on halo muons and reduces backgrounds due to halo particles. Like the muSC, the muSCa is digitized by an 8-bit WFD.

3.2.3 Muon Proportional Chamber

Downstream of the muSCa and muSC is the muPC, a multi-wire proportional chamber composed of two layers of 24 anode wires each, one oriented horizontally and the

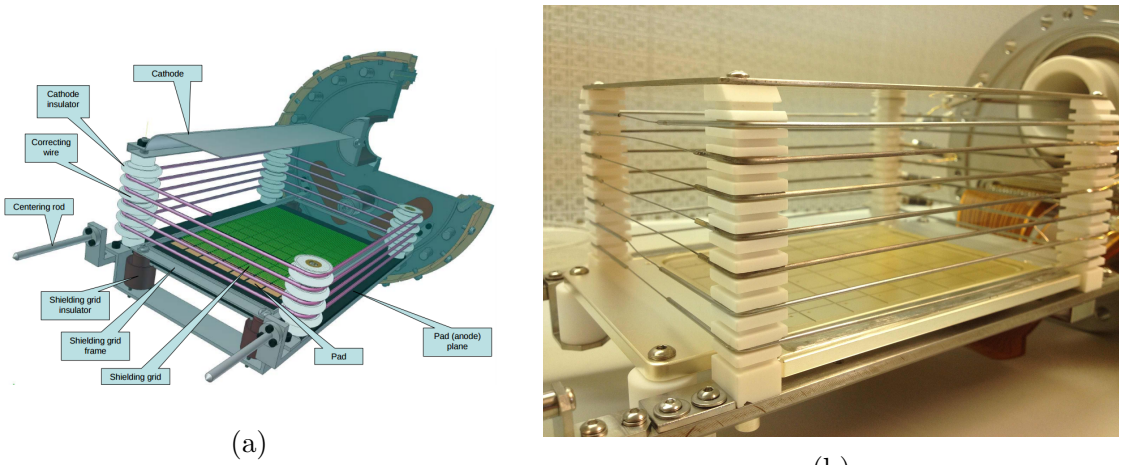

(a) (b)

Figure 3.5: (a) Conceptual diagram of the TPC. (image ref. [4]) (b) The TPC which was installed during run 6.

other vertically. The wire pitch is 2 mm, giving a 4.8×4.8 cm^2 grid for x-y position detection of the muon entrance. Each anode layer is surrounded by two 25 μm aluminized mylar cathode layers held at -2.5 kV. The entire array is sandwiched between two 50 μm mylar windows. The detector is filled with an argon, ethane, freon gas mixture for ionization. The muPC signals are digitized by TDCs.

3.3 D_2 Time Projection Chamber

The deuterium target chamber is also a time projection chamber (TPC) with the deuterium acting as the ionizing gas. Muons traveling through the gas ionize the deuterium molecules, with the amount of ionization proportional to the energy loss of the muon. Liberated electrons drift towards the anode with a velocity of about 5.3 mm/μs. This allows for determination of the vertical position of the incoming muon. By combining this information with the horizontal positioning provided by a segmented anode (pad plane), it is possible to do a full 3D reconstruction of the muon track. The primary function of the TPC is to identify muon stops in the gas. It has also proven to be an excellent detector for identifying helium recoils from muon catalyzed fusions and for identifying muon transfers to high Z contaminants.

3.3.1 TPC construction

The TPC was upgraded for run 6. In the upgraded TPC, high Z materials, primarily tungsten and silver, were used for as many components as possible. The lifetimes of μW and μAg atoms are 78 ns and 87 ns respectively. This ensures that muon capture on materials in the TPC happens very rapidly, thus minimally interfering with the lifetime measurement. Figure 3.5 shows a diagram and a photograph of the TPC.

The anode of the TPC is 95.5×125.5 mm and is composed of a 40 μm silver coating on a hot-fired alumina substrate [40]. It is divided into a 6×8 array of pads

approximately 16×18 mm^2 on a side. The anode is situated at the bottom of the TPC in the xz-plane with the long edge parallel to the z-axis.

A Frisch grid is mounted 1.4 mm above the pad plane. It's purpose is to screen the anode from the field of the slow-moving positive deuterium ions, as charges only become visible to the anode after passing the grid. It is composed of 25 μm gold plated tungsten-rhenium wires with a grid pitch of 400 μm [41] (green layer in figure 3.5). These wires are hard soldered to a silver plated tungsten frame. This grid was held at a voltage of -3.6 kV relative to the pad plane during run 6 production. The TPC Cathode is mounted 71 mm above the Frisch grid and held at -80 kV. It is constructed from a 100 μm sheet of silver glued to an aluminum frame.

The TPC volume is surrounded by seven tungsten field-shaping wires. These are held at a pairwise voltage difference of 10kV using a voltage ladder. The wires have a thickness of 1.5 mm for most of their length, but are reduced in thickness at the front of the TPC, where the beam enters, to reduce the amount of muon capture on the wires. The cathode and field shaping wires are supported by four posts made of MACOR®, a machinable glass-ceramic composed of 55% fluorophlogopite mica ($KMg_3AlSi_3O_{10}F_2$) and 45% borosilicate glass (SiO_2 and B_2O_3) [42]. These posts and the aluminum cathode support frame are the main low-Z components in the TPC.

3.3.2 Cryogenic Pre-Amplifiers

During run 4, the electronics chain of the TPC was found to have an RMS electronic resolution of 29 keV and a resolution of 40 keV for delayed ^{3}He fusion pulses [40], which have energies around 300-400 keV. To address this, a set of cryogenic pre-amplifiers were custom built and installed during run 5, making run 6 the first production run with these pre-amps in operation. These were mounted in the insulation vacuum surrounding the gas chamber and held at 140 K. They were found to improve the electronic resolution to better than 10 keV and the ^{3}He resolution to 17 keV [40].

3.3.3 TPC Signal Digitization

The signals from the 48 channels of the TPC pad plane are digitized using 8-bit, 25 μs^{-1} WFDs. Two signals are digitized for each channel, one at high gain and one at low gain. This is done to increase the dynamic range of the TPC, as signals above 1 MeV will overload the high gain WFDs, but small pulses will fail to trigger the low gain WFDs. Pulses are recorded in islands which are 88 samples long; however, if the signal is still above threshold at the end of an island, another island is recorded. This is continued until the signal drops below threshold.

3.3.4 TPC Pressure Vessel

The TPC is contained in a cylindrical pressure vessel of 2.5 mm thick aluminum. The vessel has an outer diameter of 20.2 cm and a length of 36 cm. Muons enter the deuterium vessel through a 0.5 mm thick hemispherical beryllium window. The rear

flange of this vessel is stainless steel and is penetrated by the feedthroughs for TPC electronics and gas circulation. The rear flange is sealed in place with indium wire O-rings. This vessel is housed inside a larger cylindrical aluminum vacuum vessel for cryogenic insulation. The front of the insulation vessel has a mylar window for muon entrance.

3.3.5 Gas cryogenics

The deuterium gas is held at a temperature of 31 K and a pressure of 5.1 bar so as to achieve a density of 5% of liquid density. Cryogenic conditions are achieved by cycling 27 K liquid neon from a coldhead and massive copper condenser through a series of copper pipes surrounding the deuterium vessel.

3.3.6 Gas Purity

Isotopic purity of the deuterium gas is accomplished by diffusion before the experiment. The gas is cycled through a diffusion column multiple times until ppm level purity is achieved.

Chemical purity is achieved by the Circulating Hydrogen Ultra-high Purification System (CHUPS) developed by the Petersburg Nuclear Physics Institute [43]. CHUPS continuously circulates the target gas through a synthetic zeolite filter. This system was originally built for the MuCap experiment and has been adapted for MuSun.

The primary contaminants are atmospheric compounds: N_2, O_2, and H_2O. To achieve the desired 1.5% precision measurement of Λ_d, these contaminants cannot exceed 6 ppb. At the experimental conditions of 31 K and 5.1 bar, the most abundant of these is N_2, having a vapor pressure of 20 ppb. Continuous circulation of the gas through the zeolite filter can clean nitrogen to the level of $\sim$1 ppb. The chemical purity of the gas is checked periodically using gas chromatography.

Unfortunately, at the end of run 6 it was discovered that the zeolite filter was saturated with water vapor meaning it was not effectively filtering. This makes the run 6 data unsuitable for a lifetime measurement. However, the data are still well suited for a neutron based analyses presented here.

3.4 Electron Detection

3.4.1 Electron proportional chambers

The target chamber is surrounded by two concentric, cylindrical multi-wire proportional chambers (ePC1 and ePC2). These serve as the primary instruments for electron track reconstruction. These were originally built for the MuCap experiment. The inner chamber, ePC1, has a radius of 19.2 cm and active length of 58 cm, and ePC2 has a radius of 32 cm and an active length of 80 cm. Each ePC consists of a layer of anode wires (512 in ePC1 and 1024 in ePC2) running parallel to the beam axis sandwiched between two layers of cathode strips. These strips are arranged in a helical "candy stripe" pattern at an angle of approximately 45^o to the beam axis, with

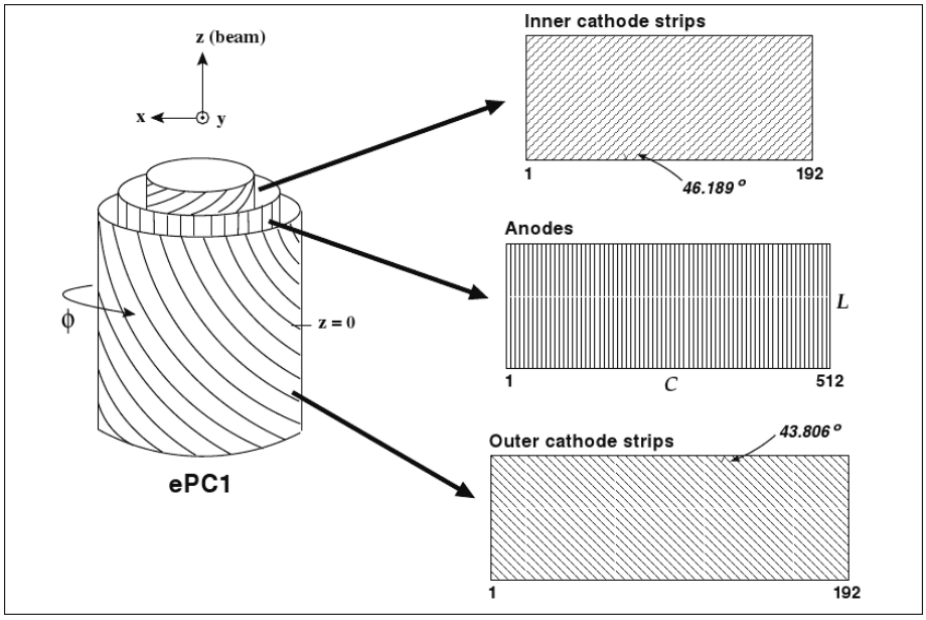

Figure 3.6: Diagram of ePC1 showing the anode layer (central layer) and inner and outer cathode layers. The angles of the cathode strips are chosen so that each covers π of the full chamber circumference. The configuration of ePC2 is similar. (image ref. [6])

inner and outer layers having opposite helicity (fig. 3.6). The width of the cathode strips and the spacing of the anode wires are both approximately 6 mm. Thus, this configuration gives complete (ϕ, z) positioning of the electron track at two different radii with a precision of about 6 mm.

Several charge-integrating preamp-discriminator cards are mounted along the edges of the proportional chambers for signal discrimination and amplification. These discriminated signals are read into custom designed, FPGA based data acqusition modules, called compressors. The compressors digitize the time and channel number of discriminated ePC signals.

3.4.2 Electron scintillators

A multi-panel scintillating hodoscope (eSC) surrounds ePC2. The eSC is composed of sixteen units, dubbed "gondolas" due to their shape. Each unit has two layers of 5 mm thick scintillating plastic, dimensions 90×16 cm^2. The sixteen gondolas are arranged in a cylindrical configuration (radius 39 cm). Combined they cover about 75% of the full solid angle.

Each scintillator has a 1.5" photomultiplier tube at each end, giving each gondola four PMTs. A best quality electron is defined by a 4-fold coincident detection ($\Delta t <$ 40 ns) by all PMTs on a single gondola. The full configuration of the TPC, ePC1, ePC2 and the eSCs can be seen in figure 3.2.

An electron in the eSC hodoscope defines the stop time of the lifetime measurement, so high accuracy is also required here. Like with the muSC, the signal from each

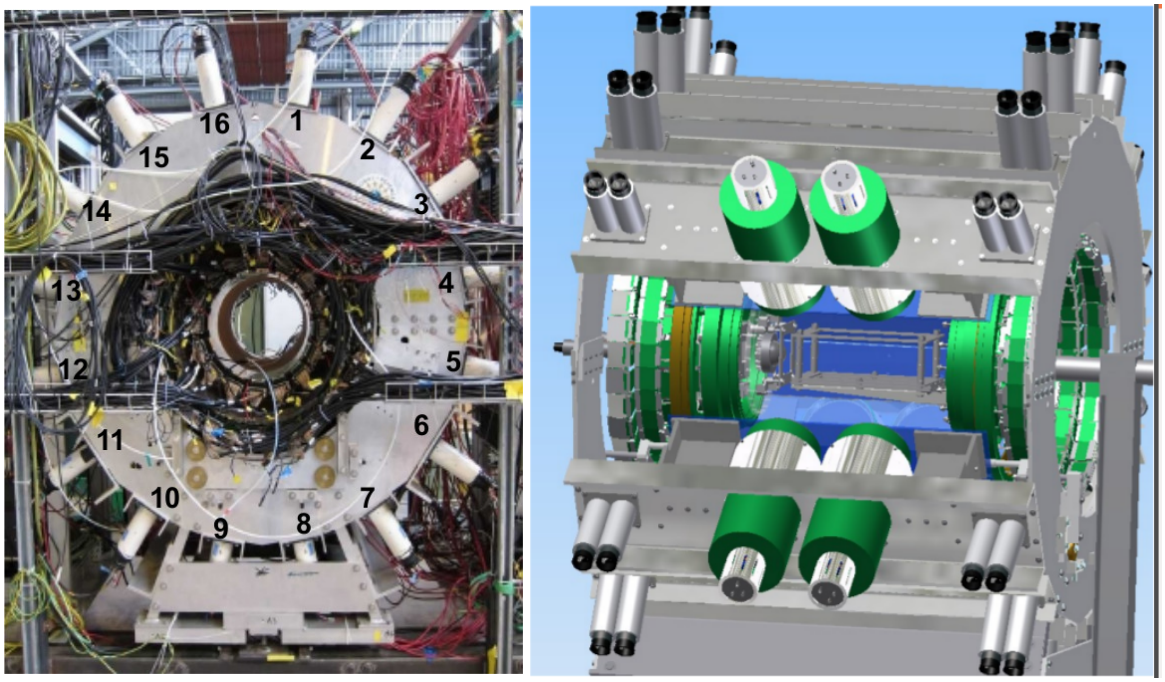

(a) (b)

Figure 3.7: (a) Labeling system for gondolas. The camera is looking upstream (image ref. [1]) (b) Position of neutron detectors in relation to gondolas. The neutron detectors can be identified by the large green cylinders representing the neutron PMTs.

of the 64 eSC PMTs is digitized by both 8-bit, 25 μs^{-1} WFDs and by CAEN TDCs. The signal recorded by the TDC defines the electron time, with 1.25 ns precision on leading edge detection.

3.5 Neutron Detector Array

Neutrons are detected using eight liquid scintillator cells arranged in four pairs outside of the eSC. This places them approximately 42 cm from the center of the TPC. These pairs are mounted behind gondolas 3, 6, 11, and 14 with one upstream and one downstream, thus they are labeled NU3, ND3, NU6, ND6, NU11, ND11, NU14, and ND14. Figure 3.7 shows the labeling system of the gondolas and the positions of the neutron detectors.

Each cell is a 13 cm diameter by 13 cm height cylinder containing approximately 1.2L of a liquid hydrocarbon solution composed primarily of xylene. Each is mounted to a 13 cm photomultiplier tube, of which six are commercially produced Bicron BC501A units, and two (NU11 and ND11) were custom built. Combined, they cover approximately 4.5% of the solid angle. Besides backgrounds from the accelerator and beam, the two sources of neutrons in MuSun are μd capture(eq. 1.3) and muon catalyzed fusion (eq. 2.2a). Capture neutrons have a broad energy spectrum extending up to about 50 MeV, while fusion neutrons are mono-energetic at 2.45 MeV. The

neutron detectors are sensitive to neutrons with an electron-equivalent recoil energy (see section 5.1) of up to about 2 MeVee, so high energy capture neutrons are undetected. Furthermore, gamma ray interference limits the ability to discriminate low energy neutrons ($\lesssim$ 200 keVee, which corresponds to $\sim$ 500 keV neutrons). Due to these limitations and detector efficiency, approximately 1% of neutrons are detected.

The neutron PMTs are particularly sensitive to stray magnetic fields. To protect against this, each was surrounded by a sheet of 160 μm mu-metal. Mu-metal is a nickel-iron alloy with very high magnetic permeability and coercivity.

These PMTs are read out into custom-built 12-bit flash-analog-to-digital converters (FADC). A detailed discussion of neutron detector calibration and neutron-gamma discrimination is given in chapter 5.

3.6 Clock

As the primary result of the MuSun experiment will be a lifetime measurement, precise timing is essential for success. MuSun uses a 500 MHz master clock to which all other clocks (such as FADCs and WFDs) are slaved. During run 6, due to a malfunction in the master clock, it instead operated at 450 MHz. The clock is precise to 1 Hz, thus giving a precision of $\sim$2 ppb. The clock is blinded by detuning up to 0.5%. The blinding for each production run is unique. At the time of this writing, all production data is still blinded.

It should be noted that the ratio Λ_q/Λ_d of capture rates from the two μd hyperfine states, which is the main result of this dissertation, is only very weakly affected by this blinding. The precise effect of the blinding on this result is discussed in chapter 8.

3.7 Run 6 Summary

The MuSun experiment took place over the course of eight runs from 2008 to 2015, with an additional ninth run planned for a muon catalyzed ^{3}He fusion study. Runs 1, 2, and 3 conducted in 2008–2010 were commissioning and engineering runs. Run 4, conducted in 2011, was the first run to collect production quality data. Between runs 4 and 5, MuSun was moved from the πE3 beamline to the πE1 beamline, with run 5 being an engineering and commissioning run for the new location. Run 6 was the first production data taking run in the new beamline. The statistics gathered during run 6 were severely limited by an extended shutdown of the proton beam. A detailed summary of run 6 is given below. Runs 7 and 8, which took place in 2014 and 2015, were both highly successful data taking runs, accumulating $\sim 10^{10}$ best quality muon stops combined.

MuSun run 6 took place in the Fall of 2013. The first three weeks of beam time were used for preparation of the detectors, front-end electronics and the data acquisition system, as well as beam tuning and final infrastructure installations in the new area. Studies were also conducted to assess the performance of the newly installed cryogenic pre-amps. During this time, the original TPC assembly used for

runs 1-5 was still in place while the new TPC was being prepared for installation. During this time, it was discovered that the waveform digitizers for the eSC detectors would intermittently drop bits. This problem was able to be fixed by reducing the master clock from 500 MHz to 450 MHz (before blinding).

Once the new TPC was installed, it was quickly discovered to have a leak from the deuterium vessel into the insulation vacuum. The leak was most likely either in the indium seal, or in the multi-pin electronic feedthrough flange. It was decided that the best fix would be transfer the new TPC assembly into the original deuterium vessel. This fix was found to be successful.

Unfortunately, shortly after installation of the new TPC, the main proton beam had to be shut down due to severe overheating of one of the RF cavities. This problem ultimately resulted in three weeks of downtime before it was eventually fixed.

Once the proton beam came back online, production data resumed after a brief period of beam tuning and system checks. Uninterrupted data taking took place over a period of about three weeks. During the first week, the new TPC operated at a cathode voltage of -85 kV and a grid voltage of -3.7 kV; however, this was found to cause sparking between the grid and the pad plane, so these voltages were lowered to -80 kV and -3.6 kV respectively. Thus, we were able to have about two weeks of uninterrupted μ^- data taking at stable conditions. After a routine beam shutdown, approximately one week of μ^+ data were collected. The beam was then changed back to μ^- and a small amount of production data were collected before another 10-day proton beam shutdown due to a problem with a flat-top cavity in the cyclotron.

During this second shut-down, the TPC was warmed. It was discovered that the zeolite filter was saturated with water. This means that instead of the N_2 impurities being at the anticipated level of $\sim$1 ppb, it was instead at the vapor pressure level of $\sim$20 ppb. The TPC was again cooled in preparation for final systematic data taking; however, this last heating and cooling cycle caused a section of the solder holding the grid wires to crack so that some of the wires lost tension and were hanging down onto the pad plane.

Since there was only a small amount of beam time remaining, the old TPC was installed and operated at 75 kV. The deuterium was doped with $\sim$2.5 ppm of N_2 as a systematic test. These tests included temperature and density scans on the doped gas.

Chapter 4 Data Acqusition and Preperation

4.1 Data Acquisition

MuSun uses the MIDAS data acquisition system (DAQ). Signals are digitized using a variety of methods, depending on the detector (described in sections 3.2–3.5), and are stored in MIDAS banks. All digitizers are slaved to the 450 MHz master clock. These data are analyzed using ROOT in a two-stage process.

Digitized signals are collected by multiple dedicated front-end computers. These computers accumulate data in buffers for approximately 10 ms. Data taking is then paused briefly while these buffers are recorded by a dedicated back-end computer and organized into MIDAS banks. This cycle is synchronized across all front-ends. A single such cycle of data taking is referred to as a MIDAS block.

This cycle is repeated until approximately 1.6 GB of data are recorded, which typically takes about three to four minutes. Once this data limit is reached, data taking is paused, typically for $\sim$10 s, while the recorded events are written into a MIDAS file (.mid format). A single such set of data is called a run.

Runs are recorded to a RAID disk array before being redundantly copied to a collection of conventional hard drives and a PSI server. Runs are then transferred off-line to a mass storage server (named Ranch) at the Texas Advanced Computing Cluster (TACC) at the University of Texas. Ranch uses an automated tape archive for long-term storage.

4.2 Stage I Analysis: Mu

Data analysis primarily takes place on a high-performance supercomputer at TACC named stampede. Analysis is done using the ROOT framework. MIDAS files for runs are processed using a custom-written, ROOT-based program called mu. Mu performs multiple tasks.

- It translates the raw data from the MIDAS files into physics objects.
- It applies calibrations, time alignments, and spatial alignments of detectors.
- It organizes the data into ROOT TTree objects, called MuSun events, around muon entrances (as defined by the muSC).
- It generates several histograms used for diagnostics.
- During the experiment, mu is used to generate multiple histograms for online monitoring.

4.3 Stage II Analysis: Mta

Tree files produced by mu are then processed through a second-stage analysis software called mta (mu tree analysis). Mta is used primarily to define physics events involving multiple detectors, such as muon entrances, muon stops, and electron tracks. A few of the key event definitions are described below. Mta is also where the bulk of the analysis is done.

4.4 Muon Entrance Definition

A "best" muon entrance is defined by the following criteria:

- A muSC pulse which crosses the muSChi threshold. This defines the time of the muon entrance
- A coincident detection ($\pm$190 ns) on one horizontal and one vertical wire of the muPC.
- A pile-up veto ($\pm$25 μs) on muSCa pulses, muSC pulses, and muPC XY coincidences. Additional pulses on individual muPC wires were not vetoed due to noise.
- A kicker activation with timing consistent with the muon entrance.

The 25 μs kicker activation time, combined with the explicit pile-up veto, defines a $\pm$25 μs event window around the muon entrance.

4.5 Muon Track and Stop Definitions

Muon stops in the deuterium gas are defined by their incoming track and by the energy deposited at the end of the track. As described in section 3.3, the anode of the target volume TPC is divided into a 6×8 grid of 1.6×1.8 cm^2 pads. This allows for the determination of the xz-coordinates of the muon track. The y-coordinate is determined by the drift time of ionization electrons.

4.5.1 Stop Energy

When a massive charged particle passes through matter, it deposits its energy in the material via ionization causing the particle to decelerate. Thus, the energy deposited per length increases with distance traveled until the particle comes to a stop, depositing most of its energy in a peak at the end of the track. This characteristic profile of dE/dz is known as a Bragg curve. Figure 4.1 shows a simulation of a muon stop in the TPC.

We define E0 to be the energy of all pulses on the final pad of a muon track (up to 2 μs after the initial pulse) and E1 to be the energy of all pulses on the pad preceding the stop pad. We include all pulses on these pads in these definitions so as to be agnostic as to which pulse was produced by the muon (rather than a ^{3}He recoil pulse

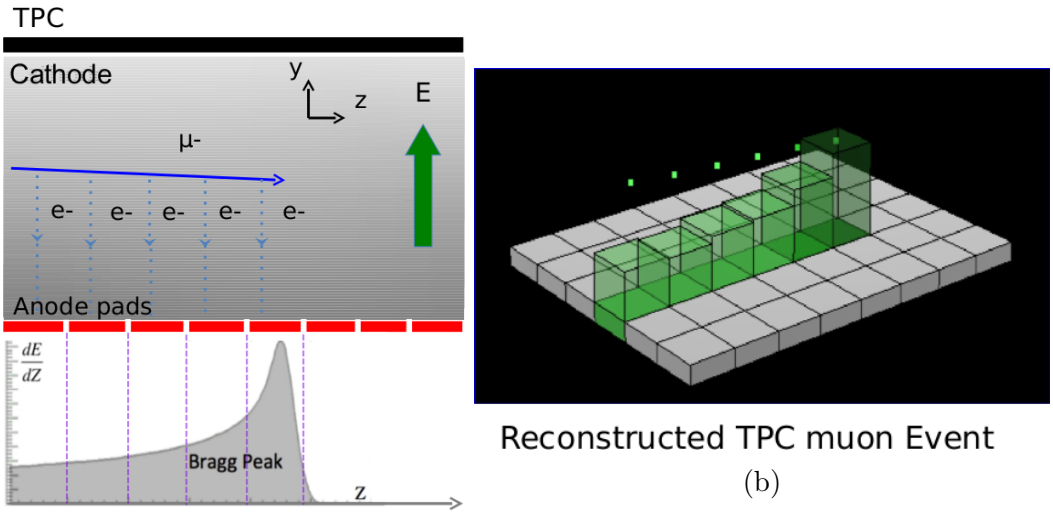

(a) (b)

Figure 4.1: Simulation of a muon stop in the TPC. The upper portion of figure (a) shows a YZ-projection of a muon track (solid blue arrow) and ionized drift electrons (dotted blue arrows) deposited on each anode pad (red bars), and the lower portion shows the rate of energy deposition per distance ($\frac{dE}{dZ}$) as a function of distance along the muon track. Figure (b) shows the energy deposited on each pad (green boxes) and the reconstructed position of the muon (green dots). Note that the majority of the ionization energy is deposited in the Bragg peak on the last pad. (image source [1])

which may follow the muon stop). The energy deposited in the deuterium gas by a stopping muon is roughly constant; however, since a muon may stop at any point on the final pad, the energy deposited on the final pad is not constant. Thus, we define a quantity called S-energy which is equal to $E0 + 2E1$. The S-energy of a muon stop in the gas was found to be constant for stops without a fusion. Figure 4.2 shows E0 vs E1 and S-energy of muon stops from run 6 data.

4.5.2 Track and Stop Definitions

To properly identify a muon stop in the deuterium gas, robust track and stop definitions are required. A muon track is defined according to the following criteria:

- The track must be at least three pads long in the z-direction. Thus, a muon stop may not occur in the first two columns of the pad plane.
- The separation in the z-direction between sequential pulses is two pads or less. This is to allow for tracks which may pass over the edge of two pads and thus not deposit enough energy on either pad to cross threshold.
- The separation in the x-direction between sequential pulses is one pad or less.

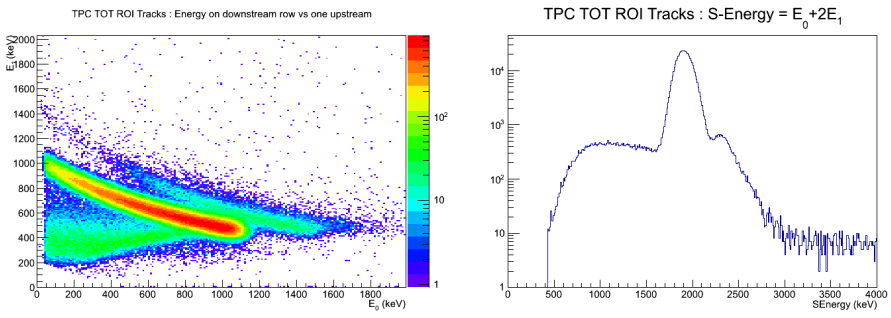

(a) (b)

Figure 4.2: (a) Plot of E1 vs E0 for muon stops in the fiducial volume. Note that most stops fall on a line with a slope of approximately -1/2. The low E1 feature are tracks that did not stop in the gas. The slightly higher energy feature are stops with a ^{3}He recoil. (b) Plot of S-energy (E0+2E1). That is, this histogram is a projection of figure (a) onto the line $2E1 - E0 = const$. The the same features can be seen here as in figure (a), those being tracks without a stop with S-energy below about 1700 keV, stops without a ^{3}He recoil peaked around 1900 keV, and stops with a ^{3}He recoil peaked around 2400 keV.

- The time difference between sequential pulses is 2 μs or less. This corresponds to a y-separation between sequential pulses of 1 cm or less.
- The S-energy of the muon stop must be at least 440 keV.
- To properly handle pulses that cross a pad boundary, an edge matching condition is applied. The leading edge of a pulse must be $\leq$1 μs from the trailing edge of the pulse on the preceding pad.
- The stop pad is defined as the last pad (in Z) of a track. If a track has pulses on two pads in the last column, then the pad with the higher energy pulse is defined as the stop pad.

To ensure that a muon stopped in the gas, a boundary veto is applied. Tracks ending on a pad along the edge of the pad plane are vetoed, as are tracks with the vertical position of the stop less than 1.5 cm (3 μs) from the cathode or anode. This defines the fiducial volume. Figure 4.3 shows a diagram of this stop definition. Furthermore, if there are two or more tracks following a single muon entrance, then all such tracks are vetoed. Defining this fiducial volume significantly reduces the low S-energy component of muon stops. That is, it eliminates tracks that do not have a Bragg peak due to not stopping in the gas (fig 4.4).

4.6 Electron Track Definition

A best quality electron track is defined according to the following conditions.

- A coincident detection by all four PMTs on a gondola ($\Delta t < 40$ ns).

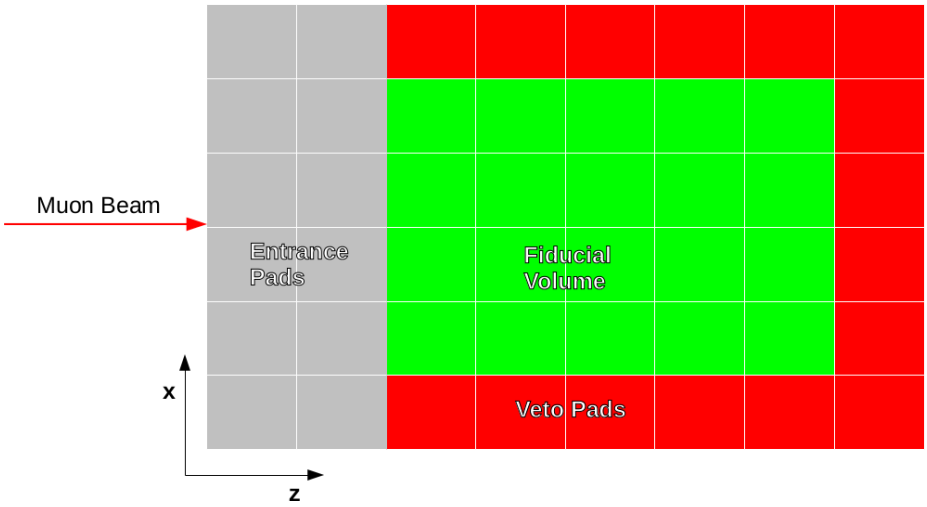

Figure 4.3: Fiducial volume of the TPC. The muon beam enters from the left. Since a muon track is defined by at least three pads, a stop cannot occur in the first two columns. An edge veto is applied to ensure that muons stop in the deuterium gas.

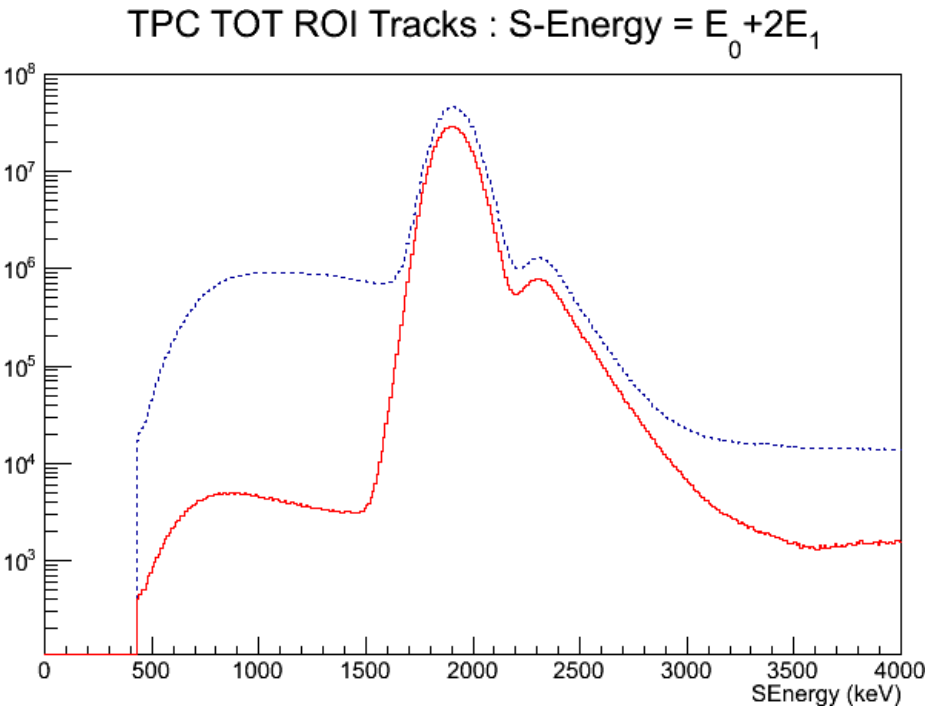

Figure 4.4: S-energy spectra for muon stops anywhere in the TPC (blue dashed line) or in the fiducial volume (red solid line). The fiducial volume cut significantly reduces the low S-energy component, showing the reduction tracks without a Bragg peak by several orders of magnitude.

- A detection in both electron proportional chambers. An electron in an ePC is defined by a detection in an anode wire and at least one cathode strip.
- The track must originate from the TPC.

During run 6, there was a significant amount of sparking in the ePCs. For this reason, in the analysis presented here, electrons are only defined by a gondola 4-fold coincidence. However, this is not a significant setback, as the final results presented here primarily use electrons as a veto condition, and a more relaxed electron definition is appropriate for a veto.

4.7 Data Set

A "golden" quality run is one during which all detectors and electronics were fully functioning, and all conditions were stable. Despite run 6 facing a host of setbacks (see sec. 3.7), approximately two weeks worth of golden quality production data were collected with the TPC cathode and grid voltages at -80 kV and -3.6 keV respectively, plus approximately one week of golden data with these voltages at -85 kV and -3.7 kV. Combined, this makes for a dataset of about 3000 golden quality μ^- production runs with approximately 2×10^9 μ^- stops in the D_2 gas. Approximately 500 runs of golden quality μ^+ data were also collected with about 2×10^8 μ^+ stops. Due to the nitrogen contamination, these data are not suitable for lifetime measurements; however, they are still well suited for the neutron analysis presented here.

Chapter 5 Neutron Event Selection

The MuSun neutron detectors are cells of a liquid scintillators with attached photo-multiplier tubes. The scintillating fluid is a solution composed primarily of xylene. Hydrocarbons such as xylene are well suited for neutron detection due to the multiple hydrogen atoms in their molecular structure. An incoming neutron scatters off of a hydrogen nucleus (i.e. a proton) and the recoiling proton produces ionization.

Since muon catalyzed fusion, $d + d \rightarrow {}^3He + n$, has two products, fusion neutrons are mono-energetic at 2.45 MeV. Muon capture (eq. 1.3), on the other hand, has three products (the two neutrons and a neutrino). Thus, capture neutrons have a broad energy distribution which is peaked at low energy, but extends up to $\sim$50 MeV.

The neutron detectors are also sensitive to gamma rays which Compton scatter off of molecular electrons. This process creates a significant background which must be removed, but it also provides a method for energy calibration.

The neutron detectors use custom built 12-bit flash-ADCs (FADC) for signal digitization. The FADCs have a 170 MHz sampling rate, so samples are 5.88 ns long. The total length of a pulse is about 70 samples. The maximum number of ADC levels per sample that can be digitized is $2^{12} - 1 = 4095$. This upper bound on the digitizable pulse amplitude roughly corresponds to a neutron pulse energy of about 1.5 MeVee. Work was done in reference [1] to recover highly energetic pulses which exceed this digitization limit using template fitting, but this method was found to be very computationally intensive with only nominal gains in high energy pulse recovery. For these analyses, overloaded pulses are excluded.

5.1 Energy Calibration

Calibration of the neutron detectors is done using two gamma sources of known energy, Cobalt-60 and Cesium-137. Co-60 emits two gammas at 1.17 MeV and 1.33 MeV. Cs-137 emits a single gamma ray at 662 keV. These gamma rays Compton scatter off of molecular electrons. The change in wavelength of the gamma ray due to Compton scattering is given by

$$\lambda' - \lambda = \frac{h}{m_e c}(1 - \cos\theta) \tag{5.1}$$

where λ is the wavelength of the incident photon, λ' is the wavelength of the emitted photon, m_e is the electron mass (511 keV), and θ is the scattering angle of the emitted photon. Thus, the maximum wavelength shift due to Compton scattering is

$$\lambda' - \lambda = \frac{2h}{m_e c} \tag{5.2}$$

for $\theta = 180^o$. Recalling that for photons $E = \frac{c}{\lambda}$, equation 5.2 can be rewritten in terms of the maximum energy transferred to the electron, known as the Compton

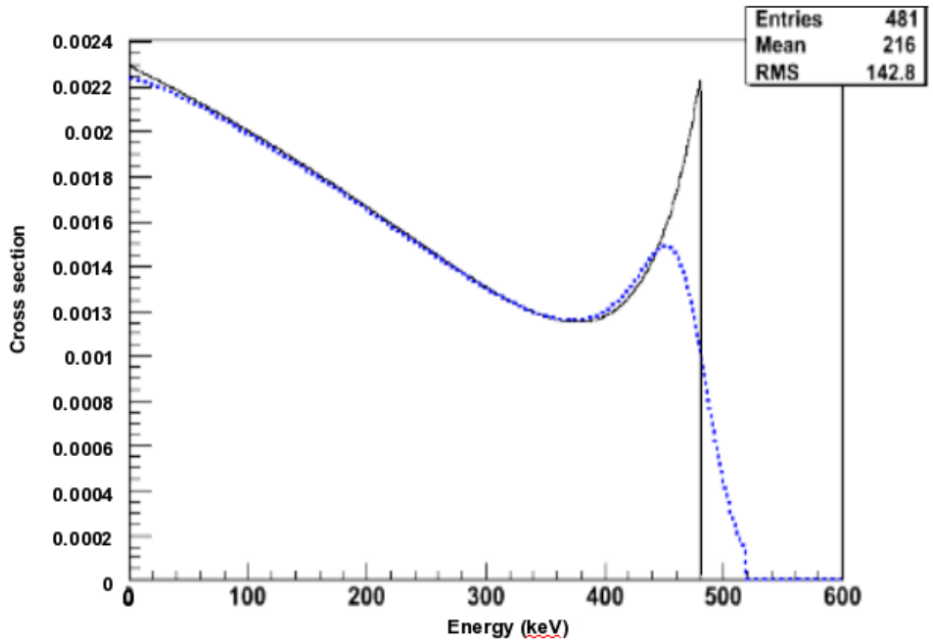

Figure 5.1: A Klein-Nishina distribution (solid black line) with the Compton edge at 482 keV and the same distribution convolved with a normal distribution with $\sigma = 20$ keV (dotted blue line) (image ref. [1]).

energy

$$E_C = \frac{2E_i^2}{m_e c^2 + E_i}, \tag{5.3}$$

where E_i is the energy of the incident photon.

The Compton energy (or Compton edge) of the 662 keV gamma ray from Cs-137 is 478 keV. In the case of Co-60, the two gamma rays at 1.17 MeV and 1.33 MeV have Compton energies of 0.960 MeV and 1.116 MeV respectively. However, these Compton edges are close enough together as to be indistinguishable, and will appear as a single, broader edge at approximately 1.04 MeV. Thus, the energy difference between the Compton edges for these two sources is 560 keV.

The differential scattering cross section of a photon incident on a free electron in lowest order quantum electrodynamics is given by the Klein-Nishina formula [44]. It can be expressed in terms of the kinetic energy of the recoil electron (E_T) as

$$\frac{d\sigma}{dE_T} = \frac{\pi r_e^2}{\varepsilon h\nu}\left(2 - \frac{2E_T}{\varepsilon(h\nu - E_T)} + \frac{E_T^2}{\varepsilon^2(h\nu - E_T)^2} + \frac{E_T^2}{h\nu(h\nu - E_T)}\right) \tag{5.4}$$

where r_e is the classical electron radius and $\varepsilon = \frac{h\nu}{m_e c^2}$. This function is rapidly increasing for E_T just below E_C and zero for $E_T > E_C$ (fig. 5.1).

Due to the finite energy resolution of the neutron detectors, we do not see a sharp Compton edge. Instead, the energy spectrum is well modeled by a Klein-Nishina distribution convolved with a normal distribution. However, a fit function based on the full convolution of a Klein-Nishina distribution and a normal distribution was found to frequently give pathological fits. Furthermore, we are only concerned with

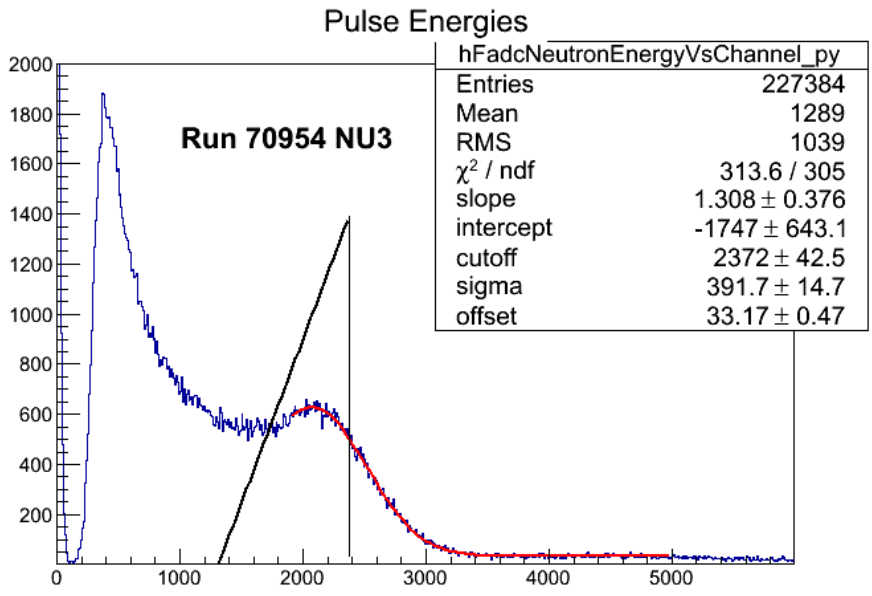

Figure 5.2: Example of a calibration fit. The red curve is the fit, the black lines show the piecewise linear function that was convoluted with a normal distribution to define the fit function. The vertical black line defines the Compton edge found by the fit. This is detector NU3 illuminated with Cs-137 from the end of run 6.

fitting the energy spectrum near the edge. Therefore, a simplified fit function was developed which was still sufficient for finding the Compton edge.

Near the Compton edge, to lowest order, the Klein-Nishina distribution becomes approximately linear. Thus, the fit function was defined by convoluting a normal distribution with the piecewise linear function

$$f(E) = \begin{cases} mE + b & E \leq E_C \\ 0 & E > E_C \end{cases} \tag{5.5}$$

where m, b, and E_C are free parameters. The convolution of this function with a Gaussian distribution

$$g(E) = \frac{1}{\sigma\sqrt{2\pi}} e^{-\frac{1}{2}\left(\frac{E}{\sigma}\right)^2} \tag{5.6}$$

gives

$$(f * g)(E) = \frac{1}{2}(mE + b)\left(1 + \operatorname{erf}\left[\frac{E_C - E}{\sqrt{2}\sigma}\right]\right) - \frac{m}{\sqrt{2\pi}} e^{-\frac{1}{2}\left(\frac{E_C - E}{\sigma}\right)^2} \tag{5.7}$$

Where $\operatorname{erf}(x) = \frac{2}{\sqrt{\pi}} \int_0^x e^{-t^2} dt$. The free parameters of the fit are m, b, E_C, σ, and a constant added to equation 5.7 to allow for background. This function was found to be sufficient for determining the Compton edge without resulting in pathological fits. Figure 5.2 shows an example of such a fit.

The neutron detectors were calibrated so that a fusion neutron pulse would be approximately in the center of the dynamic range. A 2.45 MeV neutron has an

electron equivalent recoil energy of about 900 keV. That is, the ionization energy from a proton recoiling from a 2.45 MeV neutron is approximately equal to the ionization energy of an electron recoiling from a 900 keV gamma ray. Therefore, the detectors were calibrated to have a dynamic range of about 2 MeV. This corresponds to a gain of about 5 ADC counts per keV (table 5.1). Energy calibration measurements were made at the beginning of run 6 when the voltages were set. The calibration was re-measured twice during the run and again at the end of the run to ensure that the calibrations did not drift. No measurable change was found.

Statistical and systematic uncertainties in the energy calibration of the neutron detectors will have essentially no impact on the results reported in this document. Neutron energy is not used in these analyses, except for a high energy veto on fusion neutrons, but the position of this veto is determined empirically. Thus, the errors stated here in the calibration measurements are simply the statistical errors in the functional fit.

5.2 Time Alignment

Muon capture on nuclei produces a prompt x-rays. Thus, the raw neutron detector time distribution has a large, prompt x-ray peak due to muon capture on high-Z materials. These x-rays can be vetoed with a combination of pulse shape discrimination and muon stop association. However, the promptness of these x-rays provides a powerful tool for time alignment of the detectors.

Using 1 ns bins, this peak was fit with a Gaussian for each detector, and the center of each fit was shifted to t=0. Figure 5.3 shows these fits for the eight detectors, and table 5.2 lists the timing offsets determined from this method.

5.3 After-pulse Veto

The neutron detectors were found to be susceptible to after-pulsing, especially from high energy pulses. Such high energy pulses are primarily caused by Michel electrons from muon decay traversing the neutron scintillators. These after-pulses create a significant background, especially at low energy. To remove them, a veto is applied on all neutron detector pulses with a preceding pulse in the same detector within a single muon entrance window (up to 25 μs between pulses). Figure 5.4 shows the pulse-shape discrimination (PSD) plot (described in the next section) for one channel before and after an after-pulse veto was applied. The reduction in after-pulses can be seen in the low energy, high tail/total ratio region in the top left corner of the plots. Unless otherwise specified, all neutron data presented in this work have both an after-pulse cut and an overloaded pulse cut applied.

5.4 Pulse Shape Discrimination

The large number of muon decays occurring in the experiment create a significant gamma ray background (eq. 1.1). As discussed above, these gamma rays are seen by

Detector	Cs-137 Edge (ADC)	Co-60 Edge (ADC)	Difference (ADC)	Gain (ADC/keV)	Offset (keV)
NU3	2273 ± 114	5440 ± 122	3167 ± 167	5.66 ± 0.30	78 ± 30
ND3	2422 ± 73	5667 ± 77	3245 ± 106	5.79 ± 0.19	60 ± 18
NU6	2155 ± 112	5096 ± 263	2941 ± 286	5.25 ± 0.51	68 ± 54
ND6	1557 ± 53	3481 ± 117	1924 ± 128	3.44 ± 0.23	27 ± 37
NU11	2177 ± 83	4772 ± 90	2595 ± 122	4.63 ± 0.22	8.6 ± 26
ND11	2641 ± 115	5706 ± 277	3065 ± 300	5.47 ± 0.54	-4.0 ± 55
NU14	2000 ± 39	4714 ± 31	2714 ± 50	4.85 ± 0.09	67 ± 10
ND14	2215 ± 64	5144 ± 88	2929 ± 109	5.23 ± 0.19	56 ± 21

Table 5.1: Neutron detector calibrations. Errors quoted are the propagated statistical errors in the functional fit.

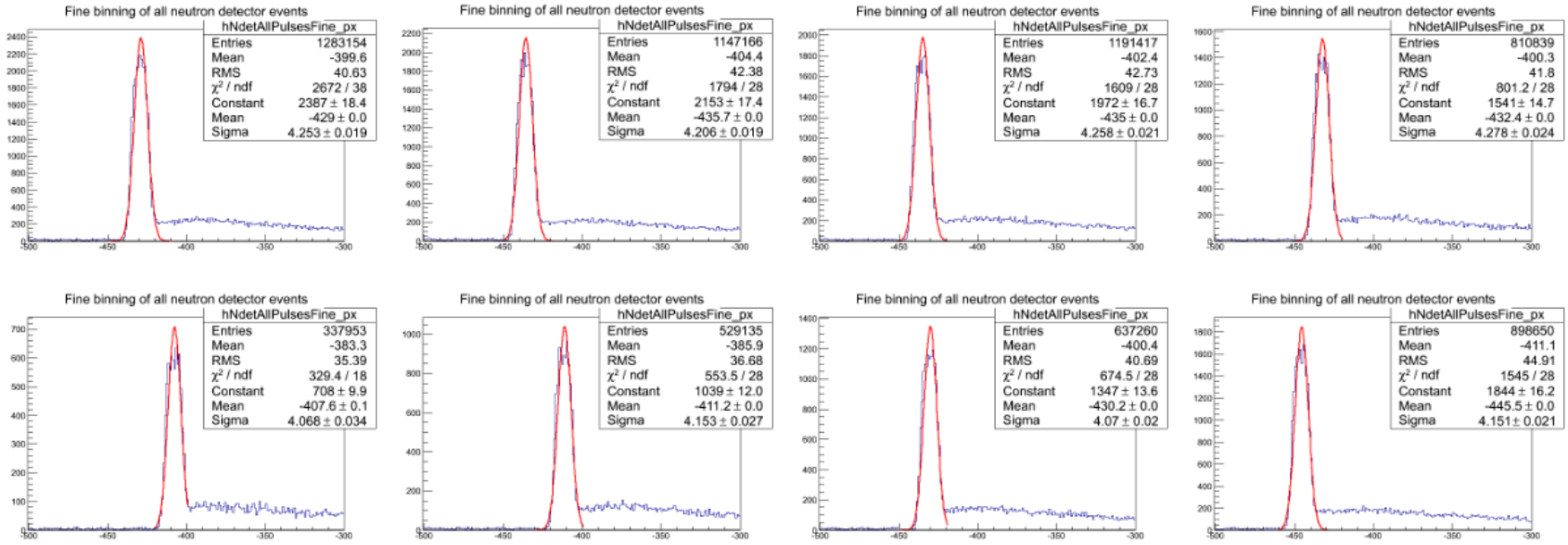

Figure 5.3: Raw neutron detector pulse time relative to muon entrance time ($t_n - t_\mu$). The prompt x-ray peak is fit with a Gaussian distribution, and a time offset is applied to shift the centers of the Gaussian fits to t=0 (table 5.2). Top row, left to right: NU3, ND3, NU6, ND6. Bottom row, left to right: NU11, ND11, NU14, ND14.

Detector	Correction (ns)	σ of fit
NU3	429	4.3
ND3	436	4.2
NU6	435	4.3
ND6	432	4.3
NU11	408	4.1
ND11	411	4.2
NU14	430	4.1
ND14	446	4.2

Table 5.2: Time offsets applied to neutron detector peak times (relative to muon entrance time) for time alignment of detectors.

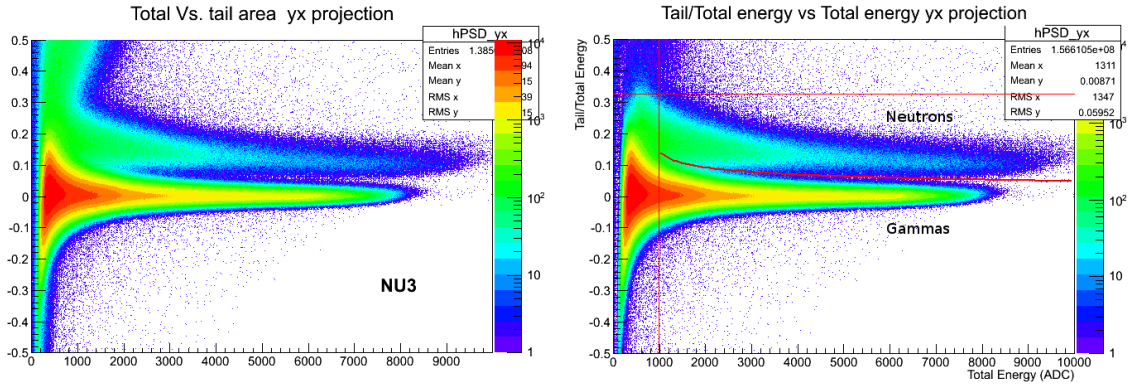

(a) (b)

Figure 5.4: Pulse-shape discrimination (PSD) plots for detector NU3 before and after an after-pulse veto was applied. After-pulses are predominantly low energy pulses with a very high tail/total energy ratio. Note the reduction in such pulses after applying the veto.

the neutron detectors. Indeed, gamma ray pulses outnumber neutron pulses by more than an order of magnitude. Therefore, it is important to efficiently discriminate neutrons from gamma rays in the neutron detectors.

In organic scintillators, an incident neutron elastically scatters off of a hydrogen nucleus (proton). The recoiling proton produces ionization resulting in the production of scintillation photons. A gamma ray in a scintillating medium instead ionizes an electron, which also produces ionization and thus scintillation. The time evolution of scintillation photons due to an ionizing particle has a fast and a slow exponential component. The scintillation profile of a recoil proton will have an enhanced slow component as compared to an electron due to its much higher ionization density. The resulting difference in pulse shape allows us to discriminate neutrons from gamma rays in the neutron detectors.

Pulse-shape discrimination (PSD) is done using the "slow/total" method. The total integral of the pulse (above pedestal) is compared to the "slow integral" (or "tail

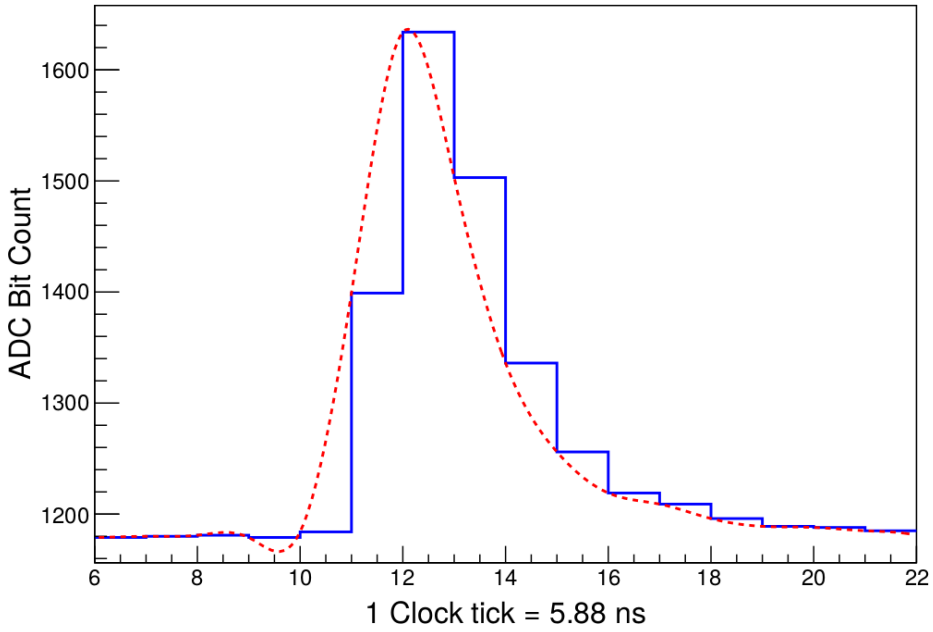

Figure 5.5: A typical neutron pulse. The dotted red curve is a cubic spline fit for interpolating pulse peak and pulse shape. (image reference [1])

integral") which starts approximately five clock ticks (∼30 ns) after the pulse peak (as determined by the cubic spline interpolation, fig 5.5). Both the slow integral and the total integral end at 400 ns after the peak time. Other start times were previously investigated by the MuSun collaboration, and the 30 ns start time was found to give the best PSD. A template fitting method of PSD was also investigated in [1]. While the template fitting method did show an advantage over the slow/total method at low energies, the template method was found to be very computationally intensive, with only nominal improvements in PSD over most of the dynamic range of the detectors. Thus, the slow/total method is used for these analyses. For illustrative purpose, figure 5.6 shows templates for neutron and gamma ray pulses, which were constructed by averaging pulses which were well discriminated by the slow/total method.

Figure 5.7 shows the PSD histograms for all eight detectors using run 6 production data. The curve dividing the neutron branch from the gamma ray branch was defined by finding the minimum between the two branches at several points along the total pulse energy axis, then fitting these points with a four-parameter power law

$$f(E) = A(E - E_0)^{-k} + C \tag{5.8}$$

where E is pulse energy in uncalibrated ADC bit counts, $f(E)$ is the slow integral to total integral ratio (a dimensionless quantity), and A, C, E_0, and k are the free parameters of the fit. The lower bound on total pulse area was set as the lowest point where two distinct peaks in the slow/total ratio could be discriminated.

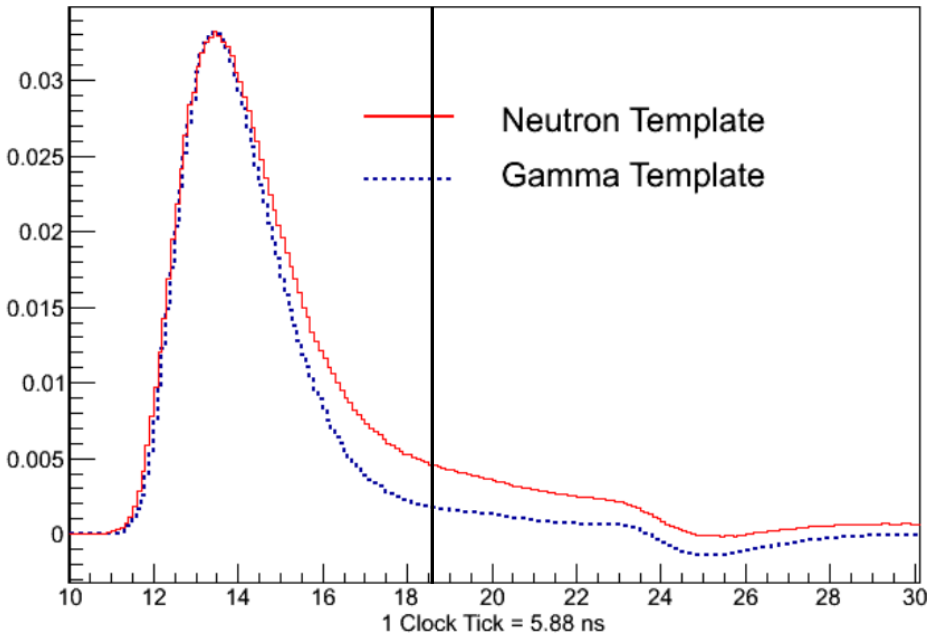

Figure 5.6: Templates neutron and gamma pulses normalized to equal amplitude. These were created by [1] for a study of template based PSD, and are used here for illustrative purpose. Note the sharper peak and lower tail of the gamma ray pulse as compared to the neutron pulse. The horizontal axis is in FADC clock ticks. The vertical line shows the position of the start of the tail integral.

Detector	Curve Parameters				Low E bound (ADC)	Slow/Tot upper bound
	C	A	E_0	k		
NU3	-0.0428(18)	763(14)	0.536(8)	0.194(3)	980	0.326
ND3	-0.0613(21)	935(18)	0.494(8)	0.175(2)	1190	0.3
NU6	-0.0216(17)	766(17)	0.710(13)	0.237(3)	1070	0.358
ND6	-0.0088(14)	593(19)	0.417(7)	0.190(2)	950	0.288
NU11	-0.044(2)	821(29)	0.452(11)	0.204(4)	1170	0.22
ND11	-0.0132(19)	1013(33)	0.425(10)	0.194(3)	1480	0.274
NU14	0.0159(13)	699(12)	0.415(7)	0.207(3)	900	0.35
ND14	0.0024(24)	749(50)	0.713(20)	0.249(4)	1520	0.324

Table 5.3: PSD fit parameters. The curve parameters satisfy equation 5.8, which defines the curve separating the neutron arm from the gamma arm of the histograms in figure 5.7. "Low E bound" is the lower energy bound (vertical line in figure 5.7) in ADC counts. "Slow/Tot upper bound" is the upper bound on the slow energy to total energy ratio (horizontal straight line in figure 5.7).

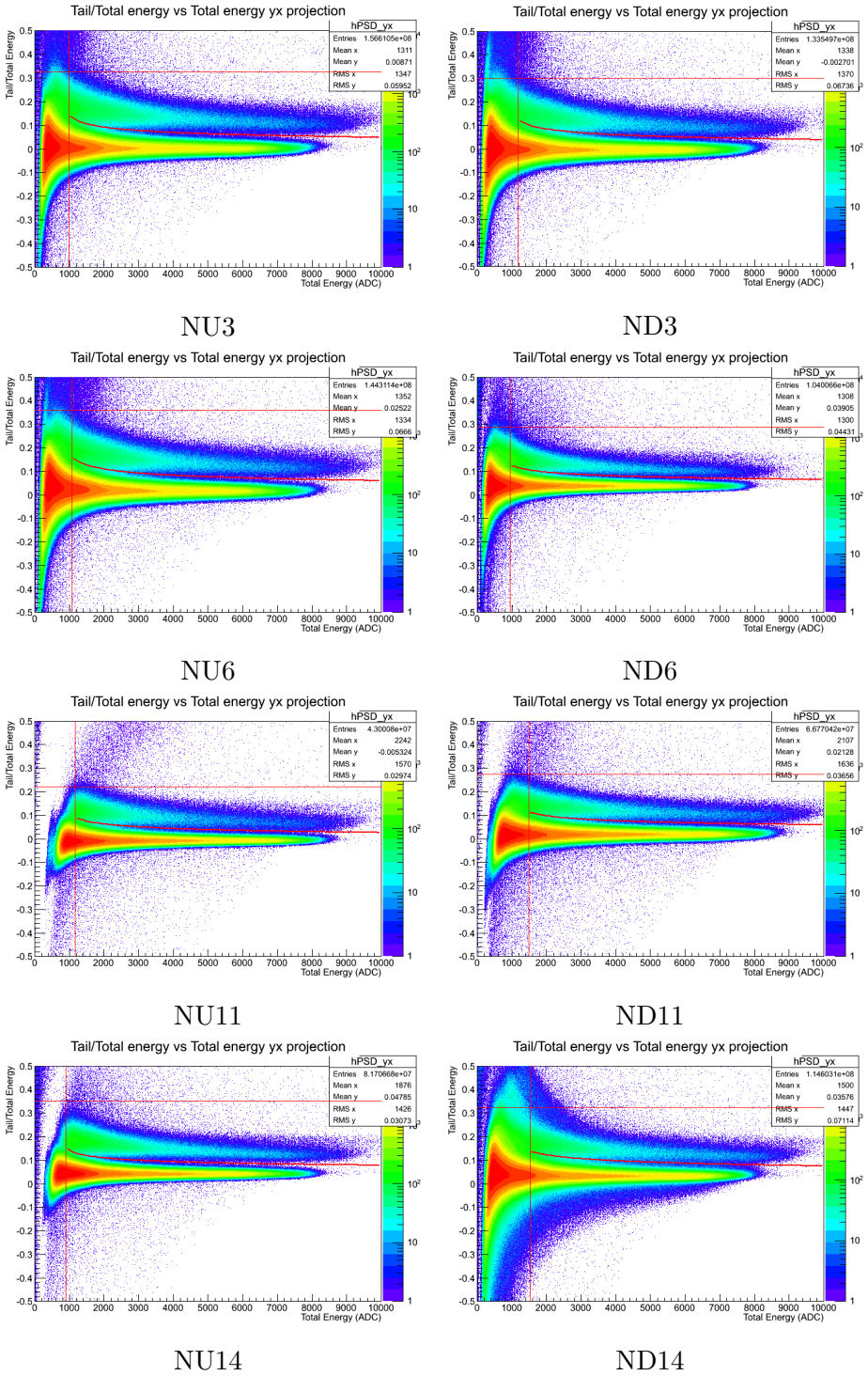

Figure 5.7: Pulse shape discrimination for neutron detectors. This plot shows tail/total energy vs total energy for approximately 1.6×10^8 pulses each. The horizontal axis is total pulse area in ADC bit counts. The vertical axis is the ratio of the slow integral to the total integral. Events in the region bounded by the three lines are defined as neutrons. The large band below the neutron band are gamma ray pulses.

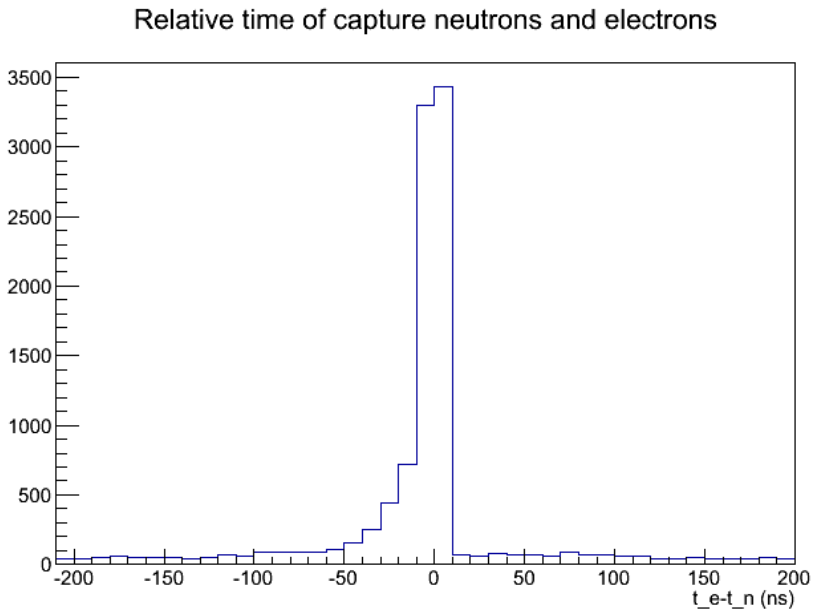

Figure 5.8: Plot of $t_e - t_n$, time of electron relative to neutron, for non-fusion, non-capture neutrons (see chapter 6 for description of how fusion neutrons and capture neutrons are defined).

5.5 Electron Coincidence Veto

Electrons from muon decay may emit a gamma ray (through radiative decay or bremsstrahlung) which may undergo a photo-nuclear reaction with a nucleus in the liquid scintillating material of the neutron detectors. This processes will produce protons or neutrons which are seen by the neutron detectors but do not originate in the D_2 target. These events can be isolated by applying multiple cuts to the neutron data which eliminate nearly all neutrons originating from the target. These cuts are discussed in detail in chapter 6. In brief, we require that an electron be associated with the neutron pulse, but have no associated ^{3}He recoil in the TPC. Since only fusion neutrons should have associated electrons, the combination of these requirements will veto both fusion neutrons and capture neutrons. The photo-nuclear neutrons can then be identified by an associated prompt electron in the gondolas. Figure 5.8 shows the electron time relative to the neutron time for these non-fusion, non-capture neutrons. As can be seen, there is a sharp peak at $t_e - t_n = 0$. For this reason, neutrons with -50 ns $< t_e - t_n < 10$ ns are vetoed.

5.6 Pile-up Veto

A neutron pile-up veto was applied after all other cuts and definitions described above were applied. Neutrons from fusion or capture will be discriminated based on their correlation with a muon stop (see chapter 6). Having two neutrons correlated with a single muon stop would create ambiguity as to its source. This veto reduced the

total neutron statistics by less than 1%.

Chapter 6 D_2 Capture and Fusion Neutron Discrimination

Neutrons are produced by muons in deuterium via two reactions, muon capture (eq. 1.3) and muon catalyzed fusion (eq. 1.7a). As discussed in chapter 2, the muon capture rate and the rate of molecular $dd\mu$ formation (which leads to muon catalyzed fusion) are both strongly dependent on the hyperfine spin state of the initial μd atom. Thus, observation of the time evolution of fusion neutrons and capture neutrons can constrain many of the kinetics parameters related to the μd hyperfine states.

Specifically, the time evolution of fusion neutrons can constrain the hyperfine transition rate from the quartet to the doublet state, λ_{qd}, and the ratio of the molecular formation rates from the two spin states, λ_q/λ_d. Such an investigation was conducted by Raha (ref. [1]) using data from MuSun run 4, and is repeated in part here using run 6 data. Furthermore, a precise observation of the time evolution of capture neutrons can constrain the relative rate of muon capture from the quartet and doublet states, Λ_d/Λ_q, which is the primary result of this work. A precise determination of Λ_d/Λ_q combined with the forthcoming measurement of Λ_d will also allow for a determination of Λ_q. This will be the first experimental limit set on Λ_q.

In order to study the time evolution of fusion neutrons and capture neutrons, they must be clearly discriminated. Fusion neutrons are primarily identified by the detection of a ^{3}He recoil in the TPC. They may also be identified by an associated delayed Michel electron from the decay of the muon. Furthermore, as muon catalyzed fusion has only two products, the neutron and a ^{3}He nucleus, fusion neutrons are mono-energetic with an energy of 2.45 MeV.

Neutrons from deuterium capture are more difficult to identify, as the only products of this reaction are the two neutrons and a neutrino which is undetected. This means that there is no signature that can be used to define a capture neutron. To further complicate matters, since muon capture has three products, capture neutrons fall on a spectrum of energies which is peaked at a about 1 MeV (near the fusion neutron energy) and continues up to the kinematic limit of about 53 MeV (half the muon mass) (fig. 6.1). Thus, capture neutrons are selected by vetoes on helium recoils and delayed electrons. Neutrons may also be produced by muon capture on high-Z materials in the detector assembly, but these neutrons can be vetoed very efficiently by ensuring the muon stop occurs in the deuterium gas.

6.1 Identifying fusion neutrons by ^{3}He recoil

As discussed in section 4.5, muons stopped in the deuterium gas deposit an approximately constant amount of energy in the gas, corresponding to an S-energy of 1900 ± 100 keV. If the stopped muon catalyzes a fusion, the recoil of the helium nucleus is also seen in the TPC as a $\sim$350 keV pulse. However, early fusion pulses (< 1 μs after the initial pulse) pile-up with the stop pulse and cannot be distinguished. Thanks to the cryogenic pre-amps installed during run 5 (see section 3.3.2), the energy resolution of the TPC is good enough (17 keV) that stops with an early

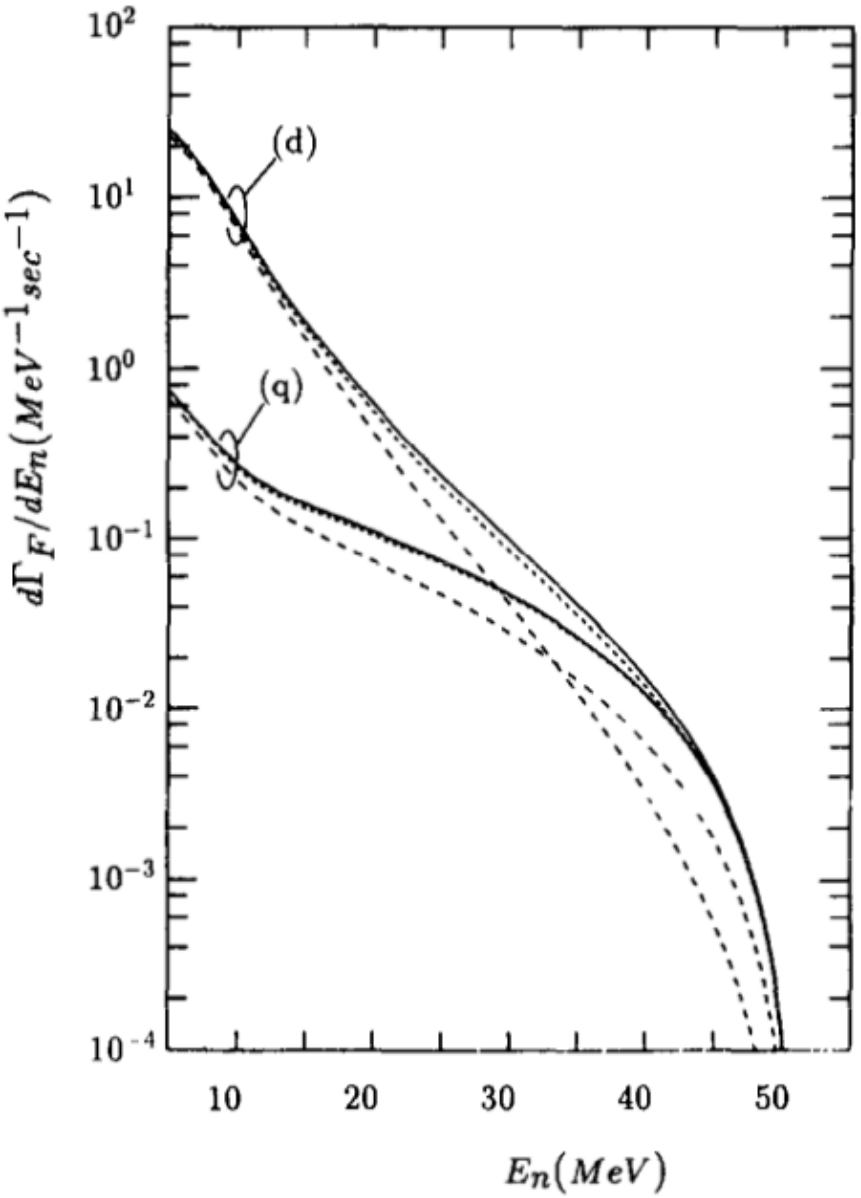

Figure 6.1: Energy spectra for neutrons from muon capture on deuterium from the quartet and doublet hyperfine spin states. (image ref. Doi 1990 [7])

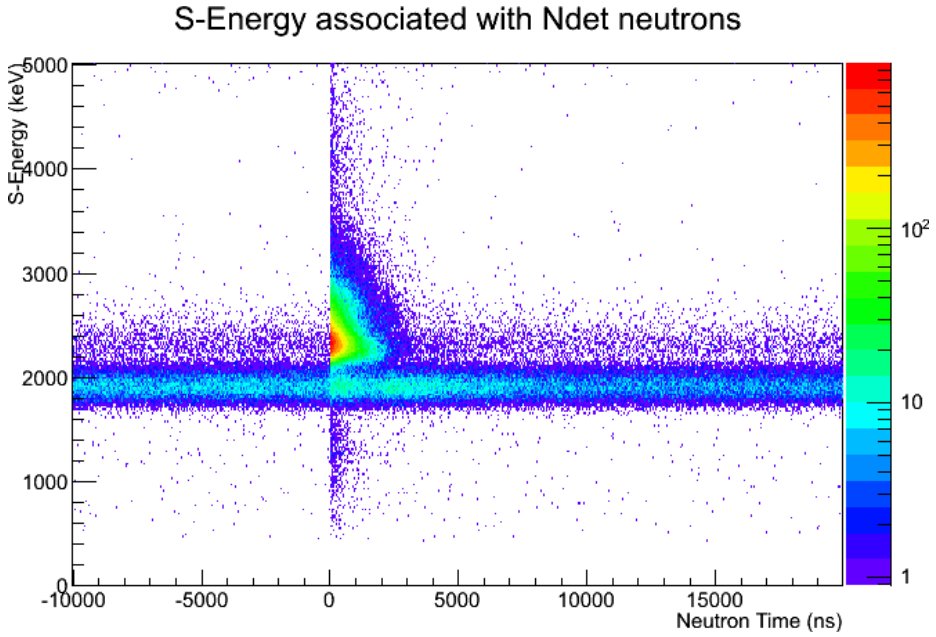

Figure 6.2: S-energy of muon stops vs. neutron time relative to muon entrance time. The prominent band centered at $\sim$ 1900 keV corresponds to muon stops without a delayed pulse, such as from ^{3}He recoils. The feature centered around 2200 keV in the range of 0 ns–2000 ns are stops with a ^{3}He recoil early enough to be included in the S-energy definition. Stops with a ^{3}He recoil after this time end up in the primary band creating an excess in that band.

fusion pulse can be clearly discriminated from stops without an early fusion by the increase in S-energy. However, helium-3 recoils which occur more than two microseconds after the muon stop are not included in the S-energy calculation. As a result, fusion neutrons cannot be identified solely based on the increase in S-energy. Stops with a fusion are therefore identified by either having an increased S-energy or a delayed ^{3}He pulse. Figure 6.2 shows the S-energy of muon stops as a function of neutron time relative to the muon entrance. Stops with an early ^{3}He recoil can be seen in a region above the prominent S-energy band, centered at approximately 2200 keV. Most stops with a ^{3}He recoil after about 2 μs end up in the main S-energy band. Figure 6.3 shows the same data as figure 6.2 but for either (a) stops with multiple pulses on the stop pad or (b) only a single pulse on the stop pad. The excess in the main S-energy band from fusion neutrons with late ^{3}He recoil pulses is clearly identified and separated from stops without a ^{3}He recoil. Figure 6.4 shows the pulse energy vs time after muon entrance for (a) delayed pulses on the stop pad and (b) delayed pulses on a pad neighboring the stop pad. The possibility of ^{3}He recoil pulses occurring on pads adjacent to the stop pad was investigated. While some evidence of recoil pulses occurring on adjacent pads can be seen, the signal is very small relative to the background of coincident pulses, so only delayed pulses on the stop pad are used to define fusion and capture neutrons.

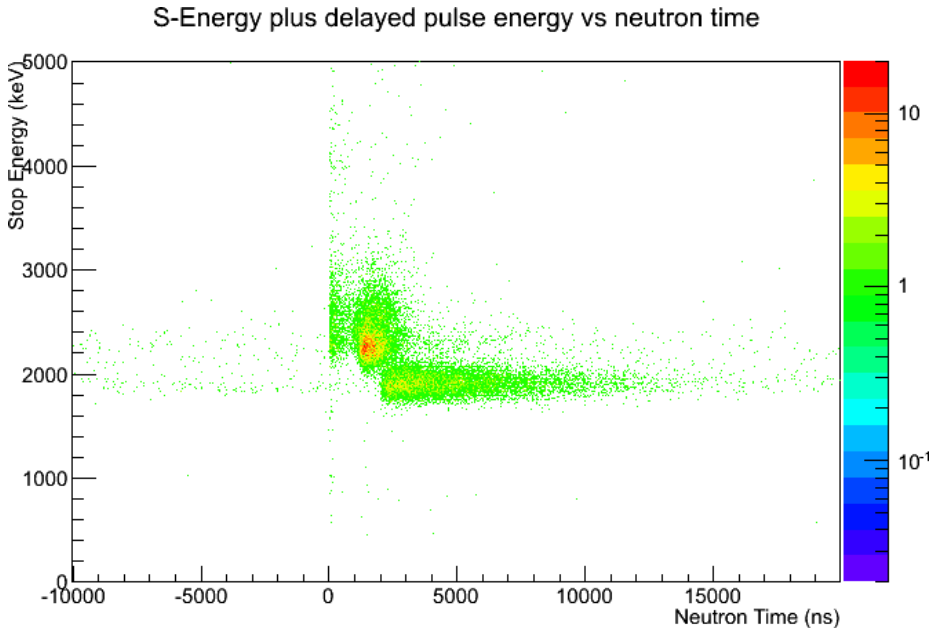

(a)

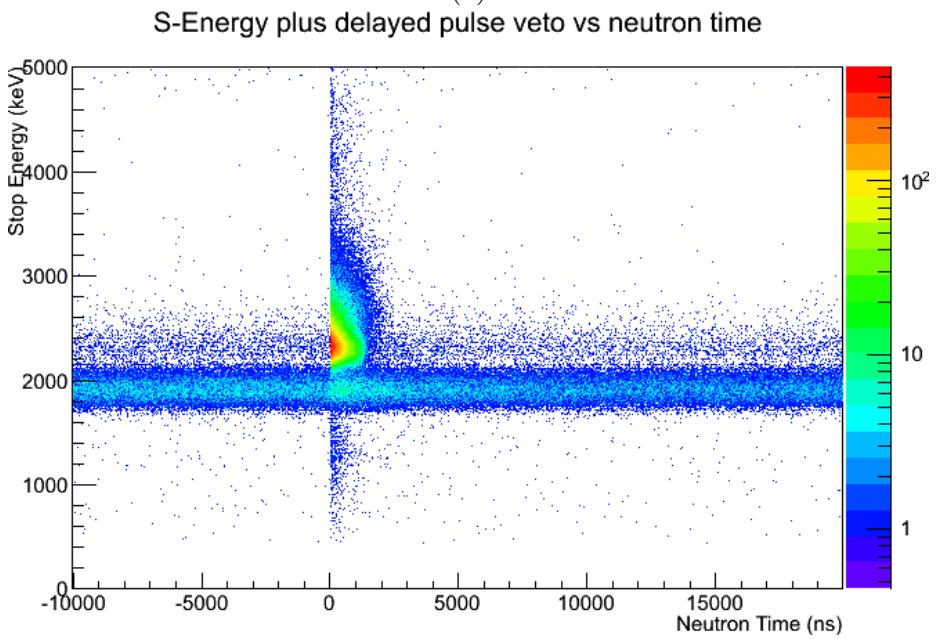

(b)

Figure 6.3: S-energy of muon stops vs. neutron time relative to muon entrance time for (a) stops with multiple pulses on the stop pad and (b) stops without multiple pulses on the stop pad.

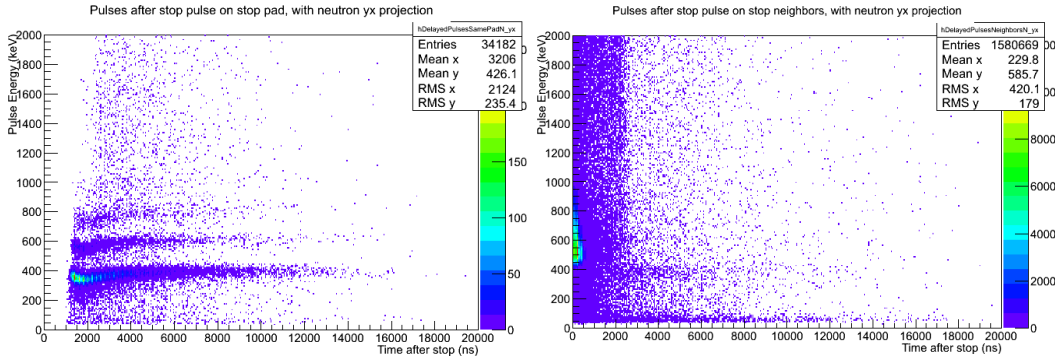

(a) (b)

Figure 6.4: (a) Pulse energies vs time after stop for delayed pulses on the muon stop pad. The prominent band around 350 keV is from ^{3}He recoil. The second band at approximately 550 keV is from $\mu + {}^3$He recoils. (b) Energy vs time plot of delayed pulses on pads which neighbor the stop pad. The vast majority of ^{3}He recoils occur on the stop pad. Helium recoils on pads neighboring the stop pad are rare and difficult to discriminate from noise, so only delayed pulses on the stop pad are considered.

6.2 Fusion and capture neutron definitions

Using the muon stop and electron information described in the previous section, we can construct definitions for fusion and capture neutrons. Neutrons from both sources must satisfy the following conditions:

- a best quality neutron pulse according to the criteria in chapter 5.
- an associated best muon entrance, as described in section 4.4.
- an associated muon stop in the fiducial volume of the TPC as described in section 4.5.
- a veto on events with multiple tracks for a single muon entrance.

In addition, a fusion neutron must have

- an associated electron in the eSC.
- either of the two following conditions:
  - an S-energy of the muon stop between 2100-4000 keV, or
  - multiple pulses on the stop pad of the muon track and an S-energy of the muon stop between 1700-4000 keV.

and a capture neutron must have

- no associated electron in the eSC.
- exactly one pulse on stop pad of the muon track.

- an S-energy of the muon stop between 1700-2050 keV.

Furthermore, we may define background neutrons by requiring

- an associated electron in the eSC.
- no associated delayed pulse on the stop muon stop pad in the TPC.
- a modified S-energy of the muon stop between 1700-2050 keV.

Since fusion neutrons have both a helium recoil in the TPC and a delayed electron, while capture neutrons have neither of these signatures, this last definition excludes both fusion and capture neutrons, and so should only be comprised of neutrons not arising from a muon stop in the deuterium gas. These conditions define the background for both fusion and capture neutrons.

For these definitions, an associated electron is defined as any electron in the event window of the muon entrance with an acceptance window of $-20\ \mu\text{s} < t_e - t_\mu < 20\ \mu\text{s}$. Although the electron associated with a fusion is delayed relative to the muon stop, both early and late electrons are included in these cuts for a few reasons. First, cutting on only delayed electrons can introduce an artificial time dependence in the neutron time distributions, whereas cutting on both early and late electrons avoids this complication. Second, the primary focus of this work is to study the time evolution of neutrons from deuterium capture. As there is no physical process internal to the experiment which produces electrons preceding the muon stop, such events are background and should be vetoed anyway. Third, The rate of early electrons was found to be very low as compared to delayed electrons, so including events with early electrons in the fusion neutron definition has a minimal impact on the results, but it allows for a single, consistent electron definition to be used for both neutron definitions. This is particularly useful in defining background events.

Figures 6.5, 6.6, and 6.7 show the time distributions for fusion neutrons, capture neutrons and background neutrons respectively. The fusion and capture neutron time distributions are shown before background subtraction. This means that there is still a significant background component in the capture neutron spectrum. The two component nature of the fusion neutron time distribution can be clearly seen. Background subtraction and fits to the data will be discussed in the next chapter.

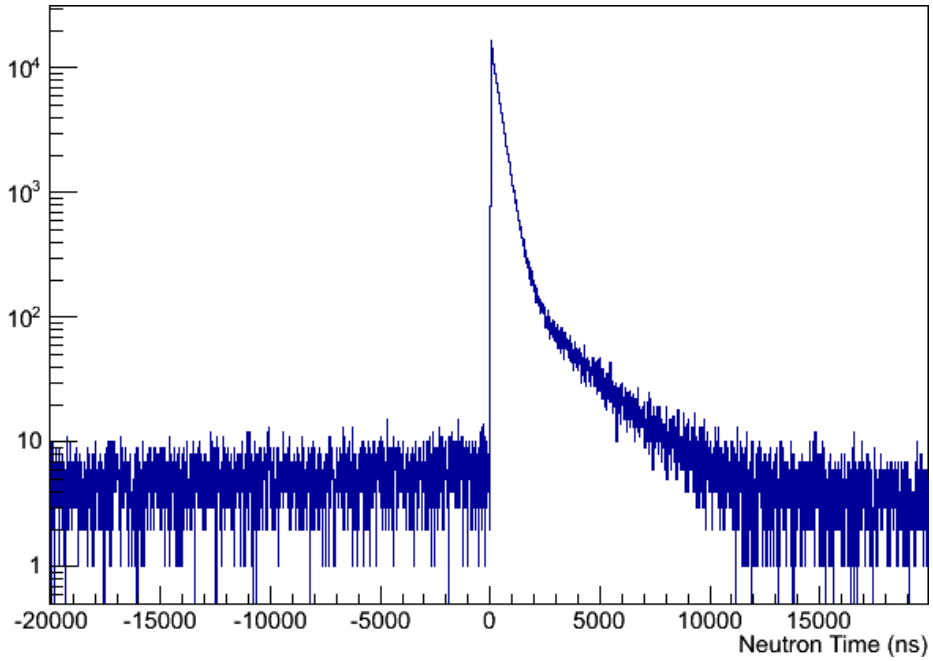

Figure 6.5: Time distribution of fusion neutrons before background subtraction. The fast and slow components, due to $dd\mu$ molecular formation from the quartet and doublet spin states respectively, can be clearly seen.

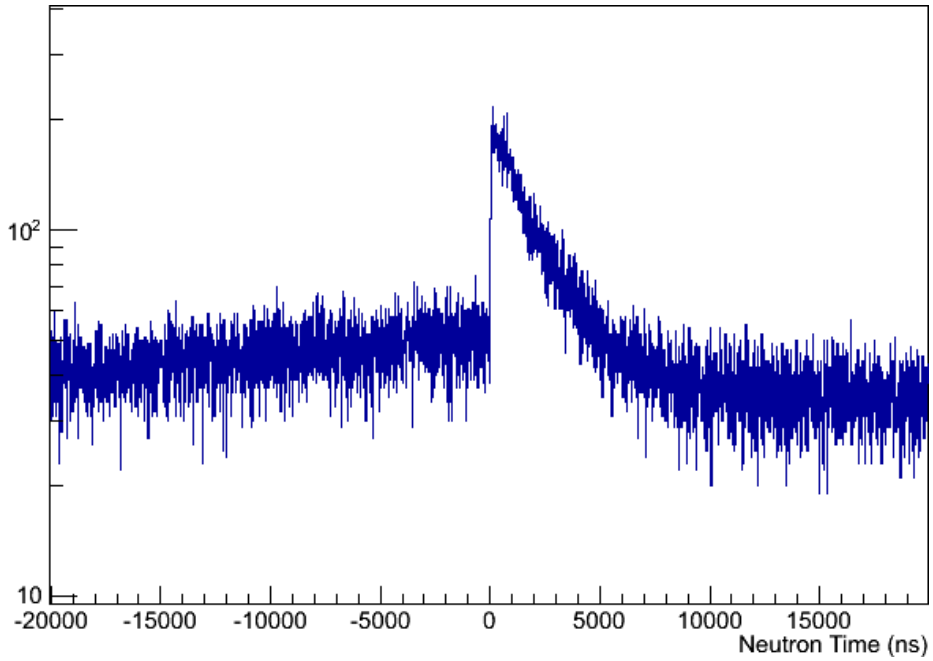

Figure 6.6: Time distribution of capture neutrons. These data are shown before background subtraction, so there is a significant background component (see fig. 6.7) which can be seen in the sloping feature before time zero. These data also include a contribution from photo-nuclear reaction neutrons which will be discussed in chapter 7.

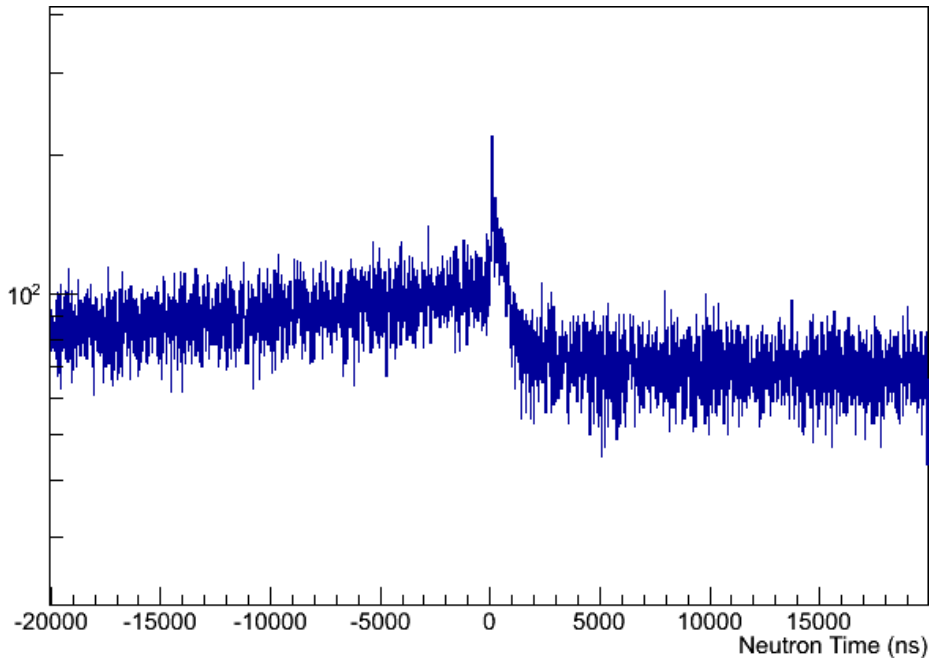

Figure 6.7: Time distribution of the capture neutron background. These data are also used as the background for fusion neutrons. An early, beam-dependent component is clearly visible. There is also a small, short-lived feature which could not be isolated.

Chapter 7 Results

As was shown in section 2.3, the time distributions of both fusion and capture neutrons are represented by the sum of two exponentials.

$$R = A_1 e^{-\lambda_1 t} + A_2 e^{-\lambda_2 t} \tag{7.1}$$

where the quantities A_1, A_2, λ_1, and λ_2 are the free parameters for fitting the data. The ratios of the $dd\mu$ molecular formation rates from the two hyperfine spin states, λ_q/λ_d, as well as the ratio of the μd capture rates from the two spin states, Λ_q/Λ_d, may be determined from these parameters. Recall that, from equation 2.11b

$$\begin{aligned} A_1 &= \frac{2}{3} N_0 \Lambda_d \left(\frac{1}{2} + X \right) \\ A_2 &= \frac{2}{3} N_0 \left(\Lambda_q - \Lambda_d X \right). \end{aligned} \tag{7.2}$$

From these we may derive the equation

$$\frac{\lambda_q}{\lambda_d} = X + \left(\frac{1}{2} + X \right) \frac{A_{2,f}}{A_{1,f}} \tag{7.3a}$$

$$\frac{\Lambda_q}{\Lambda_d} = X + \left(\frac{1}{2} + X \right) \frac{A_{2,c}}{A_{1,c}} \tag{7.3b}$$

where $A_{1,f}$ and $A_{2,f}$ are the coefficients obtained from the fusion data, and $A_{1,c}$ and $A_{2,c}$ are obtained from the capture data. For simplicity, the "f" and "c" subscripts will be dropped when it is clear from context which data set these coefficients coincide with. Note that the equation for λ_q/λ_d will be the same. By equations 2.8 and 2.9, the quantity X may be written as

$$X = \frac{\lambda_2 - \lambda_\mu - \phi\omega\lambda_q}{\lambda_2 - \lambda_1}. \tag{7.4}$$

Thus, the quantities not directly derived from the data which enter into the determination of Λ_q/Λ_d (and likewise λ_q/λ_d) are the free muon lifetime, λ_μ, the normalized gas density, ϕ, the effective sticking fraction, ω, and the $dd\mu$ molecular formation rate from the quartet hyperfine state, λ_q. The density fraction for deuterium at T=31 K and P=5.1 bar is 6.50×10^{-2}. This quantity is determined using data from the NIST chemistry web-book [45], and is stated relative to a reference density of LH_2 of 4.25×10^{22} atoms/cm^3 [4, 8]. The muon lifetime was determined to high accuracy by MuLan, and λ_q was determined experimentally by Balin *et al.* (2011) [8] to be 3.98(5) μs^{-1} at 28.3 K and 4.13(7) μs^{-1} at 32.2 K. Interpolating between these two values gives $\lambda_q = 4.08(7)$ μs^{-1}.

While λ_μ was recently determined to very high accuracy by the MuLan experiment, the data presented here are currently blinded, so any rates used in these

analyses which do not come from the run 6 production data will necessarily introduce a systematic uncertainty. This uncertainty may be mitigated by recalling that $\lambda_1 = \lambda_\mu + \phi\left(1 - \frac{1}{3}(1-\omega)\right)\lambda_d$ and noting that the λ_d term is over two orders of magnitude smaller than λ_μ, so we may make the approximation $\lambda_\mu \approx \lambda_1$, so that equation 7.4 becomes

$$X = \frac{\lambda_2 - \lambda_1 - \phi\omega\lambda_q}{\lambda_2 - \lambda_1}. \tag{7.5}$$

Thus, λ_q is the only quantity derived from the literature which is affected by the blinding.

Since the quantities λ_1 and λ_2 are identical for both the fusion and capture neutron time distributions, they may be determined by fitting either data set. In our experiment, fusion neutrons are several orders of magnitude more abundant than capture neutrons. This is due to a few reasons. First, the $dd\mu$ molecular formation rates, λ_d and λ_q, are two to four orders of magnitude larger than the deuterium capture rates, Λ_d and Λ_q. Second, fusion neutrons are mono-energetic, while capture neutrons have a broad energy spectrum. Neutron-gamma pulse shape discrimination is more effective at high energies than at low. For our detectors, this results in a lower bound on neutron detection of ~ 200 keVee. Thus, the detection efficiency is higher for fusion neutrons than for capture neutrons. Therefore, λ_1 and λ_2 will be determined by fitting the fusion neutron time distribution, and their values will be used in the fit of the capture neutron time distribution.

7.1 Fusion Neutrons and λ_q/λ_d

Fusion neutrons are defined according to the conditions described in section 6.2. Since $\lambda_q > \lambda_d$ at experimental conditions, the time distribution of fusion neutrons has a fast component (rate λ_2) which is dominated by the quartet-to-doublet hyperfine transition rate λ_{qd}. At later times, after quartet state has depopulated, the time evolution follows a slower exponential (rate λ_1) dominated by the muon lifetime.

7.1.1 Backgrounds

During run 4, a significant beam-dependent background was observed. It was caused by upstream muon captures in high-Z materials such as the beam pipe. It manifests itself in the data as an exponential increase in the early background before time zero. There is also a time-independent background of "room" neutrons produced by the proton accelerator and the beam dump. During run 6, both this time-dependent background and the time-independent background were found to be significantly reduced, although not completely eliminated. This background reduction is likely due to the difference in the beamline geometry in the πE1 beamline (where run 6 took place) as compared to the πE3 beamline (where run 4 took place). Figure 7.1 shows a side-by-side comparison of the fusion neutron time distributions from runs 4 and 6.

Both the time-dependent and time-independent backgrounds are removed by subtracting the background neutron time distribution (defined in the previous chapter, fig. 6.7) from the fusion neutron time distribution (fig. 6.5). The background signal

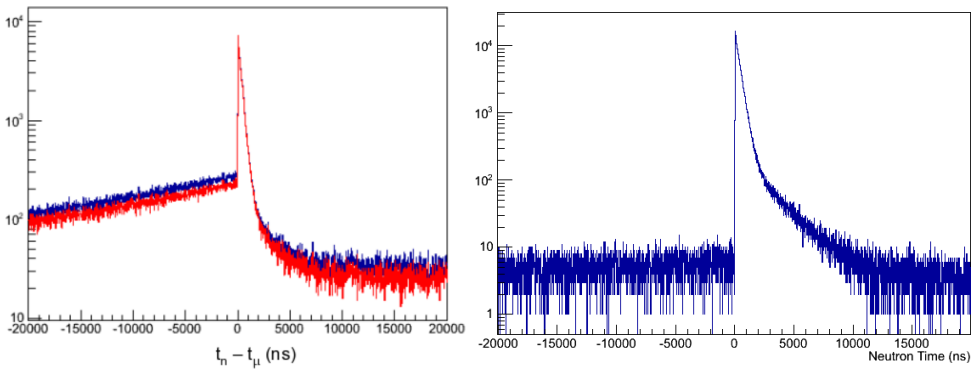

(a) (b)

Figure 7.1: Fusion neutron time distributions before background subtraction from run 4 (a) and run 6 (b). In figure (a) the blue and red lines show the time distribution before and after a cut on high energy neutrons. Both the early beam-dependent background and the flat background are significantly reduced in the run 6 data as compared to run 4. (Figure (a) from Raha [1].)

is normalized to the fusion signal on both an early interval ($t_n - t_\mu$ of -21000 ns to -1000 ns) and a late interval ($t_n - t_\mu$ of 14000 ns to 24000 ns). The subtraction is done separately for each of the eight neutron detectors. The difference between the early and late normalizations, and the effect that this normalization has on the results, is discussed in chapter 8.

Since fusion neutrons are mono-energetic at 2.45 MeV, the energy spectum of fusion neutrons shows a sharp decrease above about 800 keVee, which corresponds to the electron-equivalent recoil energy of these neutrons. However, fusion neutrons, as defined in section 6.2, still occur at energies above this point up to the upper bound of the sensitive range of the detectors. These high energy "fusion" neutrons can therefore be interpreted as background, and they give us a handle on the level of background contamination in the fusion neutrons at lower energies as well. The energy spectra of fusions, (normalized) backgrounds and the difference are shown in figure 7.2. As can be seen, the fusion and background energy spectra are well matched at high energies above the fusion cutoff for all detectors.

7.1.2 Fit Interval

Muon catalyzed fusions which occur very shortly after the muon stop ($t_n - t_\mu \lesssim$ 100 ns) have a complicated time dependence which does not follow the distinctive two-component exponential structure. This is due to epithermal effects in the $dd\mu$ molecule formation [46]. This effect dies off after the first few hundred nanoseconds, so that by choosing an appropriate start time, the fusion neutron time distribution is well modeled by equation 7.1. The choice of the domain of the fit can potentially have an influence on the results of the fit parameters.

A scan was conducted of both the start and end times of the fit. For the start time scan, the end time for the fit was fixed at $t_n - t_\mu = 20,000$ ns and the start

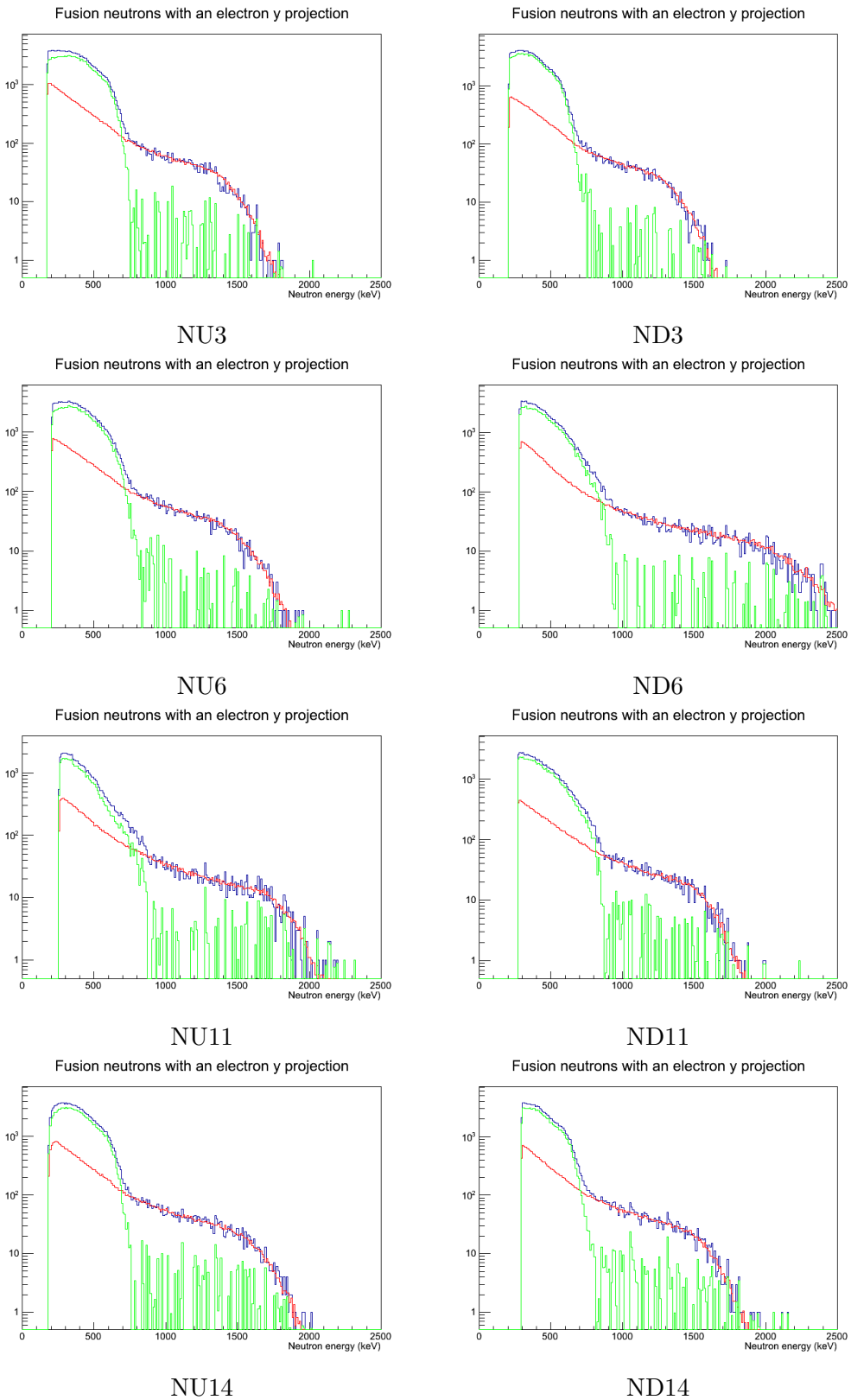

Figure 7.2: Energy spectra of fusion neutrons (blue lines), normalized background neutrons (red lines), and the difference (green lines) for each of the eight neutron detectors.

Parameter	Value
χ^2/NDF	1924/1946
A_1	261.0 ± 5.3
A_2/A_1	68.47 ± 1.24
λ_1 (ns^{-1})	$4.523 \times 10^{-4} \pm 4.3 \times 10^{-6}$
λ_2 (ns^{-1})	$2.810 \times 10^{-3} \pm 1.3 \times 10^{-5}$
X	0.99298 ± 0.00024

Table 7.1: Parameters of the fit (using eq. 7.1) to the fusion neutron time distribution (fig. 7.6). The value of X is derived from the other parameters using eq. 7.5.

time of the fit was varied between 100 ns and 1000 ns in 10 ns steps. Figure 7.3 shows the dependence of each of the four fit parameters on the start time. The red "horn" on these and following histograms shows the statistical error associated with the reduction in the size of the data set due to these cuts. This error is determined by the equation

$$\sigma^2 = \sigma_i^2 - \sigma_0^2 \tag{7.6}$$

where σ_0 is the error in the fit parameter for the full data set and σ_i is the error in the fit parameter for the reduced data set [47].

There is an observable dependence in the values of the three fit parameters on the start time of the fit. Since the early time dependence disappears by $t_n - t_\mu \geq 500$ ns (fig. 7.4), a start time of 500 ns was chosen for the final fit. An end time scan was also conducted. The start time of the fit was held at $t_n - t_\mu = 500$ ns and the end time was varied between 10,000 ns and 20,000 ns in 100 ns steps (fig. 7.5). Except fo a small effect for very early end times, the fit parameters are almost entirely unaffected by the choice of end time. Thus, an end time of 20,000 ns was chosen for the final fit.

7.1.3 Results

Figure 7.6 shows the fit to the data including the fit residual. The fit was done using the Minuit algorithm in ROOT. The method for determining the error bars on the bins is described in appendix A. The fit parameters, including the χ^2 of the fit and the derived value of the parameter X, are given in table 7.1.

From these fit parameters, we may derive the ratio λ_q/λ_d using equation 7.3a, which gives the result $\lambda_q/\lambda_d = 103.2 \pm 1.9$. These parameters may also be used to calculate the quartet-to-doublet hyperfine transition rate, λ_{qd}, by observing that, from equation 2.8,

$$\lambda_2 - \lambda_1 = \phi \left[\lambda_{qd} + \lambda_q \left(1 - \frac{2}{3}(1-\omega) \right) - \lambda_d \left(1 - \frac{1}{3}(1-\omega) \right) \right]. \tag{7.7}$$

As λ_d is about two orders of magnitude smaller than λ_q, it may be approximated to zero. This gives

$$\lambda_{qd} = \frac{1}{\phi} \left[\lambda_2 - \lambda_1 - \phi\lambda_q \left(1 - \frac{2}{3}(1-\omega) \right) \right] \tag{7.8}$$

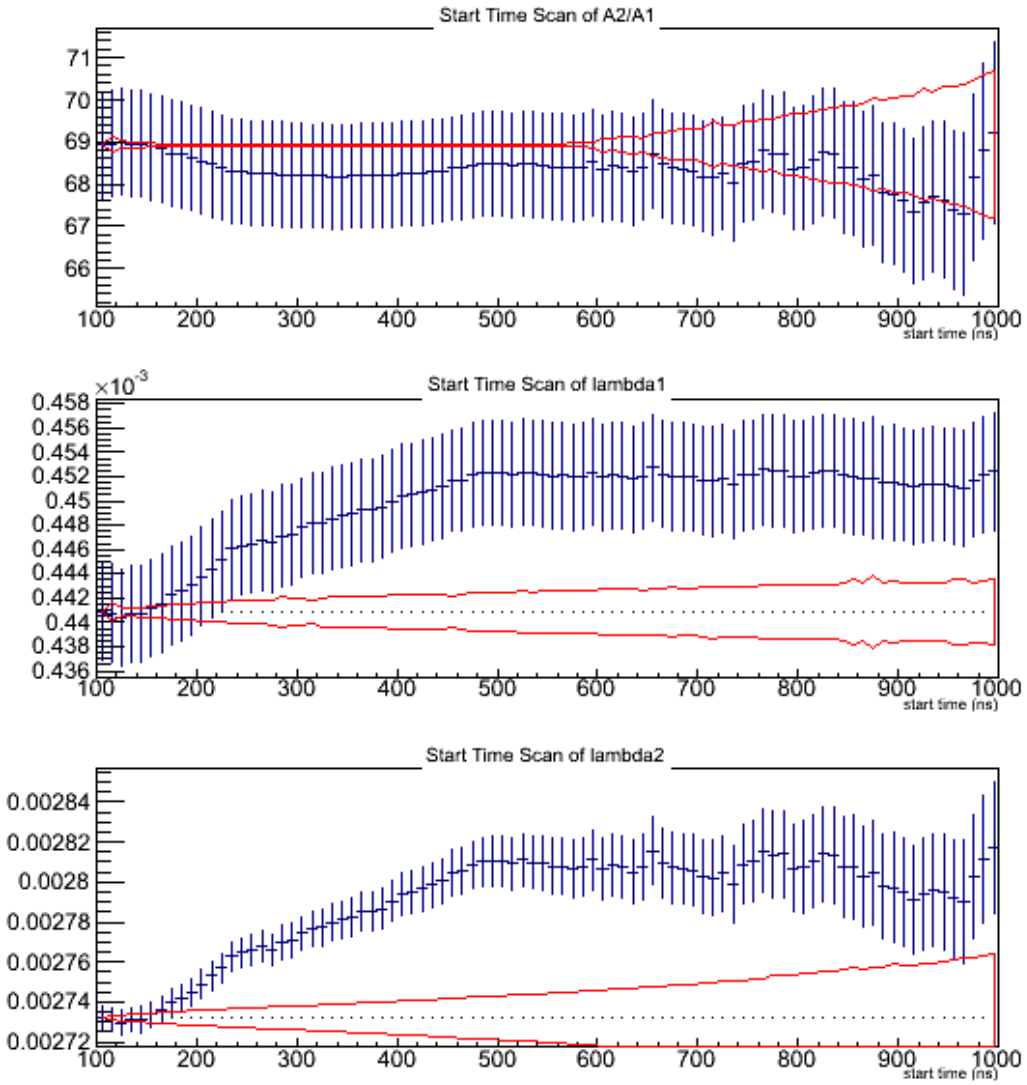

Figure 7.3: Start time scan from 100 ns to 1000 ns for each of the four free parameters in the fusion neutron fit: A_1, A_2, λ_1, and λ_2. The red envelope in each plot shows the statistical uncertainty associated with reducing the sample size by changing the starting point of the fit.

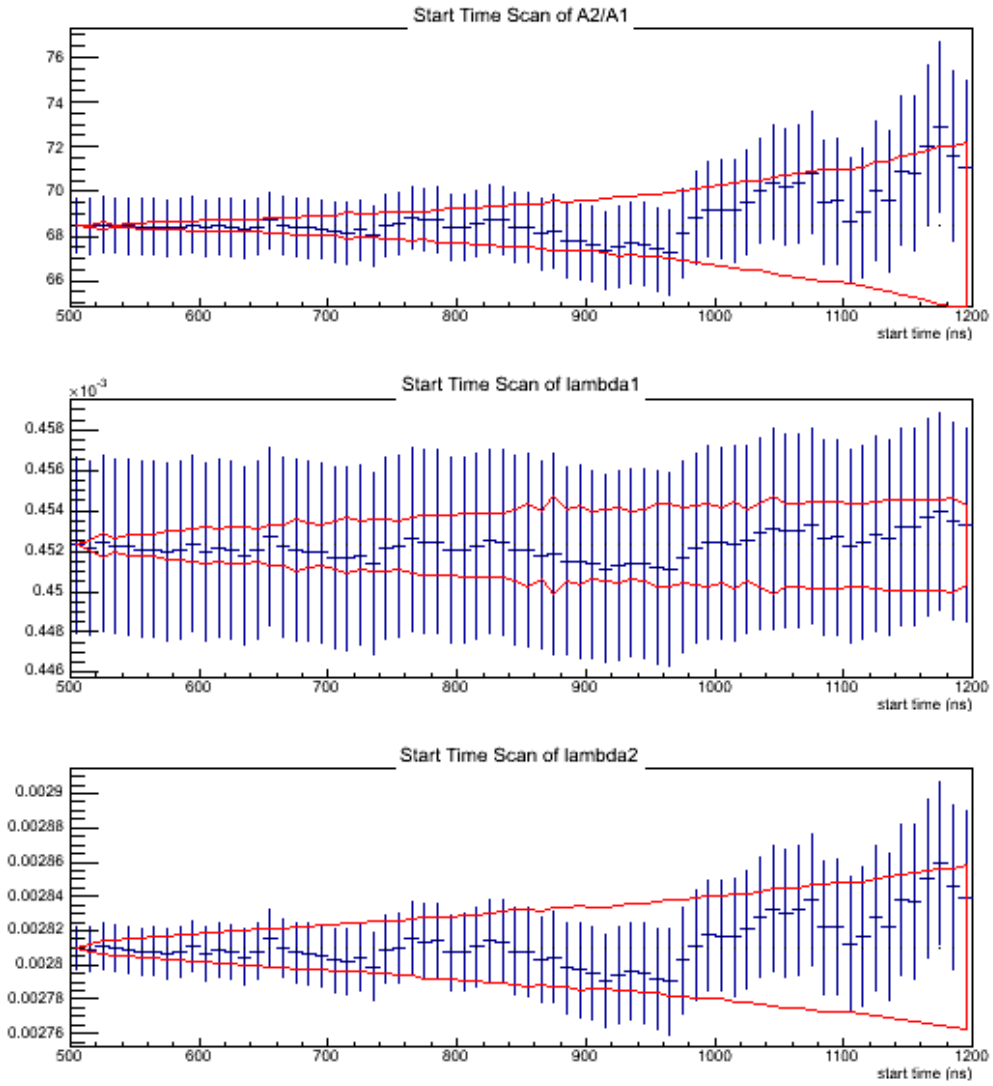

Figure 7.4: Start time scan of fusion fit beginning at 500 ns. The variation of the fit parameters after 500 ns is consistent with statistical error.

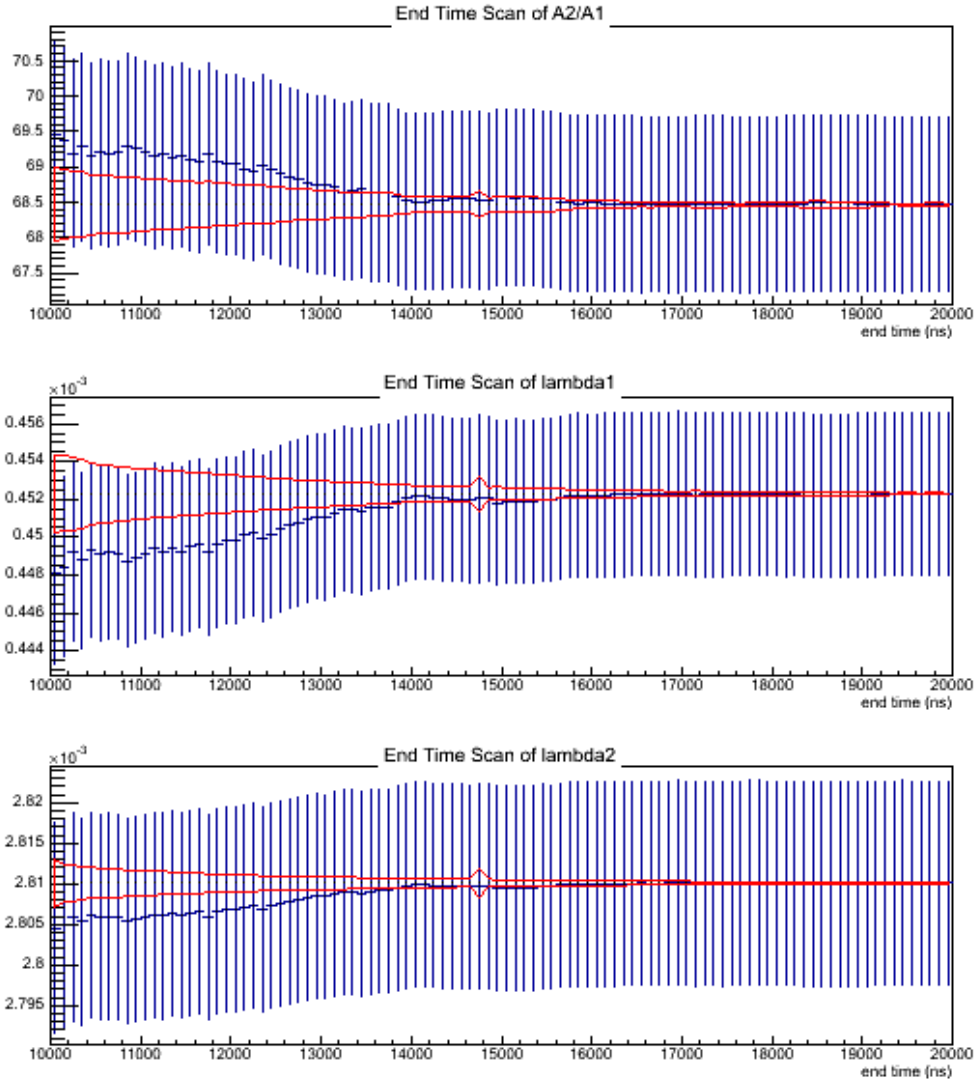

Figure 7.5: End time scan for each of the four free parameters in the fusion neutron fit: A_1, A_2, λ_1, and λ_2. The fit parameters show almost no dependence on the end time of the fit after 15000 ns. An end time of 20,000 ns was chosen for the final fit.

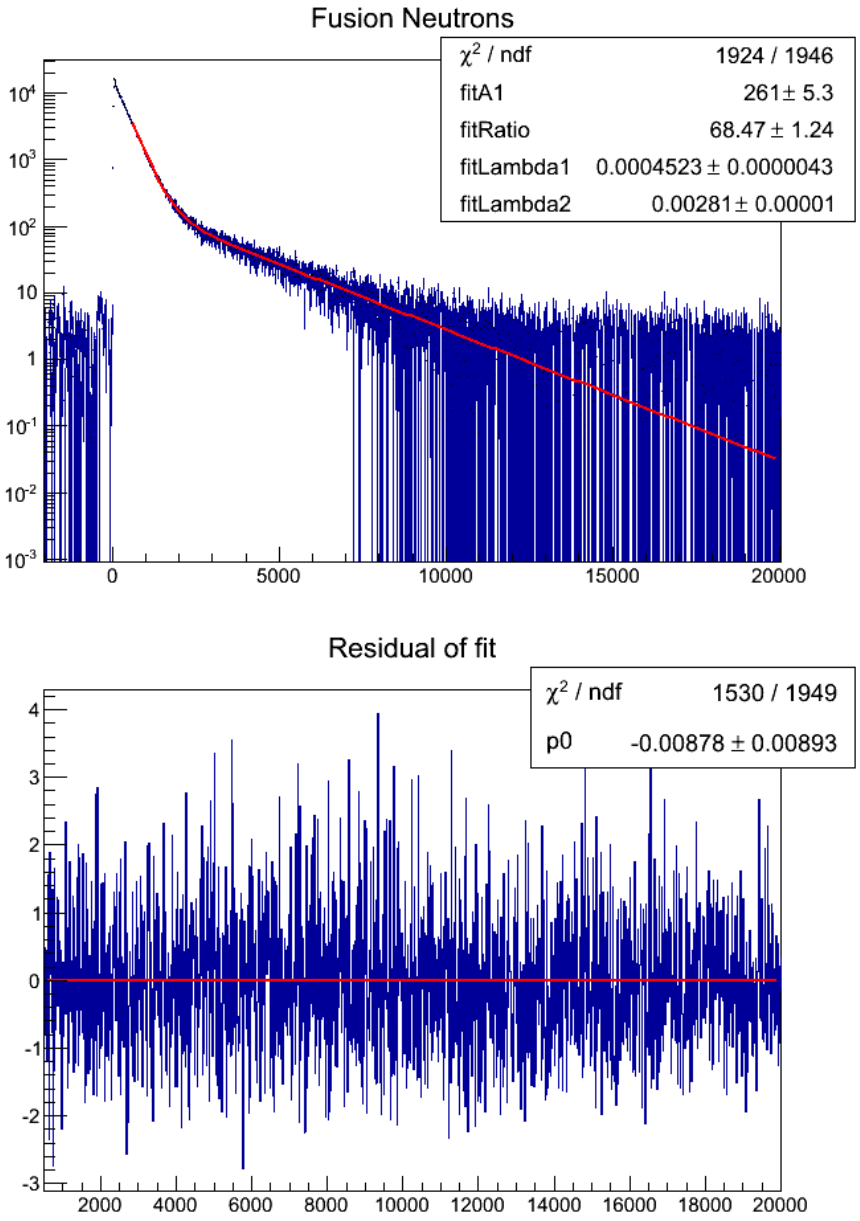

Figure 7.6: Fit of fusion neutrons and residual of fit on the interval 500 ns to 20000 ns.

with the result $\lambda_{qd} = 34.74 \pm 0.21\ \mu s^{-1}$. The uncertainties stated here on both λ_q/λ_d and λ_{qd} are purely statistical. The methods for determining the systematic uncertainties in these results are discussed in the next chapter.

7.2 Capture Neutrons and Λ_q/Λ_d

Capture neutrons are defined according to the conditions described in section 6.2. Since capture occurs much more rapidly from the doublet hyperfine spin state than from the quartet, the rate of capture neutrons will initially increase as the quartet μd atoms transition to the doublet state. Once the quartet state is depopulated, the capture neutron time distribution will fall off at the rate λ_1 which is dominated by the muon decay rate. The target conditions were chosen to strongly enhance the quartet-to-doublet transition rate, so the time distribution peaks within the first few hundred nanoseconds.

As the rising component of the capture neutron time distribution is brief, it is necessary to be able to accurately fit the time distribution at very early times. To make it possible to fit before time zero, an exponentially modified Gaussian (EMG) function is used. An EMG is the convolution of a Gaussian function with a piecewise exponential function which is zero before a time t_0. In our case, we convolve the functions

$$f(t) = \begin{cases} 0 & t < t_0 \\ A_1 e^{-\lambda_1 (t-t_0)} + A_2 e^{-\lambda_2 (t-t_0)} & t \geq t_0 \end{cases} \tag{7.9}$$

and

$$g(t) = \frac{1}{\sqrt{2\pi\sigma^2}} e^{-\frac{t^2}{2\sigma^2}}. \tag{7.10}$$

The parameter t_0 is included in equation 7.9 because the time of flight of neutrons is longer than for the X-rays used to zero-align the detectors, so the rising edge of the capture neutron time distribution may not be exactly at zero. The result of this convolution is

$$\begin{aligned} (f * g)(t) = \frac{1}{2} \Bigg[& A_1 e^{-\lambda_1 (t-t_0)} e^{\frac{(\lambda_1 \sigma)^2}{2}} \operatorname{erfc}\left(\frac{\lambda_1 \sigma^2 - (t-t_0)}{\sqrt{2}\sigma} \right) \\ & + A_2 e^{-\lambda_2 (t-t_0)} e^{\frac{(\lambda_2 \sigma)^2}{2}} \operatorname{erfc}\left(\frac{\lambda_2 \sigma^2 - (t-t_0)}{\sqrt{2}\sigma} \right) \Bigg] \end{aligned} \tag{7.11}$$

where $\operatorname{erfc}(t) = \frac{2}{\sqrt{\pi}} \int_t^\infty e^{-x^2} dx$. Since λ_1 and λ_2 are fixed by the fusion neutron data, the free parameters of this fit function are A_1, A_2, σ, and t_0. The factor of $1/2$ may be absorbed into the coefficients A_1 and A_2.

7.2.1 Backgrounds

A background subtraction is performed using the same method as for the fusion neutrons. That is, the background neutron time distribution, defined in section 6.2, is subtracted from the capture neutron time distribution by normalizing the background histogram to the capture histogram on both an early (-21,000 ns – -1000 ns) and a

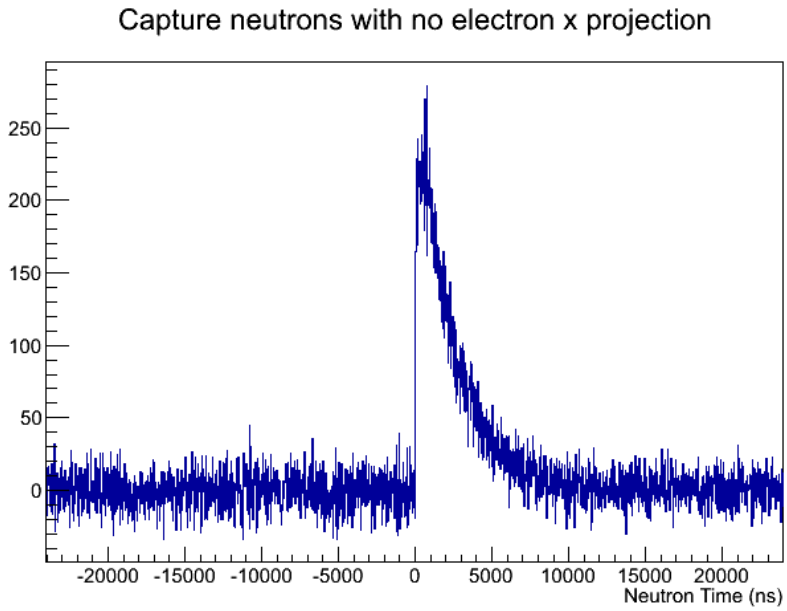

Figure 7.7: Background subtracted capture neutron time distribution. The contribution from photo-nuclear neutrons is not subtracted.

late (14,000 ns – 24,000 ns) interval. As with the fusion neutron fit, the difference between the early and late normalizations, and the effect of the normalization on the results, is discussed in chapter 8. The background-subtracted capture neutron time distribution is shown in figure 7.7. As the capture signal is much smaller than the fusion signal, the time dependent features of the background will have a much bigger impact on the structure of the final, background subtracted time distribution.

A time dependent feature was discovered in the time distribution of "capture" neutrons in the μ^+ data. These are neutrons (as defined in chapter 5) with the capture definition applied, but with a μ^+ stop in the fiducial volume rather than a μ^-. The time dependent feature, shown in figure 7.8, is an exponential decay with a rate equal to the muon disappearance rate which was determined for the run 6 production data to be $4.55780 \times 10^{-4} \pm 2.5 \times 10^{-8}$ ns^{-1} by Luo (2016) [48]. This feature is caused by Michel electrons emitting gamma rays, either from radiative muon decay or bremsstrahlung following decay. These gamma rays undergo photo-nuclear reactions in the neutron detectors and producing a proton or neutron. This effect is seen even when an electron veto is applied because approximately 30% of electrons are undetected. Figure 7.9 illustrates how an electron may induce a signal in a neutron detector while going undetected itself.

In order to properly account for this background, it must be normalized to the production data. This proved to be a challenge. Ideally, it would be normalized to the total number of muon decays in the two data sets, but there is no way to directly determine this number. However, an effective proxy was found. This background is also observed in the time distribution of neutrons from μ^+ stops with a corresponding electron, but can be fully "turned off" by vetoing on neutrons with a prompt coinci-

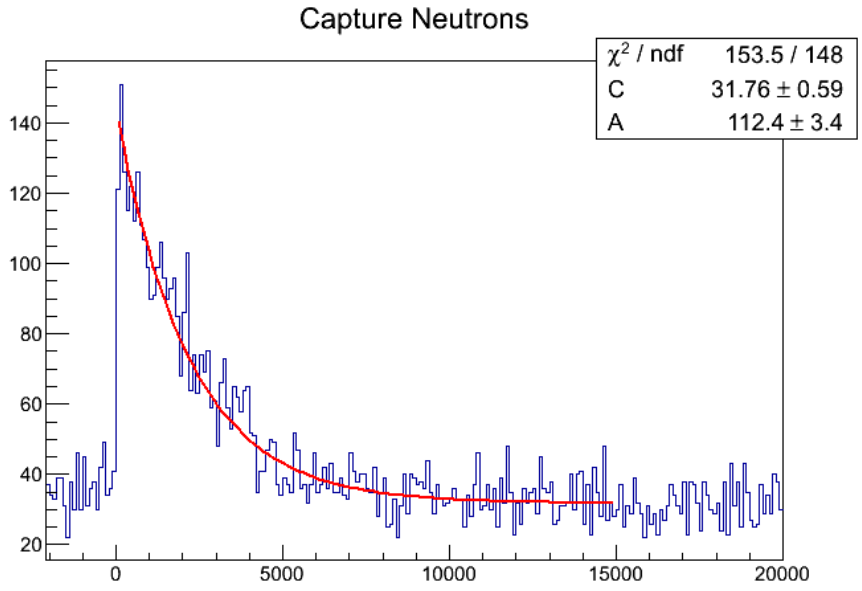

Figure 7.8: Neutrons with an (anti-)electron veto from μ^+ data. The time dependent feature is caused by photo-nuclear reactions in the neutron detectors produced by gamma rays emitted by Michel electrons. The fit to the data is shown in red. The rate of the fit is fixed by the observed muon disappearance rate (from the run 6 production data) of $\lambda = 4.5578 \times 10^{-4}$ ns.

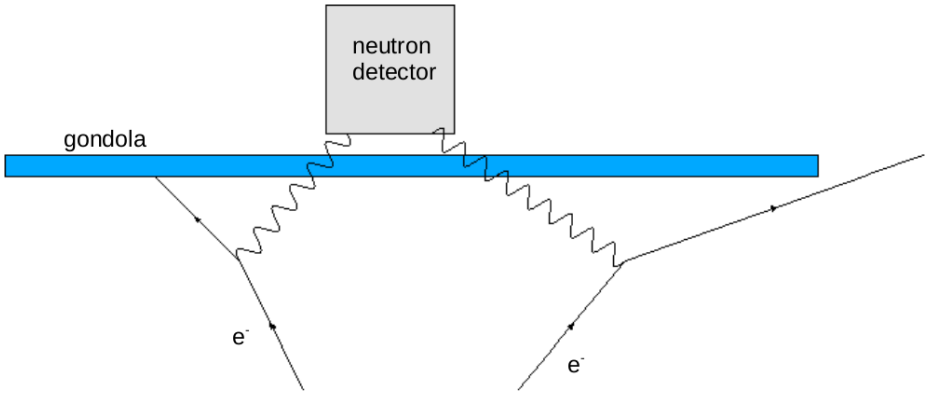

Figure 7.9: Michel electrons may emit gamma rays via bremsstrahlung which can induce photo-nuclear reactions in the neutron detectors. On the left, an electron emits a gamma ray and is detected by the gondola. On the right, an electron emits a gamma ray but misses the gondola and so goes undetected.

dent electron, as shown in figure 7.10. These prompt neutron-electron coincidences are also observed in the μ^- data, as illustrated in figure 5.8. Thus, this background observed in the μ^+ data is normalized to the μ^- data based on the rates of these coincidence evens in the two data sets. The final fit function, therefore, has the form

$$\begin{aligned}(f*g)(t) = \frac{1}{2}\Bigg[& A_1 e^{-\lambda_1(t-t_0)} e^{\frac{(\lambda_1\sigma)^2}{2}} \mathrm{erfc}\left(\frac{\lambda_1\sigma^2-(t-t_0)}{\sqrt{2}\sigma}\right) \\ & + A_2 e^{-\lambda_2(t-t_0)} e^{\frac{(\lambda_2\sigma)^2}{2}} \mathrm{erfc}\left(\frac{\lambda_2\sigma^2-(t-t_0)}{\sqrt{2}\sigma}\right) \\ & + A_+ e^{-\lambda_2 t} e^{\frac{(\lambda_+\sigma)^2}{2}} \mathrm{erfc}\left(\frac{\lambda_+\sigma^2-(t-t_0)}{\sqrt{2}\sigma}\right)\Bigg]\end{aligned} \tag{7.12}$$

where A_+ is the normalized amplitude and λ_+ is the rate of photo-nuclear gamma rays as determined from the μ^+ data. The background term does not include a time offset of t_0 in the exponential, as the background was fit from t=0.

As a check, we may also consider the ratio of muon stops in the TPC, as this number for each data set should also be closely related to the number of muon decays in each data set. The ratio of μ^- stops in the TPC to the ratio of μ^+ stops from the two datasets is 6.461. This does slightly exceed the ratio of photo-nuclear events determined by the above method of 5.065; however, these numbers are consistent enough to demonstrate the reliability of the above method.

7.2.2 Neutron Energy Lower Bound

As part of the systematic error analysis, the low energy threshold of the neutron pulse shape discrimination was varied. This lower bound was increased in 10 keV increments for all detectors simultaneously. A significant systematic effect was observed at low energies up to +200 keV, as can be seen in figure 7.11. Thus, the low energy threshold of the neutron PSD was increased by 200 keV for the final analysis.

7.2.3 Fit Interval

Start and end time scans were conducted on the fit to the capture neutron data similarly to the scans on the fit to the fusion neutron data. It was found that, for start times earlier than about -100 ns, the start time of the fit had no effect on the resulting values of the fit parameters. This is reasonable, as there is no constant term in the fit function and the data is background subtracted, so as long as the fit begins sufficiently to the left of the rising portion, Minuit is essentially "fitting zero." Thus, a start time of -1000 ns was chosen. The start time was varied beyond $t = 0$. For start times greater than 0 ns, the fit quickly becomes irregular with very large error bars on the fit parameters. For these start time scans, the end time was held fixed at 20,000 ns. A start time scan from -1000 ns to 500 ns in 20 ns increments is shown in figure 7.12.

The end time of the fit was varied from 5000 ns to 20,000 ns in 100 ns steps with the start time fixed at -1000 ns. As can be seen in figure 7.13, the parameters A_1 and

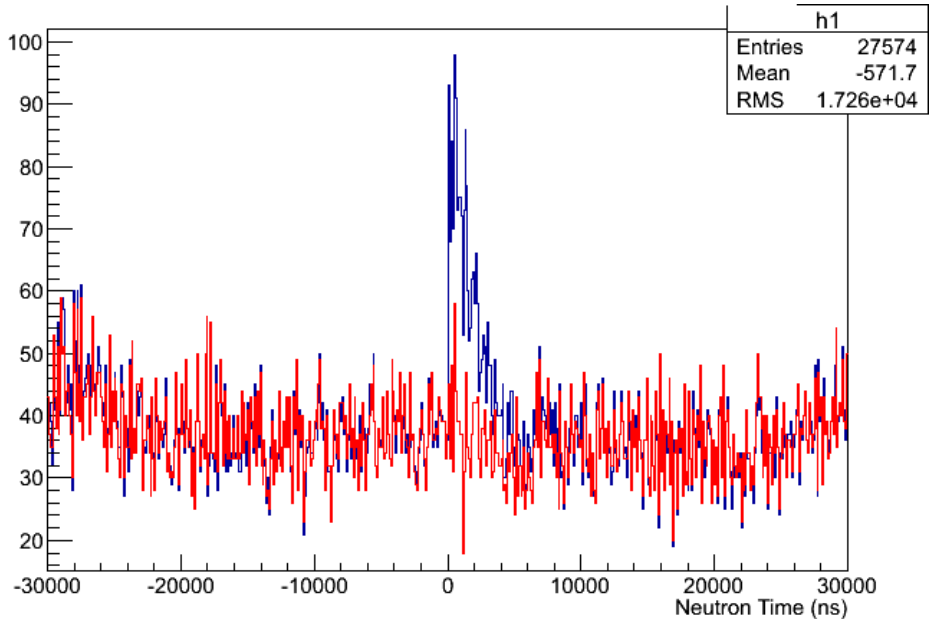

Figure 7.10: Neutrons with an associated (anti-)electron with (red) a neutron-electron coincidence veto or (blue) no such veto. These are data from μ^+ systematic runs. The time dependent feature is "turned off" by a prompt coincidence veto indicating that these neutrons are produced by photo-nuclear reactions caused by gamma rays from radiative muon decay.

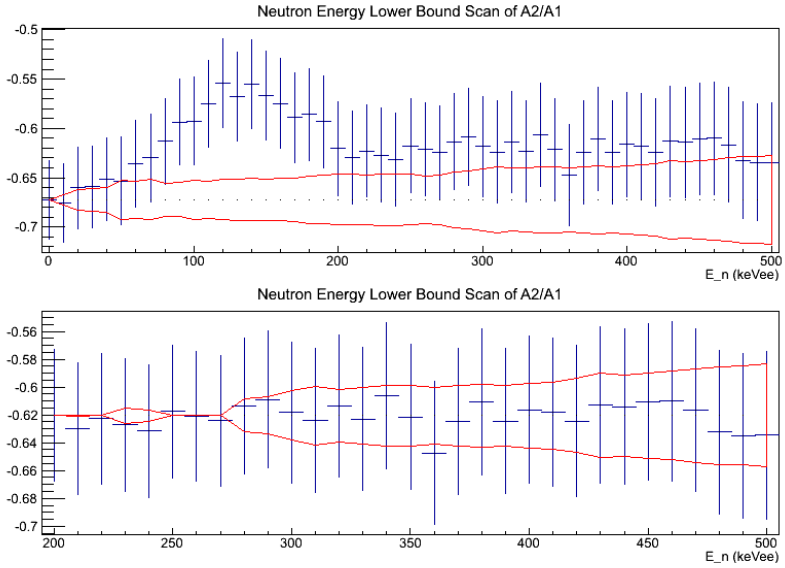

Figure 7.11: Trend plot of A_2/A_1 determined from fit of capture neutrons as a function of neutron energy lower bound. The low energy bound of the neutron definition is increased in 10 keV steps simultaneously for all detectors. The lower plot shows the same data as the upper plot, but starting from 200 keV above the initial lower energy bound. As can be seen, there is a systematic dependence of the fit on the low energy bound of the neutron definition which can be eliminated by increasing this lower bound by 200 keV.

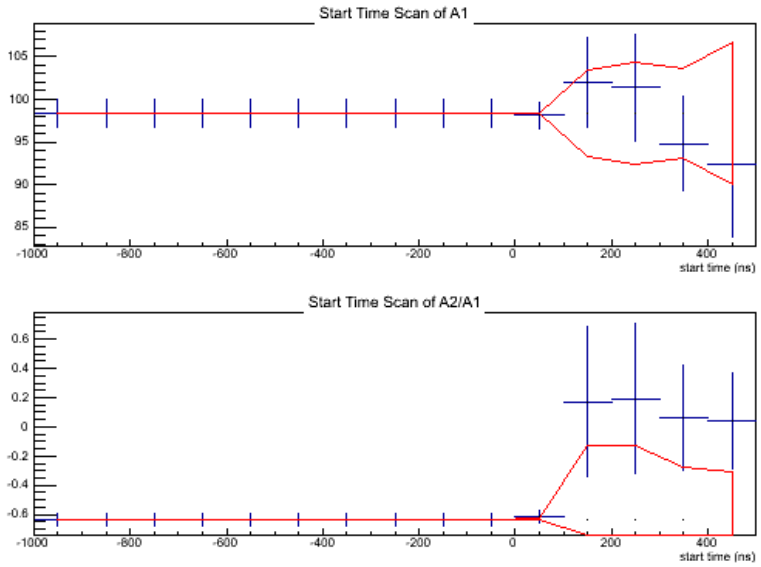

Figure 7.12: Start time scan of fit parameters A_1 and A_2 for start times between -1000 ns and 500 ns with an end time of 20,000 ns. Before -100 ns, the results do not vary. For positive start times, the fit quickly becomes irregular with large error bars.

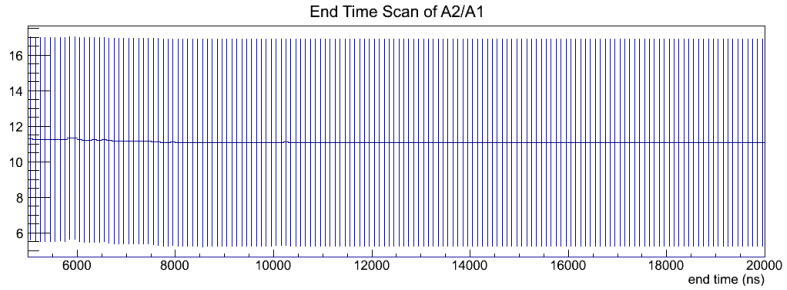

Figure 7.13: End time scan of parameters A_1 and A_2 for the fit to the capture neutron data. These parameters show almost no dependence on the choice of end time, so an end time of 20,000 ns was chosen.

A_2 show very little variation for end times after about 10,000 ns. Thus, an end time of 20,000 ns was chosen.

7.2.4 Results

The results of the fit using this method are shown in figure 7.14. The rising component of the capture neutron rate can be clearly seen in the first microsecond after time zero. This is consistent with the theoretical prediction that $\Lambda_q \ll \Lambda_d$. The data are well fit using this method, as can be seen in the fit residual.

The resulting fit parameters are listed in table 7.2. As in the fusion neutron case, equation 7.3b may be used to find a result of $\Lambda_q/\Lambda_d = 0.066 \pm 0.071$. As this result is consistent with zero, it may be interpreted as an upper bound on Λ_q/Λ_d. This result is stated with only the statistical uncertainty. As with the fusion results, the

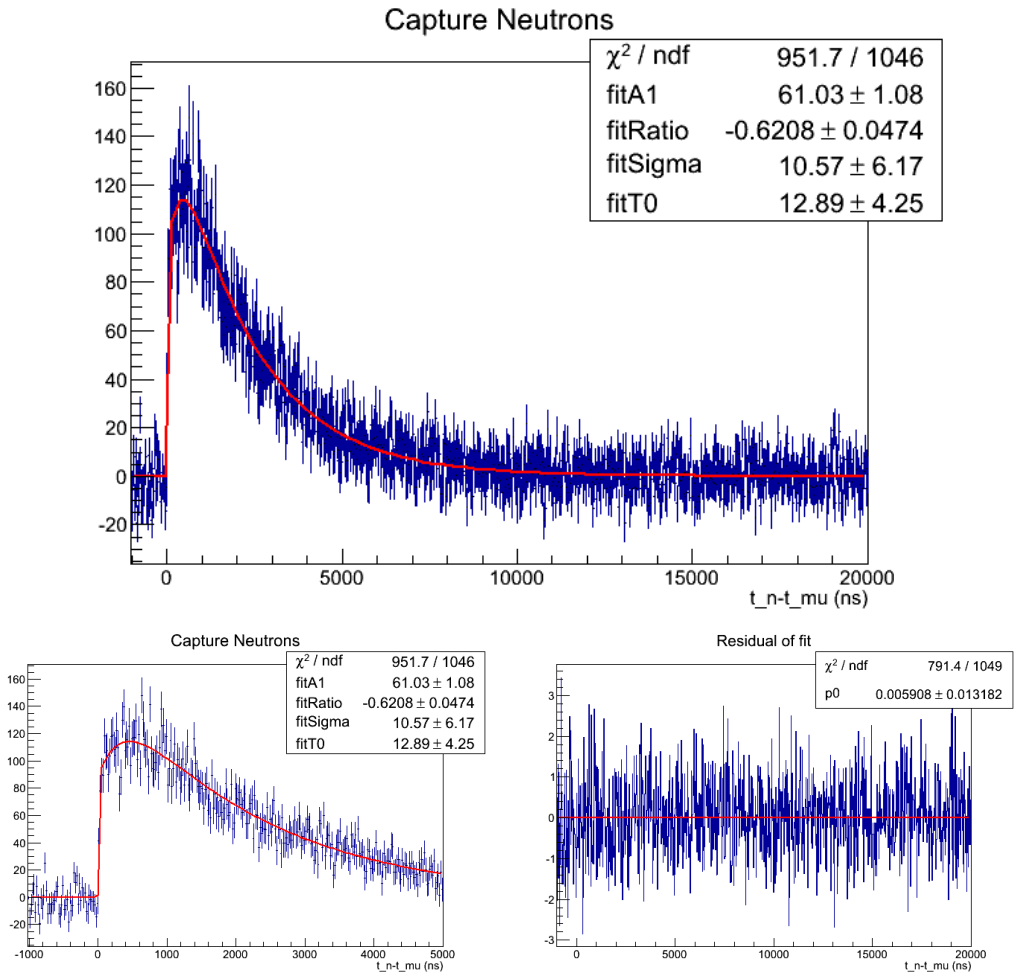

Figure 7.14: (Top row) Fit of time distribution of capture neutrons. (Bottom row) Detail of fit and residual. The data are fit using values of λ_1 and λ_2 determined from the fusion neutron data.

systematic uncertainty will be discussed in the next chapter.

Parameter	Value
χ^2/NDF	951.7/1046
A_1	61.03 ± 1.08
A_2/A_1	-0.6208 ± 0.0474
σ	10.57 ± 6.17
t_0	12.89 ± 4.25

Table 7.2: Parameters of capture neutron time distribution fit.

Chapter 8 Sources of Systematic Uncertainty

There are several potential sources of systematic error in these analyses. These systematics and their impact on the final results for λ_{qd}, λ_q/λ_d, and Λ_q/Λ_d are discussed here.

8.1 Effects of Clock Blinding

The data presented in this dissertation are blinded by detuning the master clock of the experiment by up to 0.5%. For this reason, an uncertainty of 0.5% is applied to all rates used in calculating the results which are not directly determined from the data. The only such rate that appears in the calculation of λ_{qd}, λ_q/λ_d, or Λ_q/Λ_d is λ_q. A 0.5% error on λ_q was propagated through equations 7.3 and 7.8. The resulting absolute uncertainties for λ_q/λ_d, λ_{qd}, and Λ_q/Λ_d are listed in table 8.1.

Quantity	Absolute Error
λ_{qd}	7.65×10^{-3} μs^{-1}
λ_q/λ_d	2.46×10^{-3}
Λ_q/Λ_d	1.33×10^{-5}

Table 8.1: Absolute error in results due to $\leq 0.5\%$ clock blinding. In each case, this error is about two to three orders of magnitude smaller than the statistical error.

8.2 Effects of $\lambda_d \approx 0$ Approximation

In equations 7.5 and 7.8, the approximation that $\lambda_d \approx 0$ was used, as it is much smaller than the other quantities appearing in these calculations. Using the value of $\lambda_d = 0.051(1)$ μs^{-1} at 31 K from the Balin data, we may estimate the error in λ_q/λ_d, λ_{qd}, and Λ_q/Λ_d due to this approximation. This is done by reintroducing the λ_d terms into these equations (see eqns. 2.9 and 7.7) and recalculating the results. The approximation that $\lambda_d \approx 0$ is still used in equation 2.7. The new results and the associated errors are listed in table 8.2. For all three results, the correction is within the statistical error.

Quantity	Original Result	Result With $\lambda_d = 0.051$ μs^{-1}	Absolute Error
λ_{qd}	34.74 ± 0.21 μs^{-1}	34.78 μs^{-1}	4×10^{-2} μs^{-1}
λ_q/λ_d	103.2 ± 1.9	103.6	0.4
Λ_q/Λ_d	0.066 ± 0.071	0.064	2×10^{-3}

Table 8.2: Results of using $\lambda_d = 0.051$ μs^{-1} in the calculation of the results. These calculations still use the approximation that $\lambda_d \approx 0$ in equation 2.7.

8.3 Neutron Energy Cut

The neutron-gamma pulse shape discrimination (PSD) is another potential source of systematic error. The tail/total integral cut described in chapter 5 is done at an early stage in the analysis chain, making a detailed systematic error analysis based on varying this cut infeasible. It is, however, possible to vary the low energy threshold of the PSD (see figure 5.7) at a much later stage of the analysis chain. This low energy threshold is an important systematic to check since the neutron-gamma discrimination is best at high energies and poorer at low energies.

This variation was carried out on both the fusion neutron and capture neutron data sets. A systematic effect was found in the capture neutron data. This is likely caused by gamma rays leaking into the neutron branch at low energies. The lower bound of the neutron energy was increased by 200 keV above the nominal threshold given in table 5.3 to bypass this effect. As this resulted in an adjustment to the final capture neutron data set, this systematic effect is discussed further in chapter 7 (see figure 7.11).

The scan of the lower energy bound in the neutron definition was also performed on the fusion neutron data. As can be seen in figure 8.1, the systematic variation is within the expected range of statistical variation, especially in the first 100 keV.

8.4 Systematic Error Due to TPC Volume Cuts

A fiducial volume cut is applied to muon stops in the TPC to ensure that muons stop in the gas and not in higher Z materials such as the cathode or anode. To investigate the systematic errors that may be introduced by this cut, the bounds of the fiducial volume were varied. Two of the three sets of bounds (in xyz) were held at their nominal values, and the third was varied. For the x-axis (horizontal, orthogonal to the beam), the veto band was increased by one pad width on each side, reducing the acceptance region to the central two rows. For the z-axis (parallel to the beam) the last two downstream pad columns were vetoed. And for the y-axis (vertical) the veto bands at the top and bottom of the fiducial volume were increased by 1.5 cm to a total of 3 cm from the anode and cathode.

The results for these variations are listed in table 8.3 for the fusion data and table 8.4 for the capture data. It should be noted that, due to the order of operations in the data analysis, for this systematic study the normalization of the fusion neutron background (described in section 7.1.1) was simplified, and the capture neutron energy correction (described in section 7.2.2) is not applied. This results in slightly modified values for the fit parameters and the resulting physical parameters as compared to the nominal results. However, this does not prevent the analysis presented in this section from providing good constraints on the systematic effects of the TPC geometry on the main result.

As this systematic analysis involves observing a subset of the data used for the nominal result, the set-subset variance described in equation 7.1.2 is expected. Thus, the systematic error associated with each cut is taken to be the excursion of the result for the subset outside of this variance. For this purpose, the systematic error and the

	Fiducial Volume	X cut	Y cut	Z cut
A_2/A_1	68.51(1.25)	66.69(1.48)	68.80(2.10)	68.69(1.37)
$\lambda_1(\mu s^{-1})$	0.4508(43)	0.4570(52)	0.4474(68)	0.4502(47)
$\lambda_2(\mu s^{-1})$	2.813(13)	2.820(16)	2.814(23)	2.813(14)
λ_q/λ_d	103.3(1.9)	100.6(2.2)	103.7(3.1)	103.6(2.0)
σ_{sub}		1.11	2.45	0.62
σ_{syst}		2.46	0	0
$\lambda_{qd}(\mu s^{-1})$	34.81(21)	34.83(27)	34.93(37)	34.82(23)
σ_{sub}		0.15	0.30	0.09
σ_{syst}		0	0	0

Table 8.3: Systematic error in λ_q/λ_d and λ_{qd} (determined from the fusion neutron time distribution fit) due to varying the TPC acceptance volume bounds. Two axes are held at the fiducial volume bounds, and the third is restricted. The only case in which the result varies by more than the set-subset variance (σ_{sub}) is for λ_q/λ_d for the x-axis cut. The systematic error in λ_q/λ_d is therefore taken to be $\sigma_{syst,\ \lambda_q/\lambda_d} = \sqrt{\Delta(\lambda_q/\lambda_d)^2 - \sigma^2_{sub,\ \lambda_q/\lambda_d}} = 2.46$. The fiducial volume results are slightly different from the final results due to a necessary change in the background normalization.

	Fiducial Volume	X cut	Y cut	Z cut
A_2/A_1	-0.684(38)	-0.755(44)	-0.612(68)	-0.671(46)
Λ_q/Λ_d	-0.028(57)	-0.134(66)	0.080(100)	-0.009(69)
σ_{sub}		0.033	0.082	0.039
σ_{syst}		0.101	0	0

Table 8.4: Systematic error in Λ_q/Λ_d due to varying the TPC volume cuts. Two axes are held at the fiducial volume bounds and the third is restricted. Due to the analysis flow, the neutron energy cut described above is not applied. As with the fusion neutrons, the only deviation outside of the expected set-subset variance is for the x-axis cut, giving a systematic error of $\sigma_{syst,\ \Lambda_q/\Lambda_d} = 0.101$. The fiducial volume results are slightly different from the nominal results due to the neutron energy lower bound cut not being applied.

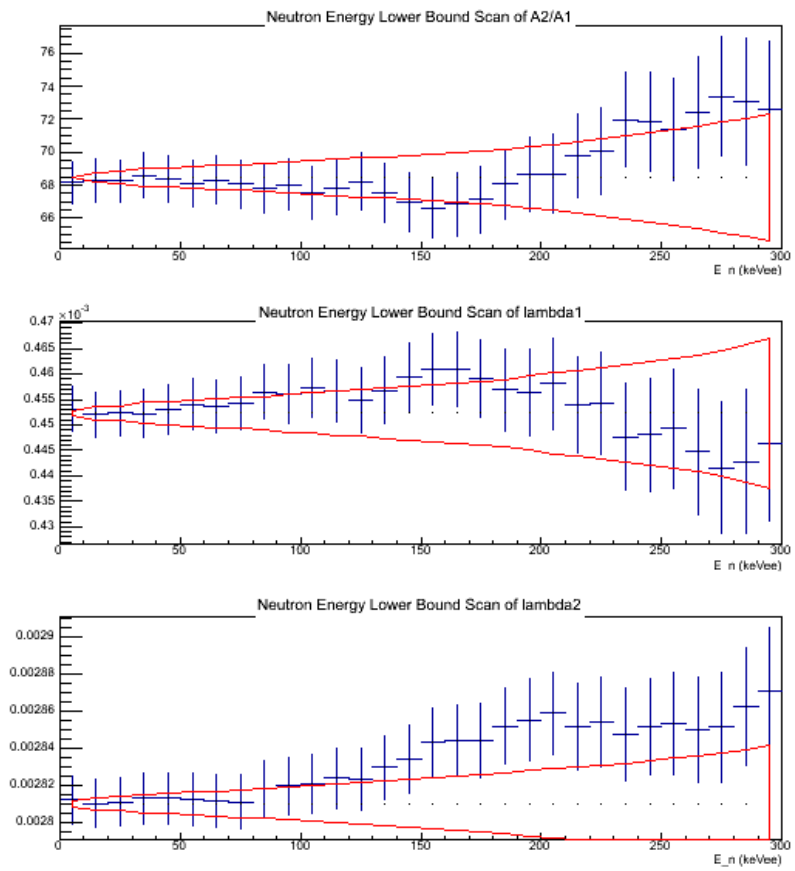

Figure 8.1: Trend plots of the fusion neutron fit parameters A_2/A_1, λ_1, and λ_2 as a function of the neutron energy lower bound in the PSD definition. The horizontal scale shows the increase in the neutron energy lower bound above the nominal threshold given in table 5.3 (in keV), not absolute neutron energy.

set-subset variance are treated as independent, giving the relation

$$\sigma_{syst}^2 = \Delta x^2 - \sigma_{sub}^2 \tag{8.1}$$

where ΔX is the difference between the nominal result and the result for the subset for a given result, and σ_{sub}^2 is the set-subset variance. If $\Delta X < \sigma_{sub}$, the systematic error for the cut is considered negligible.

While the effects of the Y and Z cuts are negligible, there is a significant effect in the cuts along the x-axis. This effect is seen in both the fusion and the capture neutron data. The cause of this systematic effect could not be determined. It should be noted that the values given in table 8.3 for λ_1 and λ_2 were used in fitting the capture neutron data to determine the results in table 8.4. Also, the normalization of the photo-nuclear background (see section 7.2.1) was recalculated for each cut. Thus, the total systematic errors in each result due to TPC volume cuts are $\Delta(\lambda_q/\lambda_d) = 2.46$, and $\Delta(\Lambda_q/\Lambda_d) = 0.101$. However, $\Delta\lambda_{qd}$ is within the set-subset variance. These are by far the largest systematic errors for both λ_q/λ_d and Λ_q/Λ_d, being larger than the statistical error in both cases.

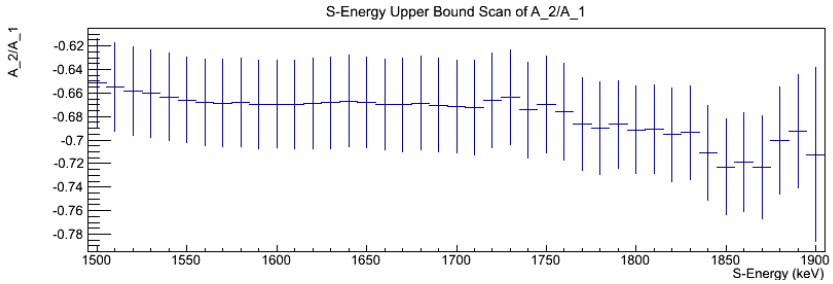

(a)

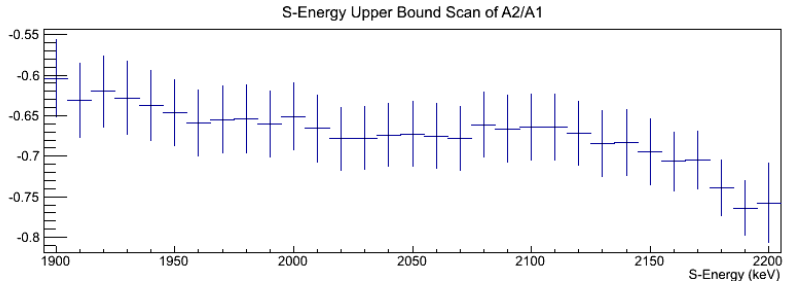

(b)

Figure 8.2

8.5 S-Energy Cuts

Capture neutrons were defined as having (among other requirements) an associated muon stop with S-energy between 1700 keV and 2050 keV. Both of these bounds were varied over a large range. As can be seen in figure 8.2, the value of the key fit parameter A_2/A_1 shows very little variation when the lower bound is between 1600-1700 keV or when the upper bound is between 2000-2100 keV. The systematic error associated with the choice of these bounds is therefore determined by varying the lower bound between 1600-1700 keV and the upper bound between 2000-2100 keV. These errors are found to be $\Delta(\Lambda_q/\Lambda_d) = 1.3 \times 10^{-3}$ for the lower bound and $\Delta(\Lambda_q/\Lambda_d) = 3.4 \times 10^{-3}$.

8.6 Effect of Histogram Re-binning

For both the fusion and capture neutron time distributions, the width of the histogram bins were varied. The bin widths were set at 10, 20, 50, and 100 ns bins. The systematic error resulting from this variation is very small for the fusion neutron data, giving errors of $\Delta(\lambda_q/\lambda_d) = 0.18$ and $\lambda_{qd} = 0.017\ \mu s^{-1}$, about an order of magnitude smaller than $\sigma_{stat.}$ for each quantity. The capture neutron data showed a systematic error of $\Delta(\Lambda_q/\Lambda_d) = 0.012$ which is about half of σ_{stat}.

Bin Width (ns)	A_2/A_1	λ_1 (μs^{-1})	λ_2 (μs^{-1})	λ_q/λ_d	λ_{qd} (μs^{-1})
10	68.47(1.24)	0.4523(43)	2.810(13)	103.2(1.9)	34.74(21)
20	68.48(1.25)	0.4524(45)	2.810(13)	103.2(1.9)	34.74(21)
50	68.54(1.25)	0.4523(44)	2.810(13)	103.3(1.9)	34.74(21)
100	68.67(1.25)	0.4527(44)	2.812(13)	103.5(1.9)	34.77(21)

Table 8.5: Systematic error in λ_q/λ_d and λ_{qd} due to rebinning the fusion neutron time distribution histogram. The nominal result is based on 10 ns binning. The resulting systematic errors are $\Delta(\lambda_q/\lambda_d) = 0.18$ and $\lambda_{qd} = 0.017$ μs^{-1}.

Bin Width (ns)	A_2/A_1	Λ_q/Λ_d
10	-0.607(44)	0.087(66)
20	-0.621(47)	0.066(70)
50	-0.620(48)	0.067(72)
100	-0.610(24)	0.069(11)

Table 8.6: Systematic error in Λ_q/Λ_d due to binning of the capture neutron time distribution histogram. The final result used 20 ns bins. The error is $\Delta(\Lambda_q/\Lambda_d) = 0.012$.

8.7 Capture Neutron Fit Parameters

8.7.1 Background Normalization

The capture neutron background was normalized to the data on both early and late intervals (see section 6.2). The normalization is slightly different for the early and late intervals. Furthermore, there is an inherent statistical uncertainty in the normalization equal to $1/\sqrt{N_s - N_b}$, where N_s and N_b are the total counts in the intervals used for normalization for the signal and background respectively. The normalization used for the final result, which combines both the early and late backgrounds, is 0.5041 ± 0.0025. For the left-hand-side only ($-21,000$ ns $\leq t_n - t_\mu \leq -1000$ ns), the normalization is 0.5007 ± 0.0029, and for the right-hand-side only ($14,000$ ns $\leq t_n - t_\mu \leq 24,000$ ns), it is 0.5131 ± 0.0048. Thus, the background normalization factor was varied between 0.4978 and 0.5179. The resulting variations in the fit to the data are listed in table 8.7. The systematic error due to these variations can be taken to be the quadrature sum of the variation from the nominal value. This gives an absolute systematic error of $\Delta(\Lambda_q/\Lambda_d) = 6 \times 10^{-4}$.

Background Normalization Factor	A_2/A_1	Λ_2/Λ_1
0.5041 (full)	-0.6208 ± 0.0474	0.0661 ± 0.071
0.4978 (LHS)	-0.6206 ± 0.0474	0.0664 ± 0.071
0.5179 (RHS)	-0.6216 ± 0.0469	0.0649 ± 0.070

Table 8.7: Variations in the results for Λ_q/Λ_d due to changes in the background normalization factor. The absolute systematic error due to these variations is $\Delta(\Lambda_q/\Lambda_d) = 6 \times 10^{-4}$.

8.7.2 Values of λ_1 and λ_2

The capture neutron time distribution was fit using values of $\lambda_1 = 4.523 \times 10^{-4} \pm 4.3 \times 10^{-6}\ ns^{-1}$ and $\lambda_2 = 2.810 \times 10^{-3} \pm 1.3 \times 10^{-5}\ ns^{-1}$ extracted from the fusion neutron fit. These parameters were varied within the range of their uncertainties. The results for the capture fit parameter A_2/A_1 for the four combinations of extremal values of λ_1 and λ_2 are given in table 8.8. The overall effect is a systematic error of 0.016%.

$\lambda_1(ns^{-1})$	$\lambda_2(ns^{-1})$	A_2/A_1	Λ_q/Λ_d
4.523×10^{-4}	2.810×10^{-3}	-0.633(48)	0.066(71)
4.48×10^{-4}	2.793×10^{-3}	-0.610	0.082
4.48×10^{-4}	2.823×10^{-3}	-0.613	0.078
4.566×10^{-4}	2.793×10^{-3}	-0.628	0.055
4.566×10^{-4}	2.823×10^{-3}	-0.631	0.051

Table 8.8: Effect of varying λ_1 and λ_2 on parameters A_1 and A_2 of the capture neutron fit function. The first line gives the values used for the final result. The variation results in a systematic error of $\Delta(\Lambda_q/\Lambda_d) = 0.016$, well within the range of the statistical error.

8.7.3 Photo-Nuclear Background

The amplitude, A_+, and rate, λ_+, of the photo-nuclear reaction background also have associated uncertainties which will contribute to the systematic error in the final result for Λ_q/Λ_d. Varying $\lambda_+ = 4.55780(25) \times 10^{-4}$ ns^{-1} (combined statistical and systematic errors) results in a 3% error, while varying $A_+ = 11.08 \pm 0.42$ results in an additional 2.2% error.

A_+	$\lambda_+(\mu s^{-1})$	A_2/A_1	Λ_q/Λ_d
4.40(22)	0.455780(25)	-0.633(48)	0.062(71)
4.18	0.455755	-0.609	0.084
4.18	0.455805	-0.609	0.084
4.62	0.455755	-0.632	0.049
4.62	0.455805	-0.632	0.049

Table 8.9: Systematic effect of varying the amplitude (A_+) and rate (λ_+) of the photo-nuclear background observed in the μ^+ data. The systematic error is $\Delta(\Lambda_q/\Lambda_d) = 0.018$.

8.8 Combined Error

The total systematic errors are therefore given in table 8.10 for λ_q/λ_d and λ_{qd}, and in table 8.11 for Λ_q/Λ_d. The final results are, therefore

$$\lambda_q/\lambda_d = 103.2 \pm 1.9(stat.) \pm 2.50(syst.)$$

$$\lambda_{qd} = 34.74 \pm 0.21(stat.) \pm 0.044(syst.)$$

$$\Lambda_q/\Lambda_d = 0.066 \pm 0.071(stat.) \pm 0.105(syst.)$$

Source	$\Delta(\lambda_q/\lambda_d)$	$\Delta\lambda_{qd}$ (μs^{-1})
Blinding	2.46×10^{-3}	7.65×10^{-3}
$\lambda_d \approx 0$	0.4	0.04
TPC volume X	2.46	0
Binning	0.18	0.017
total	2.50	0.044

Table 8.10: Combined absolute systematic error in λ_q/λ_d and λ_{qd}. The individual sources of error are treated as independent of each other.

source	$\Delta(\Lambda_q/\Lambda_d)$
blinding	1.33×10^{-5}
$\lambda_d \approx 0$	2×10^{-3}
TPC volume X	0.101
Binning	0.012
Background Normalization	6×10^{-4}
λ_1 and λ_2	0.016
Photo-nuclear background	0.018
total	0.105

Table 8.11: Combined absolute systematic error in Λ_q/Λ_d. The individual sources of error are treated as independent of each other.

Chapter 9 Conclusions

9.1 Discussion of Results

The method of identifying helium recoils in the TPC has proven to be very effective for discriminating between neutrons from $dd\mu$ fusion and neutrons from deuterium capture in the MuSun experiment. It has allowed for the determination of the first experimental limit on the relative rates of muon capture on deuterium from the quartet and doublet hyperfine spin states of the μd atom. While, the result of $\Lambda_q/\Lambda_d < 0.275$ (at 90% confidence level) is limited by both statistical and systematic error, it is consistent with theoretical predictions that Λ_q is much less than Λ_d. Furthermore, this result shows that this method is an effective way to measure Λ_q/Λ_d.

MuSun run 6 was followed by two more production runs which collected approximately 10^{10} more muon stop events. This is nearly an order of magnitude more than the statistics collected during run 6 alone. Applying the methods described in this dissertation to those data could significantly improve the statistical precision on Λ_q/Λ_d. In the future, a dedicated experiment could be conducted which could further improve the precision. Such an experiment could use much of the same design as MuSun, and even much of the same apparatus, but with some modifications to optimize for the measurement of Λ_q/Λ_d which will be described below.

The method of helium recoil identification has also allowed for a reproduction of the measurement of the ratio of $dd\mu$ molecular formation from the quartet and doublet hyperfine spin states of the μd atom previously determined by Raha [1]. It is notable that the result presented here differs from Raha's result of $\lambda_q/\lambda_d = 85.51 \pm 3.25$ (at 34 K) by 3.9σ. Furthermore, the Balin data [8] gives a value of $\lambda_q/\lambda_d = 80.98 \pm 2.10$ (at 32.2 K). This differs from our result by 5.9σ. The value of the quartet to doublet hyperfine transition rate reported here is also significantly different from the values found by Raha and Balin of $\lambda_{qd} = 38.49 \pm 0.21\ \mu s^{-1}$ and $\lambda_{qd} = 37.1 \pm 0.3\ \mu s^{-1}$ respectively. The discrepancy is quite large. The Raha result differs from ours by 12.5σ and the Balin result by 6.4σ. The large discrepancy in the values of λ_{qd} could be a result of an inaccurate determination of the environmental conditions of the deuterium target, as λ_{qd} is very sensitive to the gas density. Indeed, the target conditions for run 4 were T = 34 K and P = 5.6 bar which, according to the NIST Chemistry Webbook [45], corresponds to a density fraction of $\phi = 0.0700$, whereas the number stated in Raha is $\phi = 0.0614$. To first order, λ_{qd} is inversely proportional to ϕ, so applying this correction to the Raha result gives a value of $\lambda_{qd} = 33.76 \pm 0.18$. This gives a discrepancy of 3.5σ and, in fact, over-corrects the difference. Thus, the disagreement may be fully resolved by clarifying the determination of ϕ. However, this cannot explain the discrepancy in λ_q/λ_d, as it is only very weakly dependent on the gas density. A dedicated experiment for measuring Λ_q/Λ_d would also allow for new measurements of λ_q/λ_d and λ_{qd} which could help to resolve this discrepancy.

9.2 Future Experiments

A dedicated experiment for measuring Λ_q/Λ_d would look very similar to MuSun, but with some modifications. The new experiment would still use a pile-up protected muon beam on a cryogenic deuterium gas target inside at TPC, but the conditions of the beam and target, along with the configuration of the detectors would be modified to optimize for measuring Λ_q/Λ_d.

The incoming muon beam would still need to be pile-up protected to ensure that each outgoing neutron is correctly correlated with an incoming muon. However, it would be important to try to further attenuate the early, beam-dependent neutron background. This could be accomplished either through shielding or by removing the beam kicker. Removing the beam kicker would remove the time structure from any neutron backgrounds coming from the beam, but it would significantly increase the muon pile-up rate. Muon pile-ups could still be vetoed by using the entrance counters and adjusting the beam intensity, but the rate of pile-up-free entrances would likely be significantly reduced as compared to using the beam kicker. Shielding the experiment from these beam-dependent neutrons could reduce or eliminate this time-dependent neutron background while still allowing for the use of the beam kicker. This shielding would most likely be a layer of a neutron absorbing hydrocarbon upstream of the neutron detectors. The challenge would be finding a configuration for this shielding which can effectively block nearly all of the beam-dependent neutrons while fitting in with the rest of the experimental apparatus. The cost of the shielding materials would also be a consideration.

The photo-nuclear background discovered in the μ^+ data shows that electron detection is important for an accurate measurement of Λ_q/Λ_d. However, the design of the electron detectors would need to be modified from that of MuSun. Since MuSun's primary goal is the determination of Λ_d by measuring the muon disappearance rate to high precision, it was of paramount importance to positively identify electrons originating in the deuterium gas and veto background electrons with very high efficiency. Hence the need for the two ePCs as well as the eSCs. In an experiment whose focus is the positive identification of capture neutrons, the primary function of the electron detectors would be as veto counters. Track reconstruction would not be necessary, since vetoing on background electrons would not impact the shape of the capture neutron time distribution (assuming background electrons are not correlated with the muon entrance, which is a reasonable assumption). Instead, the electron detectors should be designed to maximize total electron detection efficiency. In the configuration used for MuSun, the electron detectors are only about 70% efficient. This would need to be increased to much closer to 100%. This could be accomplished in a few ways.

The ePCs could be removed and the eSCs could be moved in to a tighter radius, removing some (up to half) of the eSC gondolas in the process. This has the advantage of being a relatively small modification to the MuSun setup, and the additional advantage of allowing the neutron detectors to be mounted much closer to the deuterium target, which would also significantly increase neutron detection efficiency. Electron detection efficiency could also be improved by adding plastic scintillating

end-caps on both the upstream and downstream sides of the eSC array. Overall it would most likely be best to make simple modifications such as these to the MuSun design, as it would be relatively simple to do, and the eSC gondolas are well suited for mounting additional neutron detectors.

Naturally, for a dedicated Λ_q/Λ_d experiment, the number of neutron detectors would be increased. Organic liquid scintillator detectors have proven to be well suited for detecting neutrons at the energies produced by fusion and capture. However, with only eight detectors mounted rather far from the target, the solid angle coverage is very low, less than 5%. By adding a pair of neutron detectors behind each gondola, the neutron detection efficiency would be increased by a factor of four. Along with simply increasing the number of detectors, positioning them closer to the deuterium target would substantially increase the solid angle coverage of each detector. This could be accomplished by removing the eSCs and moving the gondolas in to a tighter radius, as described above. If the neutron detectors could be moved to half the distance from the deuterium target (which is possible if the eSCs are removed), and eight more detectors were added behind the remaining gondolas, then this would give an overall factor of eight increase in detection efficiency. It may be possible to mount more than two neutron detectors behind each gondola, but this would require redesigning all of the gondola mounts including the ones which already have neutron detectors on them.

As with MuSun, the deuterium target would still be contained in a time projection chamber which would be used for stop identification and ^{3}He recoil detection. As with MuSun, the target should be a cryogenic gas so that $\lambda_{dq} \approx 0$, as this greatly simplifies the physics of both muon capture and $dd\mu$ molecular formation. However, a lower density than that used for MuSun would be best, as this reduces both λ_{qd} and $dd\mu$ formation. A low value for λ_{qd} is desirable since this increases the time that μd atoms formed in the quartet spin state remain in that state and enhance the rising component of the capture neutron time distribution. The trade off is that a lower gas density also reduces the stopping fraction of muons in the gas. The optimal target conditions, in both temperature and density, would need to be determined using numerical calculations and Monte Carlo simulations.

Overall, an experiment specifically designed to measure Λ_q/Λ_d could be built using much of the existing MuSun apparatus with only relatively simple modifications. It is reasonable to estimate an increase in capture neutron events collected per muon entrance of around an order of magnitude by increasing the total detection efficiency of both neutrons and electrons, and by optimizing the target conditions.

Chapter A Two-Step Fitting Method

The fitting method for both the fusion and capture time distributions is a two-step process. This is done in order to properly set the error bars on each bin. Initially, the error associated with each bin of a histogram is $\sqrt{n}$ where n is the number of counts in a bin. This is the default for a ROOT histogram and is based on Poisson statistics. However, when fitting a histogram, it is more appropriate to have the error associated with each bin equal $\sqrt{x}$ where x is the value of the fit function at that bin. In the high statistics limit, assuming the data are perfectly modeled by the fit function, $n \to x$, so these errors are equal. However, this is not the case in practice, especially for relatively low statistics data such as the capture neutron data. Furthermore, both the fusion and capture neutron data are background subtracted. Thus, at late times (and early times in the case of the capture neutrons), most bins have very few counts or even zero/negative counts. Thus, simply using $\sqrt{n}$ will not properly represent the error on most bins in the histogram.

To resolve this issue, the histogram is fit once to give an approximate value for the fit function at each bin center. The error, δ_i, in the ith bin would then be set to $\sqrt{x_i}$ where, again, x_i is the value of the fit function at the center of the ith bin. However, both the capture and fusion neutron data are background subtracted, so $\sqrt{x_i}$ does not fully account for the error in the bin value, especially for bins close to zero after background subtraction. For a bin which is approximately zero after background subtraction, the error is

$$\delta_i = \sqrt{c_s + c_b \left(\frac{c_s}{c_b}\right)^2} \tag{A.1}$$

where c_s is the average value of the flat region of the capture/fusion neutron spectrum before background subtraction and c_b is the average value of the flat region of the background spectrum. These values are determined from the early and late regions used for background normalization as described in chapter 7. In fact, this error should be added to every bin of the histogram. Thus, the total error for the ith bin is

$$\delta_i = \sqrt{x_i + c_s \left(1 + \frac{c_s}{c_b}\right)}. \tag{A.2}$$

This error is calculated for each bin of the histogram and set as the error for that bin. The histogram is then fit a second time to give the final result.

Bibliography

[1] N. Raha. *Measurement of the dμd Quartet-to-Doublet Molecular Formation Rate Ratio ($\lambda_q : \lambda_d$) and the μd Hyperfine Rate (λ_{qd}) Using the Fusion Neutrons From μ Stops in D_2 Gas*. PhD thesis, University of Kentucky, 2015.

[2] `https://upload.wikimedia.org/wikipedia/commons/7/78/FusionintheSun.svg`.

[3] M. Doi, T. Sato, H. Ohtsubo, and M. Morita. Muon capture in hyperfine states of muonic deuterium. *Prog. Theor. Phys.*, 86(1), Jul 1991.

[4] V. A. Andreev et al. (MuSun collaboration). Muon capture on the deuteron. *arXiv:1004.1754v1 [nucl-ex]*, Apr 2010.

[5] P. Kammel, C. Petitjean, and A.A. Vasilyev (MuSun Collaboration). Progress report 2012 and beam request for 2013 - the musun experiment, 2012.

[6] T. I. Banks. *Measurement of the Rate of Muon Capture in Hydrogen Gas and Determination of the Protons Induced Pseudoscalar Coupling g_P*. PhD thesis, University of California, Berkeley, 2001.

[7] M. Doi, T. Sato, H. Ohtsubo, and M. Morita. Effect of meson exchange current on deuteron muon capture. *Nucl. Phys. A*, 511, 1990.

[8] D. V. Balin et al. High precision study of muon catalyzed fusion in d2 and hd gas. *Physics of Particles and Nuclei*, 42(2):185–214, 2011.

[9] K.A. Olive et al. (Particle Data Group). *Chin. Phys. C*, 38, 090001, 2014.

[10] V. Tishchenko et al. (MuLan Collaboration). Detailed report of the mulan measurement of the positive muon lifetime and determination of the fermi constant, Mar 2013.

[11] V. A. Andreev et al. (MuCap Collaboration). Measurement of muon capture on the proton to 1% precision and determination of the pseudoscalar coupling g_p. *Phys. Rev. Lett.*, 110(012504), Jan 2013.

[12] David J. Griffiths. *Introduction to Quantum Mechanics*. Pearson Prentice Hall, second edition, 2005.

[13] S. L. Mintz. Pion reactions in deuterium and the muon-capture rate and weak form factors. *Phys. Rev. C*, 22(2507), Dec 1980.

[14] D.F. Measday. The nuclear physics of muon capture. *Physics Reports*, 354, 2001.

[15] M. Butler, J-W. Chen, and X. Kong. Neutrino-deuteron scattering in effective field theory at next-to-next-to-leading order. *Phys. Rev. C*, 63(035501), Jan 2001.

[16] S. Ando, T.-S. Park, K. Kubodera, and F. Myhrer. The μd capture rate in effective field theory. *Phys. Lett. B*, 533, 2002.

[17] J.-W. Chen, T. Inoue, X. Ji, and Y. Li. Fixing two-nucleon weak-axial coupling $l_{1,A}$ from $\mu^- d$ capture. *Phys. Rev. C*, 72(061001), Dec 2005.

[18] T. S. Park et al. The solar *hep* process in effective field theory.

[19] Q. R. Ahmad et al. Direct evidence for neutrino flavor transformation from neutral-current interactions in the sudbury neutrino observatory. *Phys. Rev. Lett.*, 89:011301, Jun 2002.

[20] M. Cargnelli et al. Measurement of the muon capture rate in gaseous deuterium. In *Proceedings of the XXIII Yamada Conf. on Nuclear Weak Processes and Nuclear Structure*.

[21] G. Bardin et al. A measurement of the muon capture rate in liquid deuterium by the lifetime technique. *Nucl. Phys. A*, 453, Jun 1986.

[22] J. Adam Jr. et al. Calculation of doublet capture rate for muon capture in deuterium within chiral effective field theory. *Phys. Lett. B*, 709, Mar 2012.

[23] L. E. Marcucci et al. Chiral effective field theory predictions for muon capture on deuteron and ^{3}he. *Phys. Rev. Lett.*, 108(052502), Jan 2012.

[24] L. E. Marcucci et al. Muon capture on deuteron and ^{3}he. *Phys. Rev. C*, 83(014002), Jan 2011.

[25] P. Ricci, E. Truhlík, B. Mosconi, and J. Smejkal. Muon capture in deuterium. *Nucl. Phys. A*, 837(1–2), Jun 2010.

[26] J. Adam, E. Truhlik, S. Ciechanwicz, and K.-M. Schmitt. Muon capture on deuterium and the meson exchange current effect. *Nucl. Phys. A*, 507, 1990.

[27] N. Tatara, Y. Kohyama, and K. Kubotera. Weak interaction processes on deuterium: Muon capture and neutrino reactions. *Phys. Rev. C*, 42(4), Oct 1990.

[28] S. L. Mintz. Muon-capture rates in deuterium and the weak form factors in the timelike region. *Phys. Rev. D*, 8:2946–2957, Nov 1973.

[29] P. Pascual, R. Tarrach, and F. Vidal. Muon capture in deuterium. *Il Nuovo Cimento A (1965-1970)*, 12(1):241–248, 1972.

[30] E. Cremmer. Relativistic treatment of muon capture in deuterium. *Nuclear Physics B*, 2(4):409 – 423, 1967.

[31] I-T. Wang. Muon capture by deuterons. *Phys. Rev.*, 139:B1539–B1544, Sep 1965.

[32] Kanetada Nagamine. *Introductory Muon Science*. Cambridge University Press, 2003.

[33] D. Bakalov. *Muon Catalyzed Fusion*, 3(321), 1988.

[34] T. Suzuki, D. F. Measday, and J. P. Roalsvig. Total nuclear capture rates for negative muons. *Phys. Rev. C*, 35:2212–2224, Jun 1987.

[35] F. Wauters. `https://muon.npl.washington.edu/elog/musun/analysisrun6/141`.

[36] Y.-A. Thalmann, R. Jacot-Guillarmod, F. Mulhauser, L. A. Schaller, L. Schellenberg, H. Schneuwly, S. Tresch, and A. Werthmüller. Muon transfer from excited states of hydrogen and deuterium to nitrogen, neon, and argon. *Phys. Rev. A*, 57:1713–1720, Mar 1998.

[37] The PSI Proton Accelerator | Paul Scherrer Institut (PSI). `https://www.psi.ch/media/the-psi-proton-accelerator`.

[38] C. Petitjean et al. `https://muon.npl.washington.edu/elog/musun/Run6/442`.

[39] M. J. Barnes and G. D. Wait. A 25-kv 75-khz kicker for measurement of muon lifetime. *IEEE Transactions on Plasma Science*, 32(5), October 2004.

[40] P. Kammel, C. Petitjean, and A.A. Vasilyev (MuSun Collaboration). Progress report 2013 and beam request for 2014 - the musun experiment, 2013.

[41] P. Kammel. `https://muon.npl.washington.edu/elog/musun/Run6/31`.

[42] MACOR® Product Information Sheet. `http://www.corning.com/media/worldwide/csm/documents/71759a443535431395eb34ebead091cb.pdf`.

[43] V.A. Ganzha, P.A. Kravtsov, O.E. Maev, G.N. Schapkin, G.G. Semenchuk, V.A. Trofimov, A.A. Vasilyev, M.E. Vznuzdaev, S.M. Clayton, P. Kammel, B. Kiburg, M. Hildebrandt, C. Petitjean, T.I. Banks, and B. Lauss. A circulating hydrogen ultra-high purification system for the mucap experiment. *Nuclear Instruments and Methods in Physics Research Section A: Accelerators, Spectrometers, Detectors and Associated Equipment*, 578(3):485 – 497, 2007.

[44] Michael E. Peskin and Daniel V. Schroeder. *An Introduction to Quantum Field Theory*. Westview Press, 1995.

[45] NIST chemistry webbook, NIST standard reference database number 69.

[46] Andrzej Adamczak and Mark P. Faifman. *Influence of epithermal muonic molecule formation on kinetics of the μCF processes in deuterium*, page 63 –68. Springer Netherlands, 2012.

[47] G.W. Bennett et al. Statistical equations and methods applied to the precision muon $(g-2)$ experiment at bnl. *Nuclear Instruments and Methods in Physics Research, Section A: Accelerators, Spectrometers, Detectors and Associated Equipment*, 579(3):1096–1116, Sept. 2007.

[48] X. Luo. PhD thesis.

Vita

Education

- University of Kentucky, Lexington, KY, Anticipated Ph.D. in Physics, Dec. 2016, M.S. in Physics, May 2012
- University of Florida, Gainesville, FL, M.S. in Mathematics, Dec. 2007
- Haverford College, Haverford, PA, B.S. in Physics, May 2001

Research Experience

- Graduate Research Assistant, MuSun Experiment, University of Kentucky department of Physics and Astronomy, Jan. 2011 Dec. 2016.
- Research Assistant, University of Florida department of Astronomy, Oct. 2001 Dec. 2002

Teaching Experience

- Graduate Teaching Assistant, University of Kentucky, Aug. 2008 May 2015.
  - Physics I and II lab and recitation, algebra-based and calculus-based.
  - Physics and Astronomy for Teachers.
- Adjunct Professor, Bluegrass Community and Technical College, Sept. 2015 Dec. 2015
  - Astronomy I, Aug 2010 Dec 2010.
  - Physics I lab, calculus-based.
- Graduate Teaching Assistant, University of Florida, Jan. 2003 Dec. 2004.
  - Precalculus I and II recitation.
  - Calculus I recitation.

Publications

R. K. Neely, A. Sarajedini, and D. H. Martins, CCD Photometry of the Galactic Globular Cluster NGC 6144, The Astronomical Journal 119 (2000).

Presentations

Neely, R. Kreswell, the MuSun Collaboration, Measurement of Fusion Neutrons and Capture Neutrons From Muon Stops in Deuterium for MuSun, APS April Meeting 2015 60, 4 (2015).